國 立 交 通 大 學
光電工程學系暨研究所
博 士 論 文

氣相傳輸法成長氧化鋅奈米線之光學特性研究

Optical properties of ZnO-based nanowires grown by
vapor transport method

研 究 生：徐旭政

指 導 教 授：謝文峰 教授

中 華 民 國 九 十 四 年 六 月

氣相傳輸法成長氧化鋅奈米線之光學特性研究

Optical properties of ZnO-based nanowires grown by vapor transport method

研 究 生：徐 旭 政　　　　　Student　Hsu-Cheng Hsu

指導教授：謝 文 峰 教 授　　　Advisor　Dr. Wen-Feng Hsieh

國 立 交 通 大 學

光 電 工 程 研 究 所

博 士 論 文

A Dissertation
Submitted to Department of Photonics and Institute of Electro-Optical Engineering
College of Electrical Engineering and Computer Science
National Chiao Tung University
In Partial Fulfillment of the Requirements
for the Degree of
Doctor of Philosophy
in
Electro-Optical Engineering

June 2005
Hsinchu, Taiwan, Republic of China

中華民國九十四年六月

誌　謝

在通過了學位口試之後，博士生日子的終將結束了。 回首求取博士學位的日子裡，幫助過我及提攜我的人很多。 首先，我要感謝我的指導老師 謝文峰教授。 無論在學術研究以及待人處世上，謝老師都讓我學到了很多。 老師在論文主題選擇上給我很大的自由度，讓我有機會自己去找尋適當的題目。 在我徬徨無助的時候又能適時的給予引導並陪伴我解決問題。 對老師的敬意以及謝意實非筆墨可以形容讓我銘感五內，永記在心。 其次要感謝口試委員們對論文的指正以及建議，使本論文更臻完善，也讓我對於未來研究的方向以及需要補強的地方了然於胸。 我也要謝謝雷射診測實驗室朝夕相處的夥伴們在研究上以及生活上的幫忙：林家弘博士、伯澤、同慶以及維仁對實驗室公務的分擔以及生活經驗的分享；裕奎學長在研究上的討論以及體能上的鍛鍊；世昊、家豪、景升、楊松、宜錦、俊毅、國峰等學弟妹在實驗上的協助。 映如在精神上的鼓勵以及生活上的幫忙讓我無後顧之憂。 大學同窗兼室友及現在的實驗夥伴信民兄的大力幫忙更是感激在心。 很多的構想以及腦力的激盪都是在電話裡提出來，在一兩星期內的星期假日就迅速的實現。 這種有效率的研究態度讓我們的研究進度不至於落後太多。 希望未來還有機會來能夠一起並肩作戰！

此外我要謝謝工研院材料所黃宏勝博士的實驗協助，交大光電所尖端光電與材料實驗室以及工研院奈米中心的設備提供亦要一併感謝。

我要感謝的我的 雙親給予我最大的支持與鼓勵。 在看似光鮮實則荊棘滿佈的求學之路曾經跌倒了數次。 您們都用最大的包容力，無怨無悔地支持我及陪伴我，讓我站起來繼續走下去。 希望我的表現沒有讓您們失望。

最後感謝國科會以及教育部追求卓越計畫的經費支持，才能讓本論文得以順利完成。

氣相傳輸法成長氧化鋅奈米線之光學特性研究

研究生：徐旭政　　　　　指導教授：謝文峰 教授

國立交通大學光電工程學系暨研究所

摘要

我們成功地利用氣相傳輸法成長氧化鋅奈米線，並研究其結構與光學特性. 六方形柱狀氧化鋅奈米線能夠選擇性地成長在預鍍多晶氧化鋅薄膜上。 當鋅蒸氣傳送到基板上時，會很快地由氣態轉為固態，並且氧化成氧化鋅。 而在薄膜上的奈米尺度的凹坑以及山丘可以提供一個很好的成核點因此成長出氧化鋅奈米線。 使用鍍金的多孔矽做為基板時，我們發現當多孔隙的孔矽率越高時，氧化鋅奈米線越有垂直基板成長的趨勢。 使用具有(0002)優選方向的氧化鋅薄膜作為基板時，氧化鋅奈米線可以垂直成長於基版上。 當氧化鋅奈米線成長於氧化鋅薄膜/(0001)藍寶石的基版時，不僅垂直基板成長，在水平方向也是有磊晶的關係。 當使用(0001)藍寶石基板時,我們發現氧化鋅奈米線的成長方向在水平方向的投影具有三重對稱性，造成的原因為氧化鋅與藍寶石基板有磊晶的關係。

在奈米線的光學特性研究方面,我們使用變溫光激發光光譜得到自由激子複合放光主導著室溫的光激發光光譜,在低溫時則為束縛激子複合放光所主導。 我們也得到了自由激子與束縛激子的束縛能。 另一方面, 從變溫光激發光光譜可得到氧化鋅奈米線的輻射躍遷與縱光聲子極化場之耦合強度。 利用激子極子的

形成，我們可以解釋為什麼在氧化鋅奈米線裡，自由激子與縱光聲子的交互作用會遠大於其他的束縛激子之作用。 在氧化鋅奈米線裡很強的激子與聲子耦合不但影響 Haung–Ray S 因子而且影響第一階縱聲子能量，這個結果可歸咎於激子極子的形成。 除此之外，我們也發現了位於光子能量 2.5 電子伏特的缺陷發光主要來自於氧化鋅奈米線體的側壁。 我們也驗證了氧化鋅奈米線的光激發光的受激輻射放光以及雷射的產生。 雷射的產生是由於光子在被散射多次，則會誘發出更多的同調光子，進而達到了隨機雷射的產生。

最後，我們也成功的製備出氧化鋅為軸心而氧化鎂包覆於外的奈米線。 利用熱擴散的方法，可以將其光激發光光譜位置調變至更高能量。 除此之外，我們也驗證出氧化鎂鋅奈米線受激輻射放光的行為。

Optical properties of ZnO-based nanowires grown by vapor transport method

Student: Hsu-Cheng Hsu   Advisor: Dr. Wen-Feng Hsieh

Department of Photonics & Institute of Electro-Optical Engineering
National Chiao Tung University

Abstract

We successfully fabricate ZnO-based nanowires by vapor transport method. The optical properties of ZnO nanowires are also investigated. Hexagonal ZnO nanowires have been selectively synthesized via vapor-solid process without gold catalysis on a pre-coated ZnO buffer layer. The presence of nanometer-sized pits or hills on the surface of ZnO buffer layer provides nucleation sites to which the zinc vapor is transferred and condensed. Followed by immediate oxidation the ZnO nanowires were grown on the buffer layer. ZnO nanowires can be also synthesized on porous silicon substrates with different porosities via the vapor-liquid-solid method. The texture coefficient analyzed from the XRD spectra indicates that the nanowires are more highly orientated on the appropriate porosity of porous silicon substrate than on the smooth surface of silicon. Vertically well-aligned ZnO nanorods are synthesized without employing any metal catalysts on various substrates including glass, Si(111), and saphire(0001), which were pre-coated with c-oriented ZnO buffer layers, by simple chemical vapor deposition. The epitaxial relationship between ZnO nanowires and various substrates is discussed in detail.

From the temperature dependent photoluminescence spectra, we deduce the activation energies of free and bound excitons. Besides a strong ultra-violet emission at 3.26 eV observed at room temperature, the coupling strength of the radiative transition to LO-phonon polarization field was deduced in use of the Huang-Rhys factor from low temperature photoluminescence spectra to show that single crystalline ZnO nanorods.

The coupling strength of the radiative transition of hexagonal ZnO nanowires to the longitudinal optic (LO) phonon polarization field is deduced from temperature dependent photoluminescence spectra. An excitonic polaron formation is discussed to explain why the interaction of free excitons with LO phonons in ZnO nanowires is much stronger than that of bound excitons with LO phonons. The strong exciton-phonon coupling in ZnO nanowires affects not only the Haung-Ray S factor but also the FXA-1LO phonon energy spacing, which can be explained by the excitonic polaron formation.

We report room-temperature ultraviolet stimulated emission and lasing from optically pumped high-quality ZnO nanowires. Emission due to the exciton-exciton scattering process shows apparent stimulated-emission behavior. Several sharp peaks associated with random laser action are seen under high pumping intensity. The mechanism of laser emission is attributed to coherent multiple scattering among the random-growth oriented nanowires. The characteristic cavity length is determined by the Fourier transform of the lasing spectrum.

Finally, we demonstrate a simple method to achieve the bandgap engineering in core-shell ZnO-MgO nanowires by using Mg diffusion. Furthermore, we report the observation of stimulated emission (SE) from optically pumped ZnMgO nanowires.

Contents

List of Figures

List of Tables

Chapter 1 Introduction

1.1 A general of one-dimensional ZnO nanostructure

Ever since the discovery of carbon nanotubes by Iijima [1], there has been great interest in the synthesis and characterization of other one-dimensional (1D) structures. Nanorods and nanowires, nanobelts and nanotubes have become important fundamental building blocks for nanophotonic devices and offer substantial promise for integrated nanosystems.[2,3] 1D nanostructures are useful materials for investigating the dependence of electrical and thermal transport or mechanical properties on dimensionality and size reduction (or quantum confinement). They are also expected to play an important role as both interconnects and functional units in fabricating electronic, optoelectronic, electrochemical and electromechanical nanodevices. Several nice review articles have been written on synthesis, characterization, and applications of one-dimensional inorganic nanostructures. [4-6]

ZnO is a wide band gap semiconductor (3.37 eV) with a large exciton binding energy (60 meV) which is much larger than thatof GaN and the thermal energy at room temperature (21 meV), and therefore enables stable existence of excitons at room temperature even up to 550^oC. In this regard, ZnO has been recognized as a promising photonic material in the blue-UV region. The stable excitons could lead to laser action based on their recombination even at temperatures well above room temperature. Optically pumped UV lasing have been demonstrated at room temperature using high quality ZnO films.[7,8] The excitonic gain close to 300 cm^{-1} at a fluence of 3.8 μJ/cm^2 was achieved.[9] ZnO thin films are expected to have higher quantum efficiency in UV semiconductor laser than GaN.

Recently, UV lasing for ZnO nanowires has also been demonstrated at room

temperature [10]. It is expected that a lower threshold optical pumping density for lasing is due to the carrier confinement effect in one dimensional nanowires. Nanostructures composed of ZnO nanowires are also being intensively investigated because they possess a combination of attractive optical [11], mechanical [12], and magnetic properties. [13] ZnO nanowires have been evaluated for potential applications as UV laser[14], light-emitting diodes[15], and UV photodetectors[16][17], array gratings. [18] Therefore, the ZnO nanowire has become one of the most promising elemental building blocks in nanotechnology applications. In recent years, much effort has been devoted to developing various 1D ZnO nanostructures. Vapour-liquid-solid (VLS) and vapour-solid (VS) mechanisms for growth of ZnO nanowires are well recognized, and have been used. 1D semiconductor nanostructures have also been obtained via laser ablation-catalytic growth, oxide-assisted growth, template-induced growth, solution-liquid-solid growth in organic solvents and metal-organic chemical vapour deposition (MOCVD). Moreover, the observations of quantum confinement [19] and the discrete energy levels [20] are demonstrated in ZnO/ZnMgO nanorod heterostructures. The ZnO nanowires can serve as excellent photon emitters as well as good photon emitters due to their sharp tips.[21-24]

To date, most of the work on ZnO 1D nanostructures has focused on the synthesis methods. For application of nano-photonics and electronics, it is needed to create ZnO nanowires that are selective area growth, highly aligned and orientation-ordered on substrates. The fundamental optical properties, including the origin of luminescence, carrier-carrier interaction, stimulated emission and lasing are also needed to understand. Furthermore, band-gap engineering, which is the process of controlling or altering the band gap, and fabrication of heterostructure or quantum structures of ZnO-based nanowires are important issues.

1.2 Basic properties of ZnO

The wurtzite structure of the ZnO crystal is shown in Fig. 1-1.　ZnO is a crystal of hexagonal structure with the lattice constant of a=3.249 Å, c=5.207 Å.
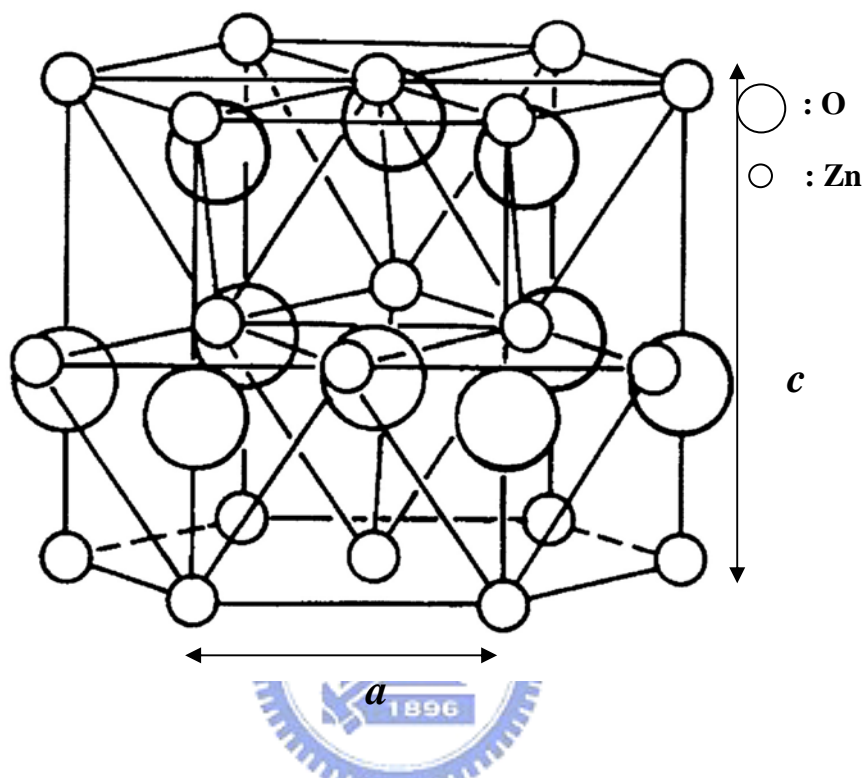
Fig. 1-1 Wurtzite structure

The basic properties of ZnO for optoelectronic applications can be obtained by examining Table I, which compares the relevant material properties of ZnO with those of other wide band gap semiconductors.　The notable properties are the large bond strength (indicated by the cohesive energy) and the melting point and the extreme stability of excitons (indicated by the large exciton binding energy).　ZnO is one of the ''hardest'' materials in the II-VI compound family.　The stability of the exciton makes ZnO a promising material for the realization of excitonic laser gain at RT.　The excitonic lasing have been demonstrated for ZnO-based thin films, quantum well, and nanowires.

TABLE I. Comparison of properties of ZnO with those of other wide band gap semiconductors.[25]

| Material | Crystal structure | Lattice constants | | Band gap energy at RT | Cohesive energy | Melting point | Exciton binding energy | Dielectric constants | |
		a (Å)	c (Å)	E_g (eV)	E_{coh} (eV)	T_m (K)	E_b (meV)	$\varepsilon(0)$	$\varepsilon(\infty)$
ZnO	Wurtzie	3.249	5.207	3.37	1.89	2248	60	8.75	3.75
ZnS	Wurtzie	3.823	6.261	3.8	1.59	2103	39	9.6	5.7
ZnSe	Zinc blende	5.668	⋯	2.70	1.29	1793	20	9.1	6.3
GaN	Wurtzie	3.189	5.185	3.39	2.24	1973	21	8.9	5.35
$6H$-SiC	Wurtzie	3.081	15.117	2.86(ind.)	3.17	>2100	⋯	9.66	6.52

1.3 Organization of the dissertation

This dissertation is organized as follow. Chapter 2 presents a brief review of growth and characterization techniques. In Chapter 3, the growth of the ZnO nanowires on varies substrates, including Al_2O_3, porous Si, ZnO/Si(111) films and ZnO/sapphires(111), are demonstrated. I also explain the growth mechanism and the epaxitial relationship between the nanowires and the substrates. In Chapter 4, the fundamental luminescence of the ZnO nanowires is investigated. The binding energies of the free and donor bound excitons are obtained by temperature dependent photoluminescence. The stimulated emission and laser action at room temperature are demonstrated. In Chapter 5, I discuss the fabrication of the ternary ZnMgO nanowires and their optical properties. The band gap engineering of the ZnMgO nanowires is demonstrated by annealing treatment. The stimulated emission from ZnMgO nanowires will be discussed. In the final Chapter 6, I conclude the investigations on the ZnO-based nanowires and propose the several topics of the future work.

References

[1] S. Iijima, *Nature* 354, 56 (1991).

[2] X. F. Duan, Y. Huang, R. Agarwal, and C. M. Lieber, *Nature* **421**, 241(2003).

[3] S. S. Wong, E. Joselevich, A. T. Woolley, C. L. Cheung, and C. M. Lieber**,** *Nature* **394**, 52 (1998).

[4] Y. N. Xia , P. D. Yang , Y. G. Sun , Y. Y. Wu , B. Mayers , B. Gates , Y. D. Yin, F. Kim ,and H.Q. Yan, *Adv. Mater.* **15,** 353 (2003).

[5] C. N. R. Rao, F. L. Deepak, Gautam Gundiah and A. Govindaraj, *Prog. Solid State Chem.* 31, 5 (2003).

[6] Z. L. Wang, *Adv. Mater.*, 15, 432 (2003).

[7] D. M. Bagnall, Y. F. Chen, Z. Zhu, T. Yao, S. Koyama, M. Y. Shen, T. Goto, *Appl. Phys. Lett.* 70, 2230 (1997).

[8] Z. K. Tang, G. K. L. Wong, P. Yu, M. Kawasaki, A. Ohtomo, H. Koinuma, Y. Segawa, *Appl. Phys. Lett.* 72, 3270 (1998).

[9] P. Yu, Z. K. Tang, G. K. L. Wong, M. Kawasaki, A. Ohtomo, H. Koinuma, Y. Segawa, *J. Crys. Growth* 185, 601 (1998).

[10] M. H. Huang, S. Mao, H. Feick, H. Q. Yan, Y. Y. Wu, H. Kind, E. Weber, R. Russo, and P. D. Yang, *Science* **292,** 1897 (2001).

[11] M. Law, J. Goldberger, P. D. Yang, *Rev. Mater. Res.* 34, 122 (2004).

[12] X. D. Bai, P. X. Gao, Z. L. Wang, and E. G. Wang, *Appl. Phys. Lett.* **82**, 4806 (2003).

[13] Y. W. Chang, D. B. Wang, X. H. Luo, X. Y. Xu, X. H. Chen, L. Li, C. P. Chen, R. M. Wang, J. Xu, and D. P. Yu, *Appl. Phys. Lett.* **83**, 4020 (2003).

[14] P. Yang, H. Yan, S. Mao, R. Russo, J. Johnson, R. Saykally, N. Morris, J.

Pham, R. He, and H.-J Choi, *Adv. Funct. Mater.* **12**, 323 (2002).

[15] C. H. Liu, J. A. Zapien, Y. Yao, X. M. Meng, C. S. Lee, S. S. Fan, Y. Lifshitz, and S. T. Lee, *Adv. Mater.* **15**, 838 (2003).

[16] H. Kind, H. Yan, B. Messer, M. Law, and P. Yang, *Adv. Mater.* **14**, 158 (2002).

[17] K. Keem, H. Kim, G.-T. Kim, J. S. Lee, B. Min, K. Cho, M.-Y. Sung, and S. Kim, *Appl. Phys. Lett.* **84**, 4376, (2004).

[18] Z. W. Pan, S. M. Mahurin, S. Dai, D. H. Lowndes, *Nano Lett.* 5, 723 (2005).

[19] W. I. Park, G. C. Yi, M. Kim, S. J. Pennycook, *Adv. Mater.* 15, 526 (2003).

[20] T. Yatsui, J. Lim, M. Ohtsu, S. J. An, G. C. Yi, *Appl. Phys. Lett.* 85, 727 (2004).

[21] C. J. Lee, T. J. Lee, S.C. Lyu, Y. Zhang, H. Ruh, H. J. Lee, *Appl. Phys. Lett.* 81, 3648 (2002).

[22] Y. W. Zhu, H. Z. Zhang, X. C. Sun, S. Q. Feng, J. Xu, Q. Zhao, B. Xiang, R. M. Wang , D. P. Yu, *Appl. Phys. Lett.* 83, 144 (2003).

[23] Y. K. Tseng, C. J. Huang, H. M. Cheng, I. N. Lin, K. S. Liu, I. C. Chen, *Adv. Fun. Mater.* 13 811 (2003).

[24] S. Y. Li, P. Lin, C. Y. Lee, T. Y. Tseng, *J. Appl. Phys.* 95, 3711 (2004).

[25] Y. F. Chen, D. M. Bagnall, H. J. Koh, K. T. Park, K. Hiraga , Z. Q. Zhu, T. Yao, *J. Appl. Phys.* 84 3912 (1998).

Chapter 2 Growth and characterization techniques

2.1 Growth of ZnO nanowires

Previous effort in the synthesis of ZnO nanowires and nanorods have employed vapor-phase transport via a vapor–liquid–solid (VLS) mechanism [1,2] and vapor solid mechanism [3,4], gas reaction [5] and oxidation of metal in the pores of anodic alumina templates [6,7]. In this research, the vapor-phase transport was used to grow the nanowires. The detailed growth mechanisms of the nanowires are discussed as follows.

2.1.1 Vapor-Liquid-Solid (VLS) Methods

Among all vapor based methods, the VLS methods seems to be the most successful for fabricating nanowires with single crystalline structures and in relatively large quantities. This process was first developed by Wagner *et al.* to produce Si single crystalline micro-whiskers in 1960s [8], and recently re-examined successfully by Lieber [9] and Yang [3,4]. The key factor is needed to deposit metal clusters such as Fe, Co, Ni, and Au as the catalysts. A typical VLS process starts with the dissolution of gaseous reactants into nano-sized liquid droplets of catalyst metal while the liquid droplets are supersaturated with the guest material, followed by nucleation and growth of single crystalline nanorods and then nanowires. The 1D growth is mainly induced and dictated by the liquid droplets, whose size remains essentially unchanged during the entire process of nanowire growth. In the sense, each of liquid droplets serves as a soft template to strictly limit the lateral growth of an individual nanowire. As a major requirement, there should exist a good solvent capable of

forming liquid alloy with the target material, ideally they should be able to form eutectic compounds.   All of the major steps involved in a VLS process is schematically illustrated in Fig. 2-1(a) [10].   Based on the Zn-Au binary phase diagram as shown in Fig. 2-1(b), Zn and Au form liquid alloys when the temperature is raised above the eutectic point.   Once the liquid droplet is supersaturated with Zn, growth of nanowire takes place at the solid-liquid interface.   The vapor pressure of Zn in the chemical-vapor-deposition system has to be kept sufficiently low so that the second ordinary nucleation will be completely suppressed.   Both physical methods (thermal evaporation and laser ablation) and chemical methods (chemical vapor transport and deposition) have been employed to generate the vapor species required for the growth of nanowires, and no significant difference was found in the quality of nanowires produced by these methods.
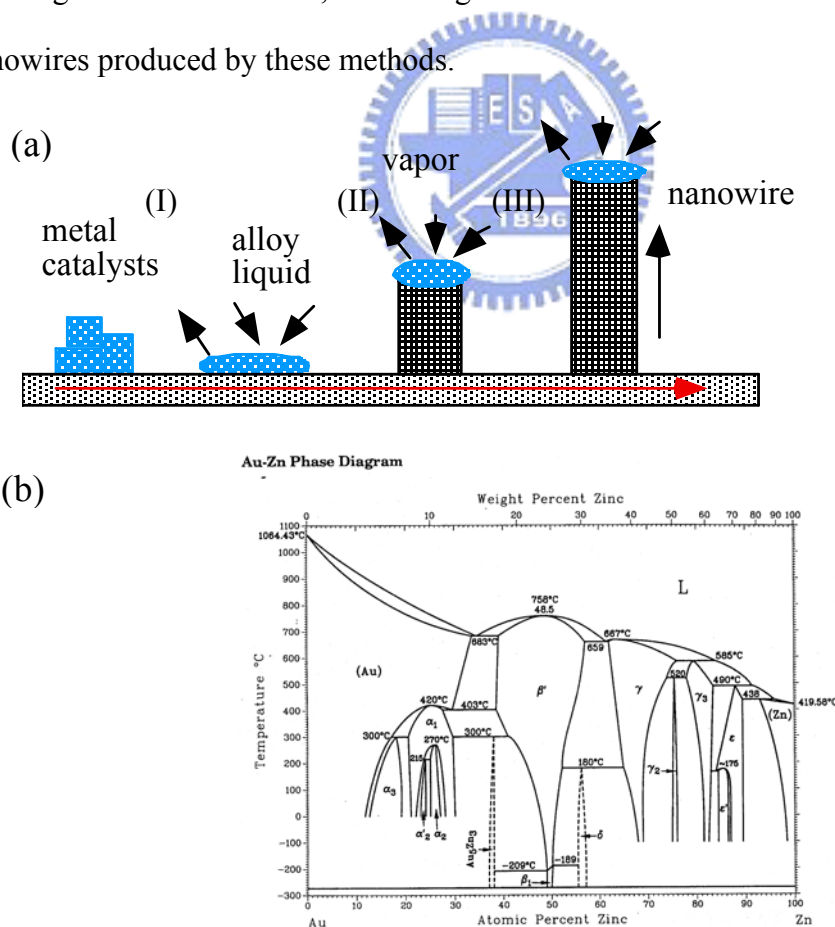
Fig. 2-1 (a) Schematic illustration of vapor-liquid-solid growth mechanism including three stages (I) alloying, (II) nucleation and (III) axial growth.   (b) Au-Zn phase diagram.

2.1.2 Vapor-Solid method

The vapor–solid (VS) method for nanowires growth also holds for the growth of 1D nanomaterials.   In this process, evaporation, chemical reduction or gaseous reaction first generates the vapor.   The vapor is subsequently transported and condensed onto a substrate.   The VS method has been used to prepare whiskers of oxide, as well as metals with micrometer diameters.   It is, therefore, possible to synthesize the 1D nanostructures if one can control the nucleation and the subsequent growth process.

2.2 Characterization techniques

2.2.1 X-ray diffraction [11]

The peaks of an x-ray diffraction pattern are directly related to the atomic distances.   Consider an incident monochromatic x-ray beam interacting with the atoms arranged in a periodic manner as shown in 2-dimension in Fig. 2-2.   The atoms, represented as circles in the graph forming different sets of planes in the crystal.   For a given set of lattice planes with an inter-plane distance of d, the condition for a diffraction (peak) to occur can be simply written as

$$2d \sin \theta = n\lambda \tag{2.1}$$

which is known as the Bragg's law.   In this equation, λ is the wavelength of the x-ray, θ the diffraction angle, and n an integer representing the order of the diffraction peak.

$$2\mathrm{dsin}\,\theta = \mathrm{n}\,\lambda$$

λ
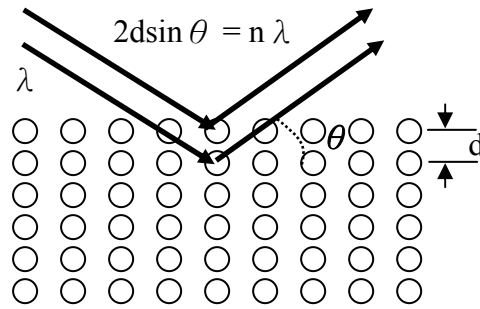
Bragg's Law

Fig. 2-2 X-ray diffraction from 2-dimensional periodic lattices

Let's consider hexagonal unit cell as shown in Fig. 2-3 which is characterized by lattice parameters a and c, the equation representing the plane spacing for the hexagonal structure is

$$\frac{1}{d^2} = \frac{4}{3}\left(\frac{h^2 + hk + k^2}{a^2}\right) + \frac{l^2}{c^2}. \tag{2.2}$$

Combining Eq. (2.1) with (2.2) yields:

$$\frac{1}{d^2} = \frac{4}{3}\left(\frac{h^2 + hk + k^2}{a^2}\right) + \frac{l^2}{c^2} = \left(\frac{2\sin\theta}{\lambda}\right)^2 \tag{2.3}$$

and rearranging to give

$$\sin^2\theta = \frac{\lambda^2}{4}\left[\frac{4}{3}\left(\frac{h^2 + hk + k^2}{a^2}\right) + \frac{l^2}{c^2}\right]. \tag{2.4}$$

Thus, the lattice parameters can be estimated from (2.4).
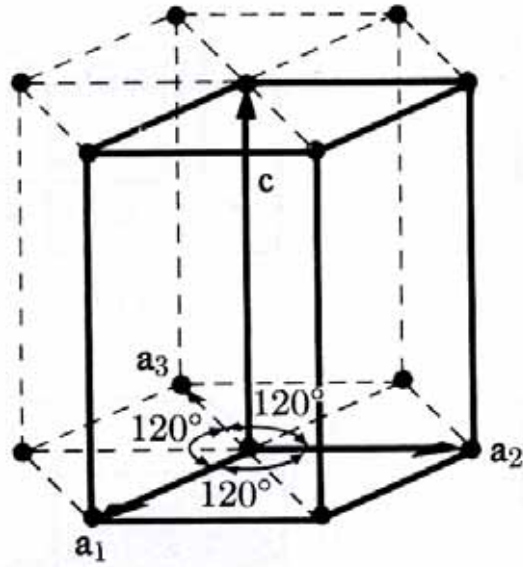
(a)

Fig. 2-3 The hexagonal unit cell.

2.2.2 Raman characterization

Raman scattering is an inelastic scattering process. When light encounters the surface, most of the light is reflected, transmitted, absorbed, or Rayleigh scattered, because of the first-order elastic interaction with electrons, phonons, and impurities. There is no change in photon frequency. However a small portion of the light beam interacts inelastically with phonon modes, producing outgoing photons whose frequencies are shifted from the incoming ones. These are the Raman-scattered photons. They gain energy by absorbing a phonon (anti-Stokes shifted), or lose energy by emitting one (Stokes shifted), according to the energy and momentum conservation rules:

$$\omega_s = \omega_i \pm \Omega, \qquad\qquad (2\text{-}5)$$

$$q_s = q_i \pm K \quad , \qquad\qquad (2\text{-}6)$$

11

where ω_i and ω_s are the incoming and scattered photon frequencies. q_s and q_i are the incoming and scattered photon wavevectors, and Ω and K are the phonon frequency and wavevector, respectively.   Raman scattering is inherently a weak process, but lasers provide enough power that the spectra can be routinely measured.

All of the Raman parameter-band frequencies and intensities, line-shape and line-width, as well as polarization behavior can be used to characterize the lattice and impurities.   The intensity gives information about crystallinity.   The line-width increases when the crystal contains defects or disorders, because they would damp the crystal vibration to shorten the phonon lifetime or relax the selection rules for momentum conservation in Raman process.   All these capabilities can be used as a judgment for layered microstructure as well as bulk, subject only to the limitation that the penetration depth of the exciting radiation range from a few hundred nanometers to a micrometer.
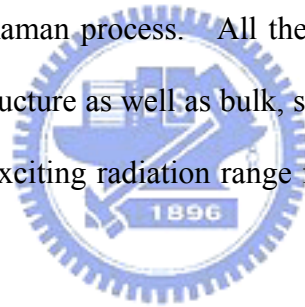
2.2.3 Raman modes of ZnO

Wurtzite ZnO belongs to the C_{6v}^4 ($P6_3mc$) space group.   At the Γ point of the Brillouin zone, the group theory predicts the existence of the following optic modes: $\Gamma_{opt} = A_1 + 2B_1 + E_1 + 2E_2$.   These two B_1 modes, B_1(low) and B_1(high), are silent, and A_1, E_1, and E_2 modes are Raman active.   The displacement vectors of the phonon normal modes are illustrated in Fig. 2-4 [12].   In addition, A_1 and E_1 are also infrared active and split into longitudinal and transverse optical (LO and TO) components.   The frequencies of these modes assigned in the literature [13] are listed in Table 2.1.
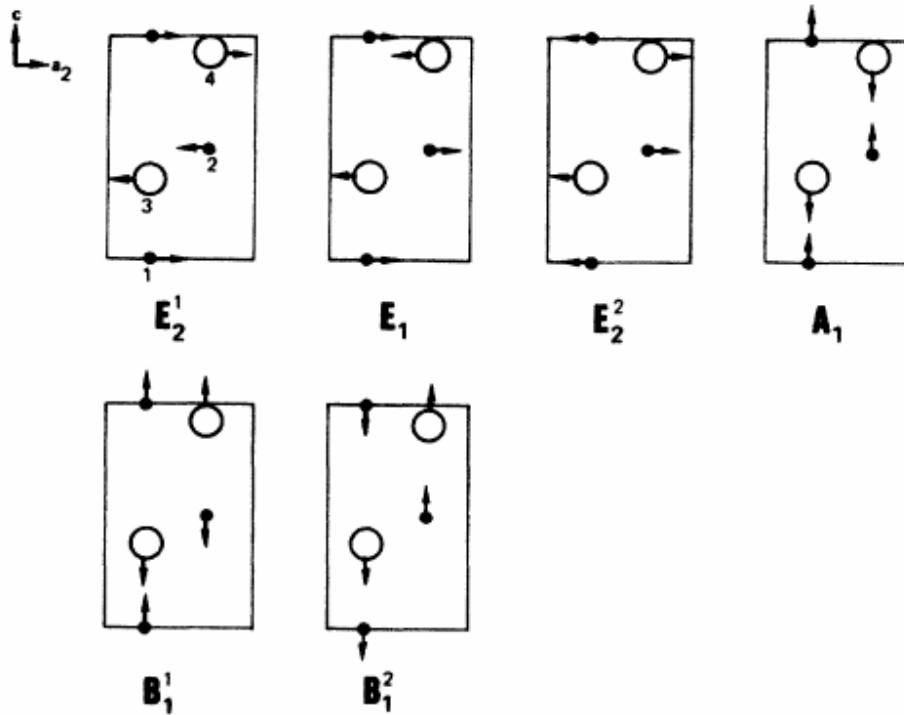
Fig. 2-4   Displacement vectors for the five Raman modes of the wurtzite structure. [12]
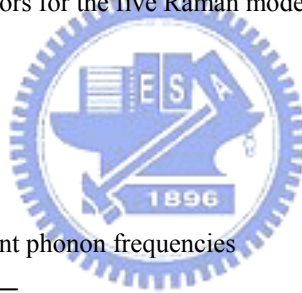
Table 1 Raman-active w-ZnO Γ -point phonon frequencies

Mode	frequency (cm^{-1}) [13]
E_2(low)	101
E_2 (high)	437
A_1(TO)	380
E_1(TO)	408
A_1(LO)	574
E_1(LO)	584

2.3 Photoluminescence characterization [14-16]

Photoluminescence (PL) is one of the most useful optical methods for the semiconductor industry, with its powerful and sensitive ability to characterize impurities and defects in semiconductors, which affect material quality and device performance.   To control crystal purity is crucial in many optical applications, such as laser action, optical gain, and active optical devices.   A given impurity produces a set of characteristic spectral features.   The fingerprint identifies the impurity type, and often several different impurities can be seen in a single PL spectrum.   And the linewidth of PL peak is an indication of sample quality and crystallinity, although such analysis has not yet become highly quantitative.

2.3.1 Fundamental optical transitions

Since the PL emission requires that the system be in a nonequilibrium condition, and some means of excitation is needed to act on the semiconductor to produce hole-electron pairs.   We consider the fundamental transitions, those occurring at or near the band edges.

The ground state of the electronic system of a perfect semiconductor is a completely filled valance band and a completely empty conduction band.   We can define this state as the "zero" energy or "vacuum" state.   If we start from the above-defined ground state and excite one electron to the conduction band, we simultaneously create a hole in the valance band.   In this sense an optical excitation is a two-particle transition.   The same is true for the recombination process.   An electron in the conduction band can return radiatively or nonradiatively into the valance band only if there is a free space, i.e., a hole.   Two quasi-particles are annihilated in the recombination process.   What we need for the understanding of the optical properties of the electronic system of a semiconductor is therefore a

description of the excited states of N-particle problem. The quanta of these excitations are called "excitons". Here we will consider the so-called *Wannier excitons* more specifically. In Wannier excitons, the Bohr radius (i.e. the mean distance between electron and hole) is larger in comparison to the length of the lattice unit cell. This condition is met in most II-VI, III-V, and column IV semiconductors.

2.3.1.1 Wannier excitons

Using the effective mass approximation, Fig. 2-5 suggests that the Coulomb interaction between electron and hole leads to a hydrogen-like problem with a Coulomb potential term $\dfrac{-e^2}{4\pi\varepsilon_0\varepsilon|r_e - r_h|}$.

Indeed excitons in semiconductors form, to a good approximation, a hydrogen or positronium like series of states below the gap. For a simple parabolic band in a direct-gap semiconductor one can separate the relative motion of electron and hole and the motion of the center of mass. This leads to the dispersion relation of exciton as shown in Fig. 2-6

$$E_{ex}(n_B, K) = E_g - Ry^* \frac{1}{n_B^2} + \frac{\hbar^2 K^2}{2M} \tag{2-9}$$

where n_B= 1,2,3… is the principal quantum number, $Ry^* = 13.6 \dfrac{\mu}{m_0}\dfrac{1}{\varepsilon^2}$ is the exciton binding energy, M=m_e+m_h, and K=k_e+k_h are translational mass and wave vector of the exciton, respectively.
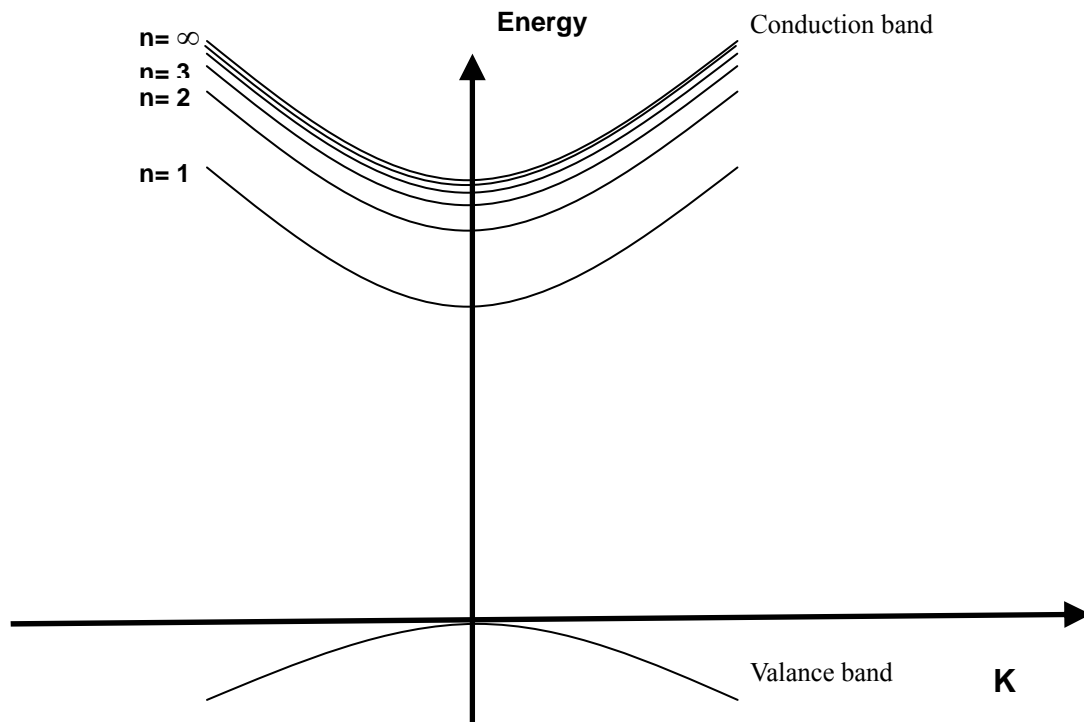
Fig. 2-5   The exciton dispersion in a two-particle (electron-hole) excitation diagram of the entire crystal.   The crystal ground state (zero energy and zero momentum) is the point at the origin.   Different parabolas represent the kinetic energy bands associated with different terms of the excitonic series.[14]

2.3.1.2 Bound excitons

A real crystal is never perfect.   Imperfections such as ion vacancies, interstitials, or substitutional atoms (either native or intentionally introduced) exist in densities ranging from $n_i < 10^{12}$ cm^{-3} in ultrapure crystals.   The imperfections can attract excitons that become localized at the defect sites to form bound excitons.   The binding energy of the exciton to the defect is often quite small, typically a few meV. Therefore, the bound excitons are best observed at very low temperatures.

An exciton may be bound to a donor, which is a substitutional atom with a higher number of valance electrons compared with the host atom, or to an acceptor, a substitutional atom with a lower number of valance electrons.   Donors contribute excess electrons to the crystal, while acceptors tend to capture electrons or

equivalently donate holes.   Donor or acceptor atoms may be electrically charged or neutrals.   When the donor atom has given away its initial extra valence electrons, it becomes positively charged and it referred to as an ionized donor.   Similarly, when an acceptor atom has captured an electron (or equivalently released a hole), it has a negative charge and is called an ionized acceptor.   In contrast, a neutral donor or acceptor has no charge, since it has kept its original number of valance electrons. Excitons may get bound to either an ionized donor or acceptor, or a neutral donor or acceptor by forming complexes represented schematically in Fig. 2-6.   In many crystals, the binding energy of the exciton to a neutral donor or acceptor is close to tenth of the donor or acceptor ionization energy, which is the energy required to free the extra valence electron of a neutral donor, or the energy to free a hole (to accept an electron) in a neutral acceptor.   Bound excitons are characterized by more sharply peaked emission which occurs at a lower energy than the corresponding free exctions, which is due to reduced kinetic broadening, since the bound exciton is spatially localized at an impurity.   The emitted energy of bound energy E_{BE} is

$$E_{BE} = E_g - E_E^F - E_E^B,$$ (2-10)

where E_E^B is energy necessary to bind the exciton to the defect center and E_E^F is the binding energy of the free exciton.   Therefore, luminescence of bound exciton typically dominates the near band edge emission and occurs on the low energy side of the free exciton emission.
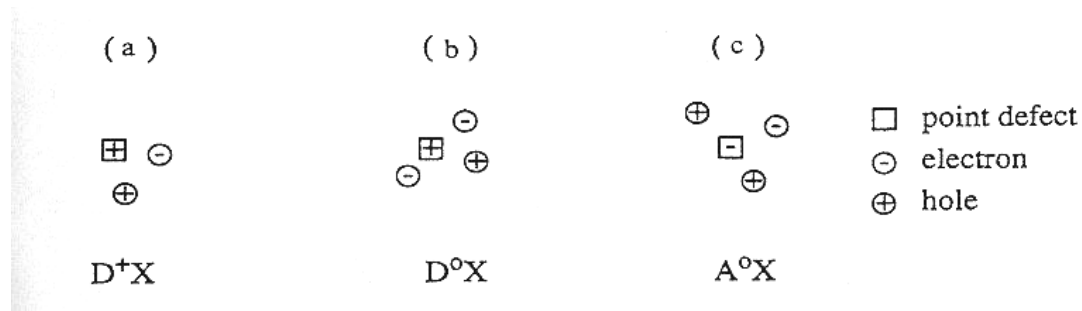
Fig. 2-6 Visualization of (a) an exciton bound to an ionized donor, (b) a neutral donor, and (c) a neutral acceptor. [14]

2.3.1.3 Donor-Acceptor Pairs (DAP)

Donors and acceptors can form pairs and act as stationary molecules imbedded in the host crystal. The coulomb interaction between a donor and an acceptor results in a lowering of their binding energies. In the donor-acceptor pair case it is convenient to consider only the separation between the donor and the acceptor level:

$$E_{pair} = E_g - (E_D + E_A) + \frac{q^2}{\varepsilon r} , \qquad (2\text{-}11)$$

where r is the donor-acceptor pair separation, E_D and E_A are the respective ionization energies of the donor and the acceptor as the isolated impurities.

2.3.1.4 Deep transitions

By deep transition we shall mean either the transition of an electron from the conduction band to an acceptor state or a transition from a donor to the valence band in Fig. 2-7. Such transition emits a photon $h\nu = E_g - E_i$ for direct transition and $h\nu = E_g - E_i - E_p$, if the transition is indirect and involves a phonon of energy E_p. Hence the deep transitions can be distinguished as (1) conduction-band-to-acceptor transition which produces an emission peak at $h\nu = E_g - E_A$, and (2) donor-to-valence-band transition which produces emission peak at the higher photon energy $h\nu = E_g - E_D$.

18
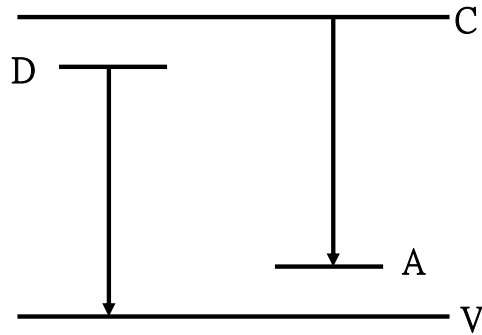
Fig. 2-7 Radiative transition between a band and an impurity state.

2.3.2 Influence of high excited light intensity

The PL conditions as mentioned above are excited by low excitation light intensity.   At low excitation light intensity (low density regime in Fig. 2-8), the PL properties are determined by single electron-hole pairs, either in the exciton states or in the continuum.   Higher excitation intensity (intermediate density regime in Fig. 2-10) makes more excitons; such condition would lead to the exciton inelastic scattering processes and form the biexciton.   The scattering processes may lead to a collision-broadening of the exciton resonances and to the appearance of new luminescence bands, to an excitation-induced increase of absorption, to bleaching, or to optical amplification, i.e., to gain or negative absorption depending on the excitation conditions.   If we pump the sample even harder, we leave the intermediate and arrive at the high density regime in Fig. 2-6, where the excitons lose their identity as individual quasiparticles and where a new collective phase is formed which is known as the electron-hole plasma (EHP).
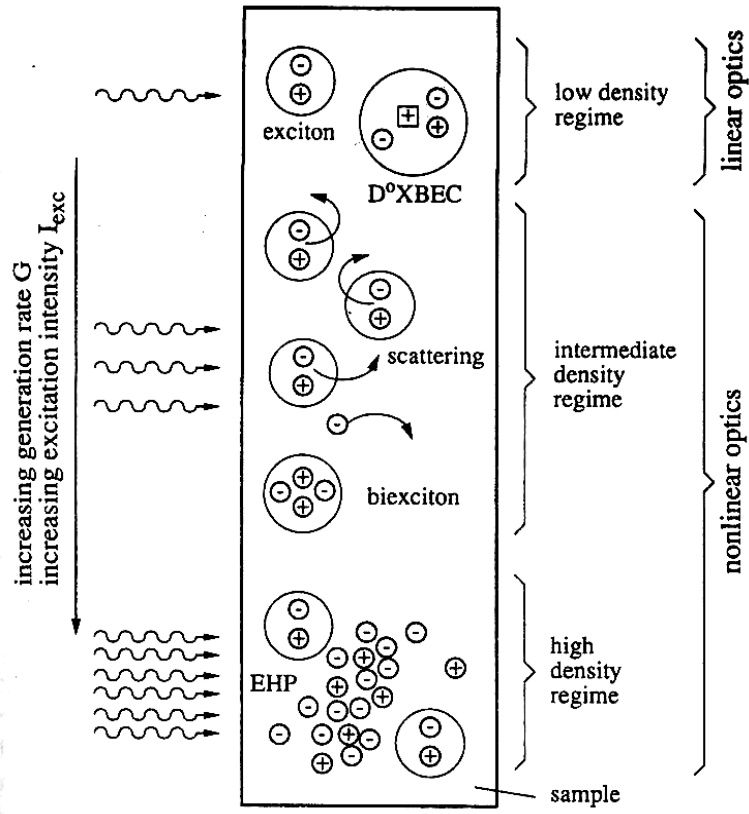
Fig. 2-8 The general scenario for many-particle effects in semiconductors. [14]

2.3.2.1 Inelastic scattering processes

In the inelastic scattering processes, an exciton is scattered into a higher excited state, while another is scattered to the photon-like part of the polariton dispersion and leaves the sample with high probability to release luminescence photon, when this photon-like particle hits the surface of the sample. This process is shown schematically in Fig. 2-9 and the photons emit in such a process have energies E_n given by Ref. 14

$$E_n = E_{ex} - E_b^{ex}\left(1 - \frac{1}{n^2}\right) - \frac{3}{2}kT \ , \qquad (2\text{-}7)$$

where n = 2, 3, 4,..., E_b^{ex} =60meV is the binding energy of the free exciton of ZnO, and kT is the thermal energy. The resulting emission bands are usually called P-bands with an index given by n.
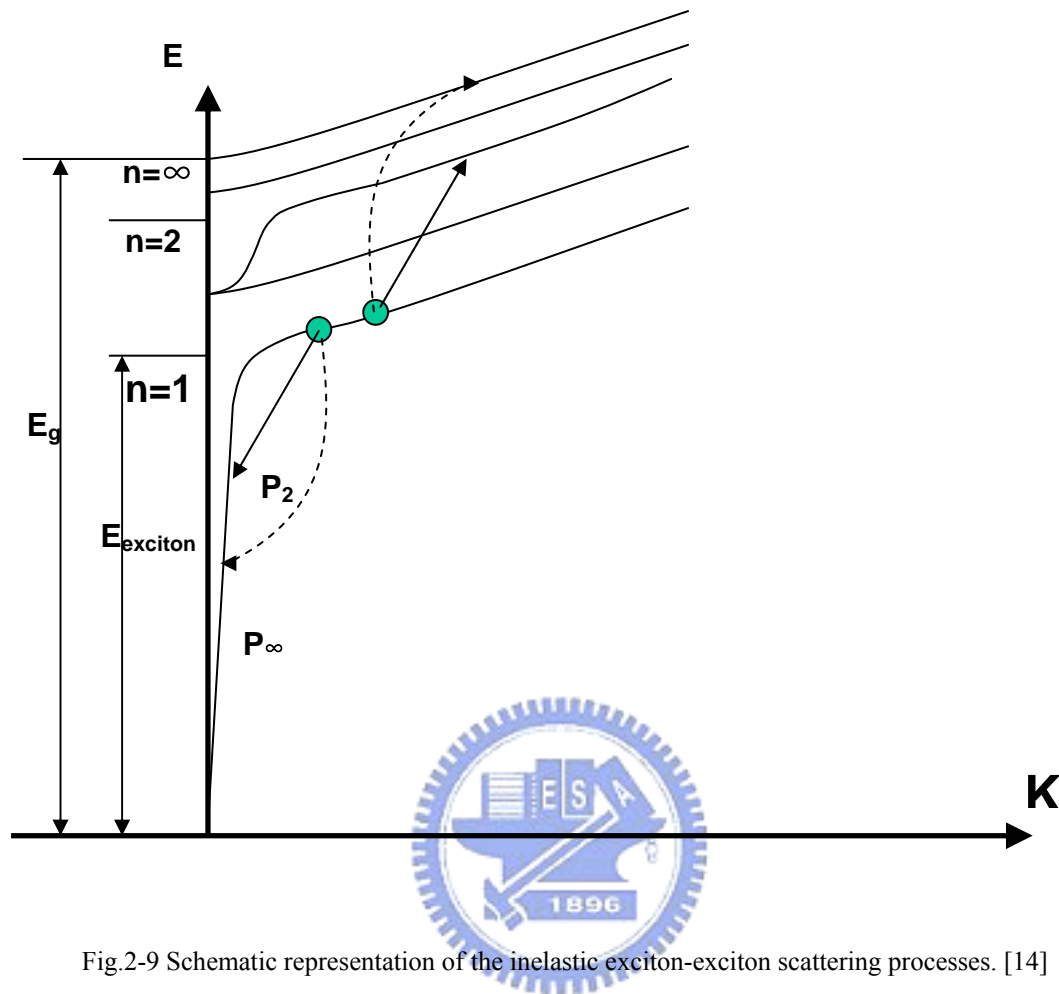
Fig.2-9 Schematic representation of the inelastic exciton-exciton scattering processes. [14]

2.3.2.2 Electron-Hole Plasma

In the high density regime, the density of electron-hole pairs n_p is at least in

parts of the excited volume so high that their average distance is comparable to

or smaller than their Bohr radius, i.e., we reach a "critical density" n_p^c in an

EHP, given to a first approximation by $a_B^3 n_p^c \approx 1$. We can no longer say that a

certain electron is bound to a certain hole; instead, we have the new collective

EHP phase. The transition to an EHP is connected with very strong changes of

the electronic excitations and the optical properties of semiconductors.

References

[1] M. H. Huang, Y. Wu, H. Feick, N. Tran, E. Weber and P. D. Yang. *Adv Mater* **13,** 113 (2001).

[2] M. H. Huang, S. Mao, H. Feick, H. Yun, Y. Wu, H. Kind, E. Weber, R. Russo, and P. D.Yang. *Science* **292,** 1897 (2001).

[3] Z. W. Pan, Z. R. Dai and Z. L. Wang, *Science*, **291** 1947 (2001).

[4] J. Q. Hu, Q. Li, N. B. Wong, C. S. Lee, and S. T. Lee, *Chem. Mater.* **14** (2002) 1216.

[5] J. C.Hulteen, C. R. Martin, *J. Mater. Chem.*, Volume: 7, (1997), p. 1075

[6] Y. Li, G. W. Meng, L. D. Zhang, F. Phillipp, *Appl. Phys. Lett.* 76, 2011 (2000).

[7] C. H. Liu, J. A. Zapien, Y. Yao, X.M. Meng, C. S. Lee, S. S. Fan, Y. Lifshitz, S. T. Lee, *Adv. Mater.* 15, 838 (2003).

[8] R. S. Wagner, and W.C. Ellis, *Appl. Phys. Lett.*, **4**, 89(1964)

[9] A. M. Morales and C. M Lieber, *Science,* **279**,208 (1998).

[10] Y. Wu and P. Yang. *J. Am. Chem. Soc.* **123**, pp. 3165 (2001).

[11] B. D. Cullity, *Elements of X-ray diffraction*, 2 nd ed, (Addison Wesley, Canada, 1978).

[12] A. P. Jephcoat, R. J. Hemley, H. K. Mao, R. E. Cohen and M. J. Mehl, Phys. Rev. B 37, 4727 (1988).

[13] J. M. Calleja and M. Cardona, Phys. Rev. B **16**, 3753 (1977).

[14] C. F. Klingshirn, "*Semiconductor Optics*" (Springer, Berlin, 1997).

[15] N. Peyghambarian, S. W. Koch, and A. Mysyriwicz, *Introduction to Semiconductor Optics* (Prentice-Hall, New Jersey, 1993).

[16] J. I. Pankove, *Optical Processes in Semiconductors* (Dover Publications, New York, 1971).

Chapter 3 Experimental procedures

The experimental detail, including the preparation of ZnO nanowires, structural and optical analysis methods are presented as follows.

1. 3.1 Growth of ZnO nanowires

3.1.1 Preparation of substrate and buffer layer

Several kinds of the substrates were used in this research, including polycrystalline Al_2O_3 (alumina), porous silicon, pre-coated ZnO thin films on silicon (111) and *c*-face sapphire.   All substrates were cleaned before the growth process of ZnO nanowires.

The porous silicon substrate was made by the electrochemical andization method on <100> p+ silicon substrates.   Electrochemical etching using Pt as the cathode was carried out for 2 mins in a Teflon cell containing HF and ethanol with 1:1 volume ratio under different current densities between 10 and 80mA/cm^2.   The resultant porous Si has a thin nanoporous layer.   Then thin gold films were deposited on the alumina and the porous silicon substrates as catalyst using sputtering deposition.

The ZnO/Si and ZnO/sapphire pre-coated films were grown by pulsed laser deposition.   A ceramic ZnO target (99.999%) was ablated in a vacuum chamber by a KrF excimer laser with wavelength of 248 nm and pulse duration of 25 ns.   A metal grid as a mask covered on part of the substrate was used to pattern the ZnO film. The deposition was done at 500°C-600°C for 2 hours under the pressure of 10^{-8} Torr and *in-situ* annealing for 1 hour at 700°C.   All samples are unintentionally doped. The thickness of the ZnO buffer film is ~ 1μm.

3.1.2 Preparation of ZnO nanowires

The ZnO nanowires were grown in a horizontal quartz tube furnace. A typical schematics of the equipment is shown in Fig. 3-1. The detail experimental parameters such as temperature, process time, pressure and flow rate etc., will be shown in each chapter. The typical growth condition is introduced in this section.

A powder mixture of pure ZnO and graphite (weight ratio 1:1) or pure Zn metal was placed in an alumina boat as the starting materials. The substrates were placed on an alumina boat and then put into the center of a quartz tube, 2.5 cm in diameter and 90 cm long, located in the middle of a high temperature cylindrical tube furnace. The zinc source was positioned in the center of the quartz tube and the substrate was placed 1cm-5cm downstream of the zinc source. After the system was evacuated to a pressure of less than 1 Torr by a mechanical pump, high-purity argon gas was introduced into the system with a flow rate of 500 sccm. Then the furnace temperature was increased to 500°C to 950°C and maintained for required time (typically 30 min) while the experiment proceeded. After the system had been cooled to the ambient temperature, a gray-white colored product was found deposited on the substrate and the wall of the tube close to the low-temperature end of the furnace.
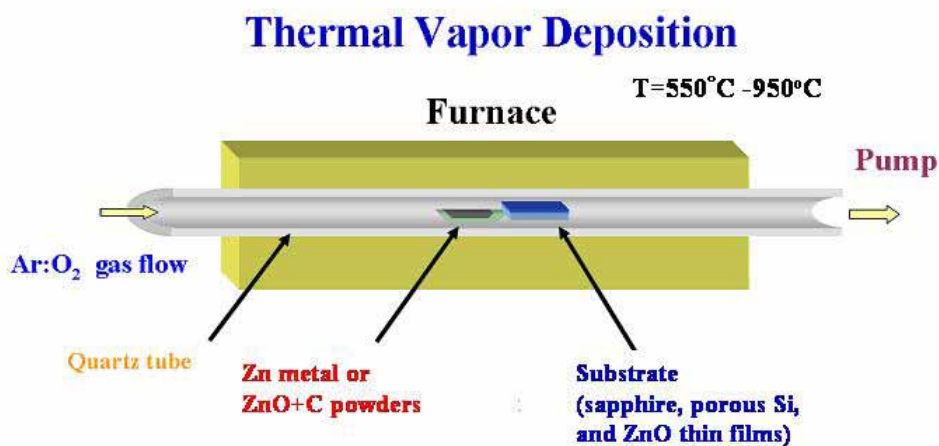
Fig. 3-1   A schematic diagram of the experimental apparatus for growth of ZnO nanowires

3.2 Structure Characterization

3.2.1 X-ray Diffraction

Structural properties were characterized using x-ray diffraction (XRD) (MAC Science MXP18) and high resolution XRD (Bede D1 system with dual channel single crystal Si monochromator). The scanning step is 0.02^o and scanning rate is 4 degree/min.

3.2.2 Electron Microscopy

The morphology and crystal structure of the products were characterized by field-emission scanning electron microscope (SEM, LEO 1530 and JEOL-6500) and transmission electron microscope (TEM, JEOL-2100).

3.2.3 Electron Beam Scattering Diffraction

The Electron Beam Scattering Diffraction (EBSD) is attached to FE-SEM JEOL-6500. The EBSD acquisition hardware comprises a sensitive CCD camera, and an image processing system for pattern averaging and background subtraction. Figure 1 is a schematic diagram showing the main components of an EBSD system. The EBSD acquisition software will control the data acquisition, solve the diffraction patterns and store the data. EBSD is carried out on a specimen, which is tilted between 60◦ and 70◦ from the horizontal. This is the best achieved by mounting the specimen so that the surface is normal to the electron beam, which is the optimum position for examining the microstructure using backscattered electrons. Following such examination the specimen may then be tilted to the EBSD operating position. If a backscattered image is required from the tilted sample, additional backscattered

electron detectors must be used [1,2] and these are typically positioned close to the transmission phosphor screen.

(a)   (b)
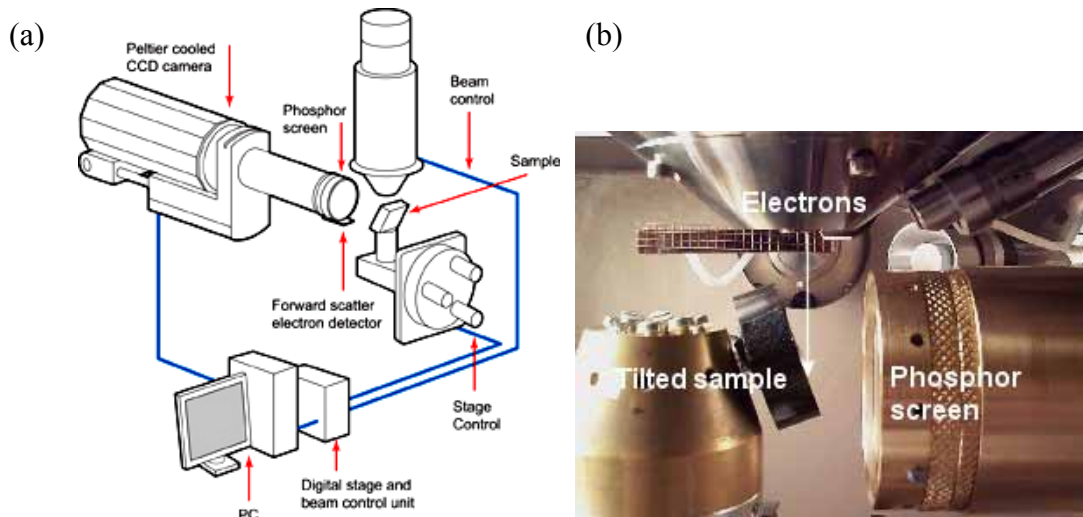
Fig.3-2 (a) Diagram of the principal components of an EBSD system.   (b) A photograph taken inside an SEM chamber showing the typical experimental arrangement for EBSD. [3]

3.2.4 Raman scattering measurement

The macro-Raman scattering was measured with an Ar-ion laser (Coherent INNOVA 90) as the excitation source emitting at a wavelength of 488 nm with 500mW.   The spectra were measured at room temperature.   As shown in Fig. 3-2, the incident beam was in 45° reflection geometry with the samples mounted on the holder to a spectrometer.   The laser beam was focused by a converging lens (f = 5 cm) in beam spot size ~ 30-50 μm in diameter) and an average power about 10 mW on the sample surface.   The scattered light was collected using backscattering geometry by a camera lens and imaged onto the entrance slit of the triplemate spectrometer (Spex 1877).
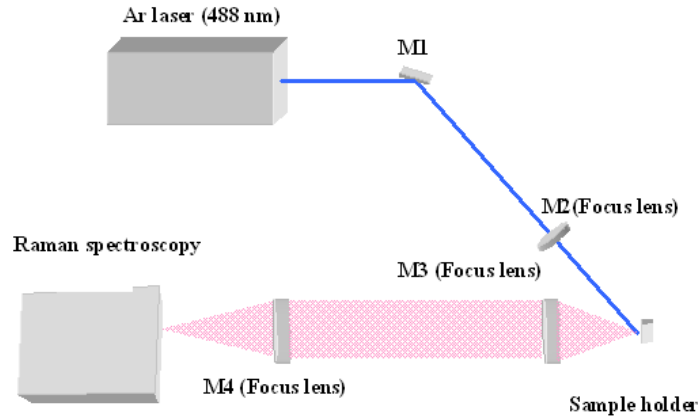
Fig. 3-3 The scheme of the Raman system.

The micro-Raman system was also preformed in the backscattering geometry with a confocal Olympus (BX-40) optical microscope. The scattered light was dispersed through the triple-monochromator system and detected by a liquid-nitrogen-cooled CCD. The 515 nm line of a frequency-doubled Yb:YAG laser was used as the Raman excitation source. The best spatial resolution during Raman measurements was 1.0 μm with a spectral resolution of 0.2 cm^{-1}.

3.3 Luminescence characterization

3.3.1 Photoluminescence

For continuous-wave (cw) photoluminescence (PL) measurement, we used a He–Cd laser (λ =325 nm) as the excitation source. For pulsed pumping, we used the third harmonic of Nd:YVO$_4$ laser (λ =355nm) with pulse width of ~500 ps and repetition rate of 1kHz. The schematics of the cw-PL and pulsed pumping system are shown in Fig 3-4(a) and (b), respectively. The excitation laser beam was directed normally and focused onto the sample surface with power being varied with an optical attenuator. The spot size on the sample is about 100μm. Spontaneous and stimulated emissions were collected by a fiber bundle and coupled into a 0.32 cm

focal-length monochromator with a 1200 lines/mm grating, then detected by either an electrically cooled charge coupled device (CCD) or a photomultiplier tube (PMT) detector. The temperature-dependent PL measurements were carried out using a closed cycle cryogenic system. The closed cycle refrigerator was used to set the temperature anywhere between 7 K and 300 K.

3.3.2 Cathodoluminescence

Cathodoluminescence (CL) studies were carried out in SEM JEOL-6500 system and a fully integrated GATAN MonoCL system equipped with scanning monochrometer. The sample was irradiated by the electron–beam at 45°C oblique incidence and emission was collected from the normal direction to the sample surface. The beam diameter in the SEM is of the order of a few nanometers. The excited volume depends on the energy of the electron beam. Electron energies ranging from 1 keV to 25 keV are commonly used in the SEM. The resulting probe areas range from tens of nanometers to a few microns in radius. The light emitted from such region is captured by a parabolic mirror, and a spectrum is obtained using a grating and a high efficiency light detector.

(a)

He-Cd laser

TRIAX 320

sample

(b)

fiber to spectrometer

third harmonic of Nd:YVO$_4$

Laser $\lambda = 355$nm

sample

knife

cylindrical len

Concave lens to
expand the beam
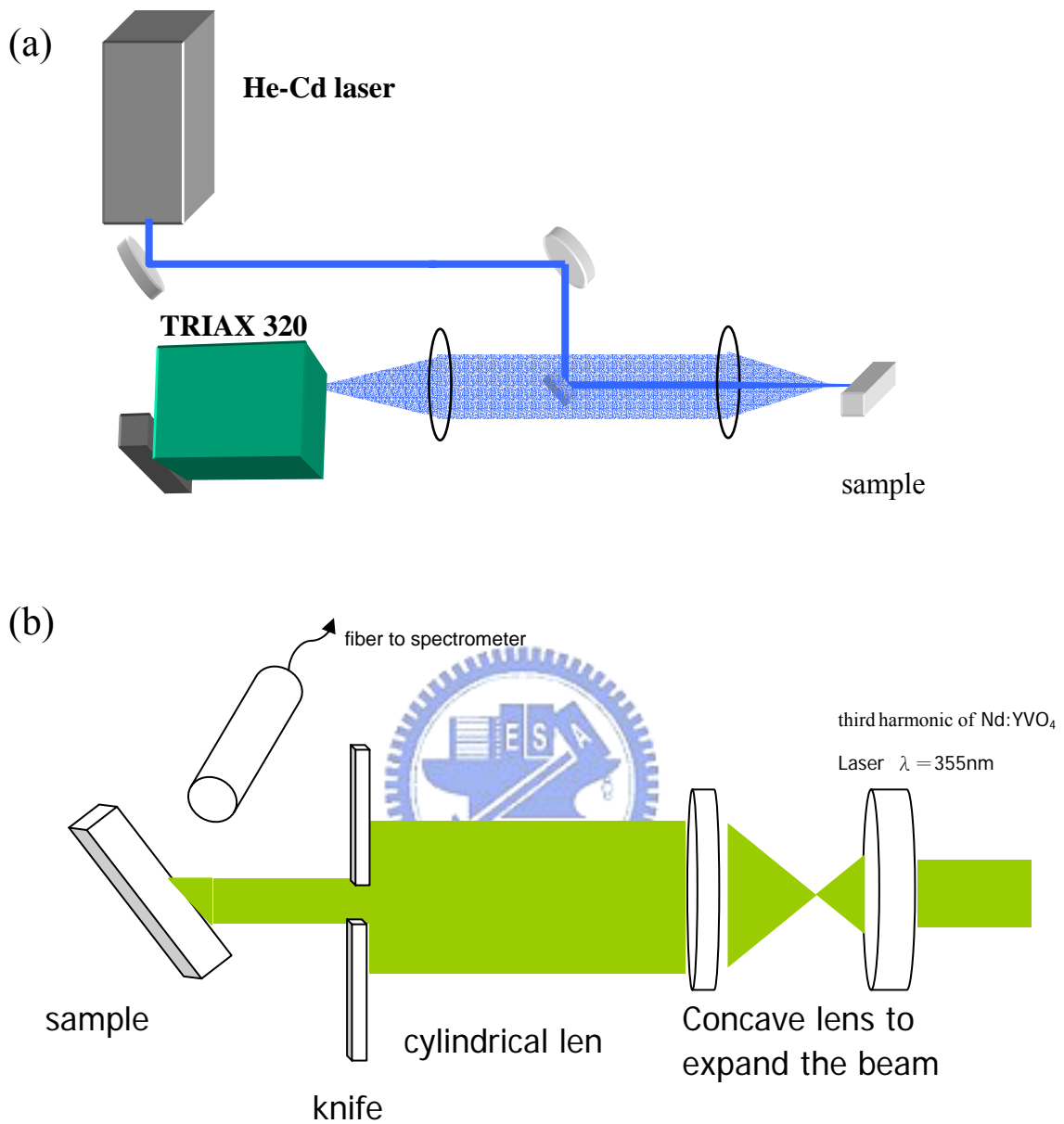
Fig. 3-4 The scheme of the PL system (a),optical pumping system (b).

References

[1]   D. J. Prior, P. W. Trimby, U. D. Weber and D. J. Dingley, *Mineral. Mag*. **60,** 859
      (1996).

[2]   A. P. Day and T. E. Quested, *J. Microscopy* **195,** 186 (1999).

[3]   http://www.ebsd.com/basicsofebsd1.htm

Chapter 4 Growth and structure properties of ZnO nanowires

4.1 Introduction

To understand the novel physical properties of ZnO nanowires and their applications in constructing nanoscale electronic and optoelectronic devices, the study focus is on how nanowire can be fabricated. Although each substrate has specific advantage for device application, the principal aim of this study is to grow vertically aligned ZnO nanowires. To step toward this aim, varies substrates, including ZnO buffer layers, Au coated-porous silicon, sapphire (0001) and so on, were used for the fabrication of ZnO nanowires. The growth and structure properties of ZnO nanowires are discussed. Moreover, controlling the growth area, growth direction, epitaxial relation between nanowires and substrates are also investigated.

4.2   Selective growth of ZnO nanowires via self-catalyst method

Figure 4-1 displays the atomic force microscope tomography of a ZnO buffer layer with the oxygen pressure of 10^{-2} Torr. It is seen that the film surface was non-uniform with root mean square (RMS) roughness of 1.3 nm. Presented in Fig. 4-2 is the SEM photograph of the nanowires grown on ZnO buffer layer with the oxygen pressure of 10^{-2} Torr. High yield of the nanorods were observed on ZnO buffer layer (left hand side of the figure) but rare nanorods were observed on the other part of the sapphire substrate, where was covered by the metal mask during the growth of ZnO buffer layer. The SEM-photograph shown in Figure 4-3(a) is a magnified section of high yield ZnO nanowires, as can be seen, the nanowires are

well-defined hexagonal crystals with diameters of around 100-300 nm and lengths up to 3µm. Figure 4-3(b) shows the Energy-Dispersive X-ray (EDX) spectrum of this section, which indicates that the nanowires contain only Zn and O elements and notably no other elements are detected.
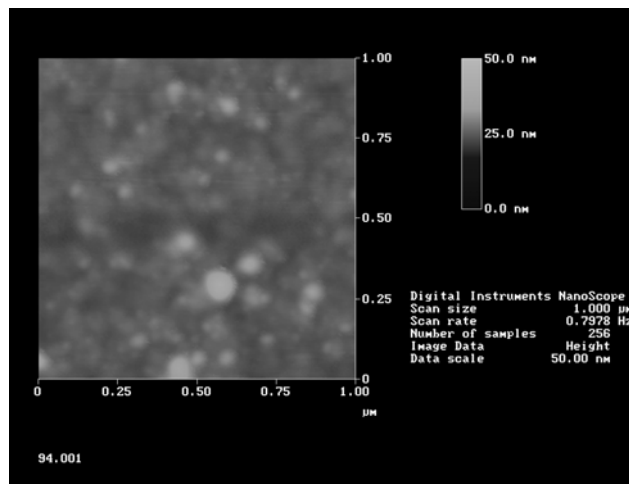
Fig. 4-1 The AFM image showing the morphologies of ZnO buffer layer grown on a sapphire (0001) substrate.
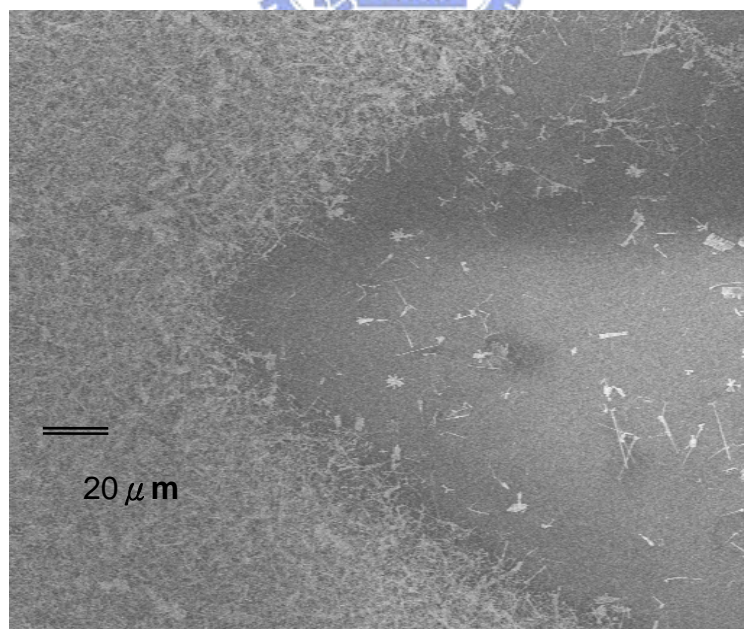
Fig. 4-2 SEM image of the ZnO nanorods showing two different growth regions.

The formation of ZnO nanowires includes two steps: nucleation and growth. For the conventional VLS process, metal catalyst such as gold is necessary to form the liquid metal-alloy droplets and the nanowires are grown through condensation of the source metal from the supersaturated liquid metal-alloy droplets followed by immediate oxidation. Since there are no metal catalysts involved in the growth process, no droplets were found at the ends of nanorods, which is the main feature of the VLS mechanism, the growth mechanism is not based on VLS but it is likely governed by vapor-solid process [1] or the so-called self-catalyzed VLS process.[2] As shown in AFM tomography in Fig. 1, the presence of pits or hills with nanometer order on the surface of ZnO buffer layer may provide nuclear seeds for the thermally vaporized Zn atoms to condense onto the substrate, which is similar to the growth of MgO nanorods.[3]   Thus, the already condensed Zn not only acts as the seed but also provides an energetically favorite site for adsorption of oxygen.
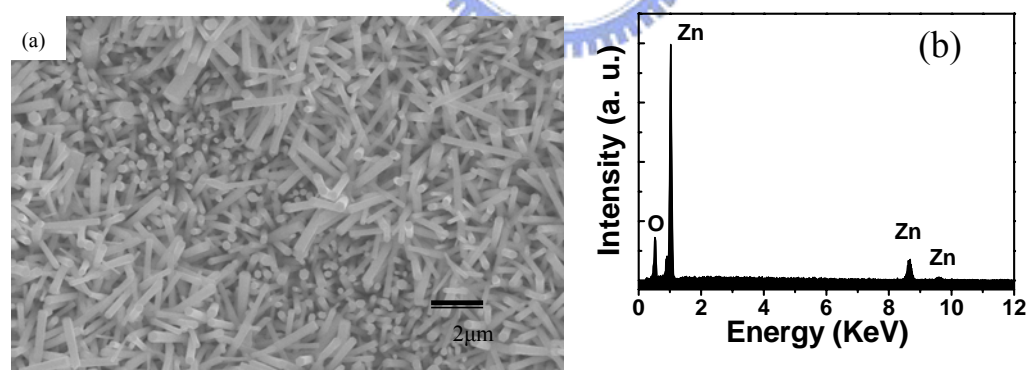
Fig. 4-3 (a) A typical high magnification SEM image shows shapes of ZnO nanowires. (b) EDX pattern of the ZnO nanorods.

It has been demonstrated that the morphology of the crystals is related to the relative growth rates of various crystal faces that bound the crystal; these growth rates

are not only determined by the internal structure of the crystal but also affected by the growth conditions.[4]   The SEM image in Fig. 4-3(a) indicates that the growth rates of the directions <001>, <101>, and <100> of the ZnO crystal have the relationship of $R_{<001>} > R_{<101>} > R_{<100>}$.   The anisotropic growth of the crystal causes formation of high aspect-ratio ZnO nanostructure and the ZnO nanowires are preferentially oriented along the c-axis with prismatic morphology on their tops.

On the other hand, there are only very few nanowires on the bare sapphire. This is due to the smooth surface may not serve as a nucleation site, Zn vapor is hardly condensed on the clear sapphire surface as compared with on the rough ZnO buffer layer.   This result is consistent with the previous report on ZnO nanorods growth by MOVPE method [5] that a thin ZnO buffer grown at low temperature is a key factor for their growth method.   Hence, according to the VS axial growth mechanism, pre-coated ZnO buffer layer is preferential to grow ZnO nanowires. Figure 4-4 displays an assembly of ZnO nano-homojunctions formed on several nanorods on the different morphology of buffer layer.   If the surface of the nanorods is rough and the concentration of Zn reaches the critical vapor pressure, then the nano-branches will grow from the nano-valley on the surface of the nanorods.   This growth mechanism of ZnO branch may be similar to the growth of self-catalyzed nanowires and is analogous to Jian's finding on SnO_2 nanodendrites. [6]   They found the morphologies of the SnO2 nanowires change under different oxygen gas flow. Unfortunately, we are still not able to completely control the growth conditions to obtain   the   desired   types   of   ZnO   branches.
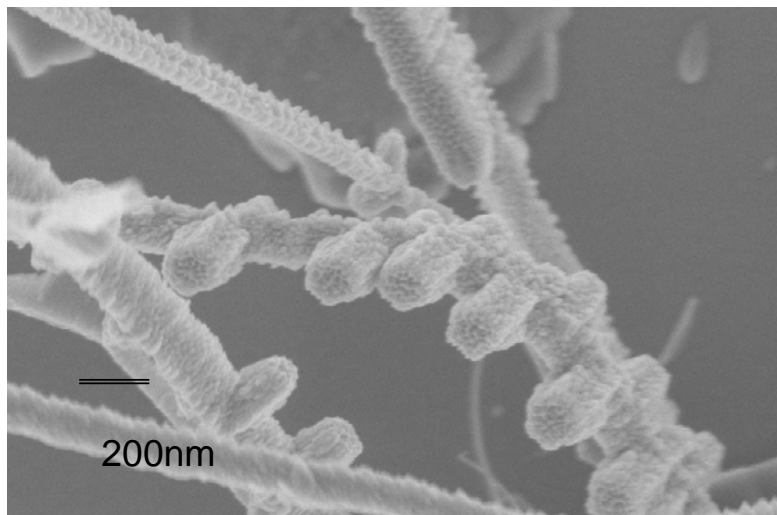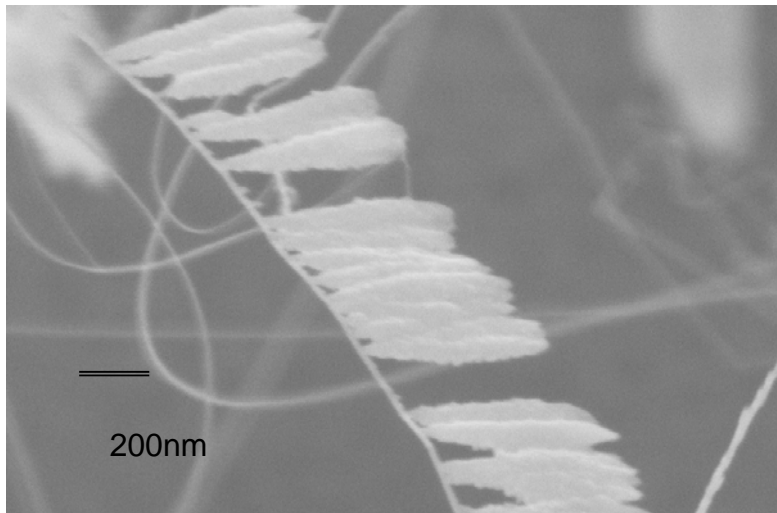
Fig. 4-4 3D ZnO structures with several nanowires.

4.3   ZnO nanowires grown on porous silicon substrate

ZnO nanowires grown on Si-based substrates have received increasing interest for their low cost and large size.   The next-generation semiconductor nanowire-based nanophotonic devices with the well-developed Si-based technology will have many potential applications.   Unfortunately, the large mismatches in the thermal expansion coefficients and the lattice constants would introduce a rather large stress between the ZnO and the Si substrate.   This stress results in the growth of randomly oriented ZnO nanowires.   Many efforts to prepare ZnO nanowires on a Si

substrate have not attained a satisfactory quality due to the large stress. Recently, Fan et *al.* [7] reported self-oriented regular arrays of carbon nanotubes by using a porous silicon substrate. Additionally, porous silicon (PS) can emit red to blue emission with rather easily obtainable red emitting in PS. [8,9] A white light source is achievable if the red emission from the PS layers can be combined with the green emission from the defect band of the ZnO and the blue-UV emission from the ZnO excitonic emission.

A typical cross-section-view SEM image of the high-density ZnO nanowires grown on a large area of the substrate is shown in Fig. 4-5. The majority of the nanowires are grown with a length of about 2-3 μm and diameters ranging from 20–200 nm. This micrograph reveals a high density of quasi-aligned nanowires uniformly distributed over the entire substrate. A TEM image (see Fig. 4-6) shows that the diameter of an individual ZnO nanowire is about 30 nm. The inset in Fig. 4-6 shows a typically selected area electron diffraction (SAED) pattern for a single ZnO nanowire. Along the same nanowire, the diffraction patterns are essentially identical, revealing that the nanowire is hexagonal wurtzite single-crystalline ZnO. The absence of even one droplet on the tip of a ZnO nanowire seems to imply that the growth mechanism is not followed by the VLS mechanism. This observation is due to the Au being infiltrated into the PS pores as the growth temperature is increased. The adhesive force between Au and PS was stronger than that between Au and plain Si. Therefore, Au as a catalyst stayed at the bottom of the nanowires when Zn vapor was introduced into the catalytic system. The above growth is still likely to be governed by the VLS mechanisms.
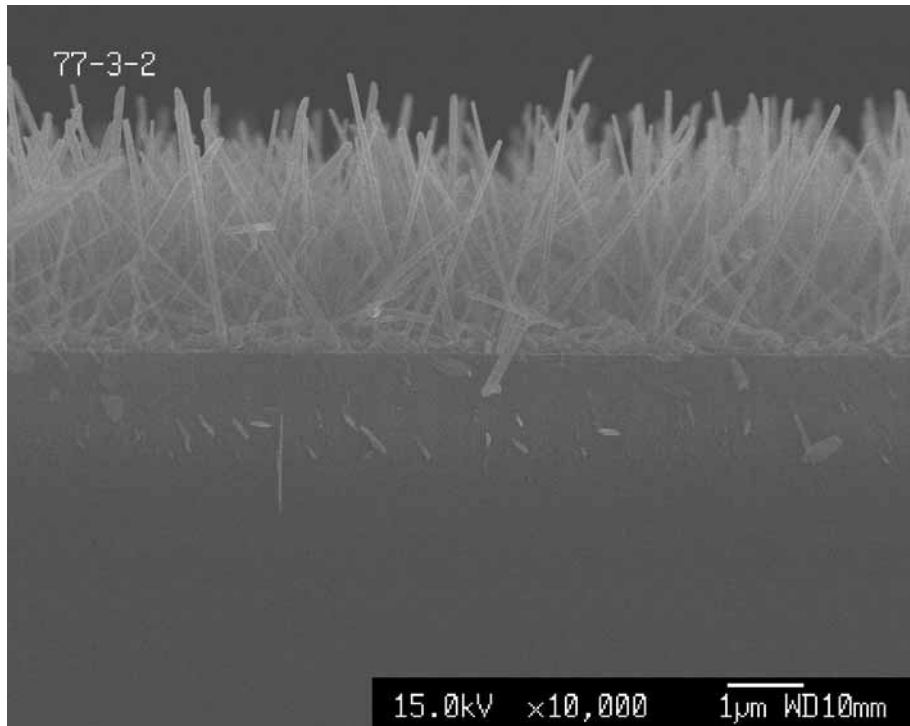
Fig. 4-5 SEM cross-section-view image of the ZnO nanowires on PS.
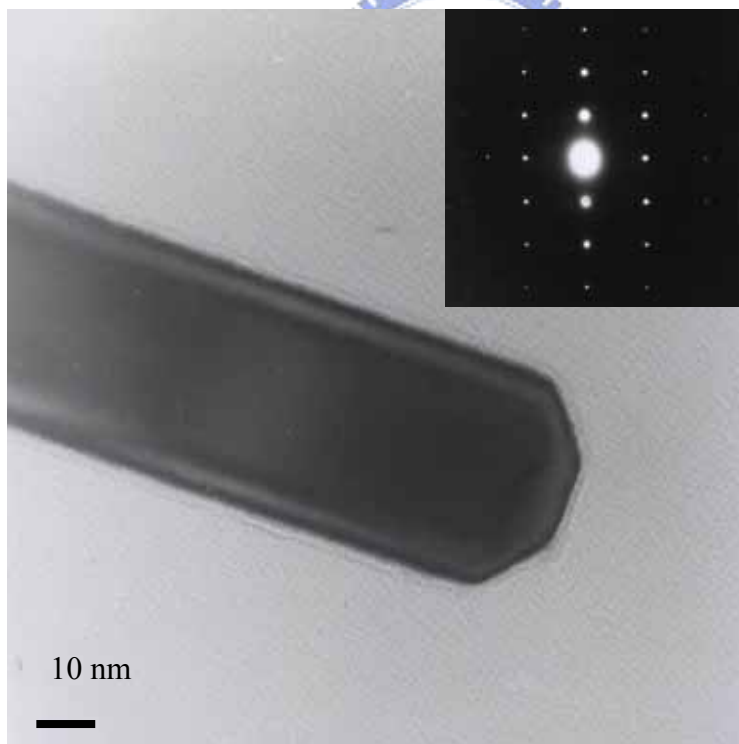
Fig. 4-6 TEM image showing the representative morphology of the ZnO nanowires. Inset shows the SAED patterns, revealing the monocrystalline phase nature of the nanowires.

Figure 4-7(a) displays a typical XRD pattern for the ZnO nanowire. Major peaks were identified and compared with JCPDS file 36-1451, drawn at the bottom of Figure. 4-7(a). This reveals that the product is composed of hexagonal ZnO with lattice constants a=0.325 nm and c=0.522 nm, which is in agreement with the JCPDS card for ZnO. These data from XRD and SAED analysis altogether further reveal that the ZnO nanowires are hexagonal wurtzite crystalline ZnO.

(a)

(b)
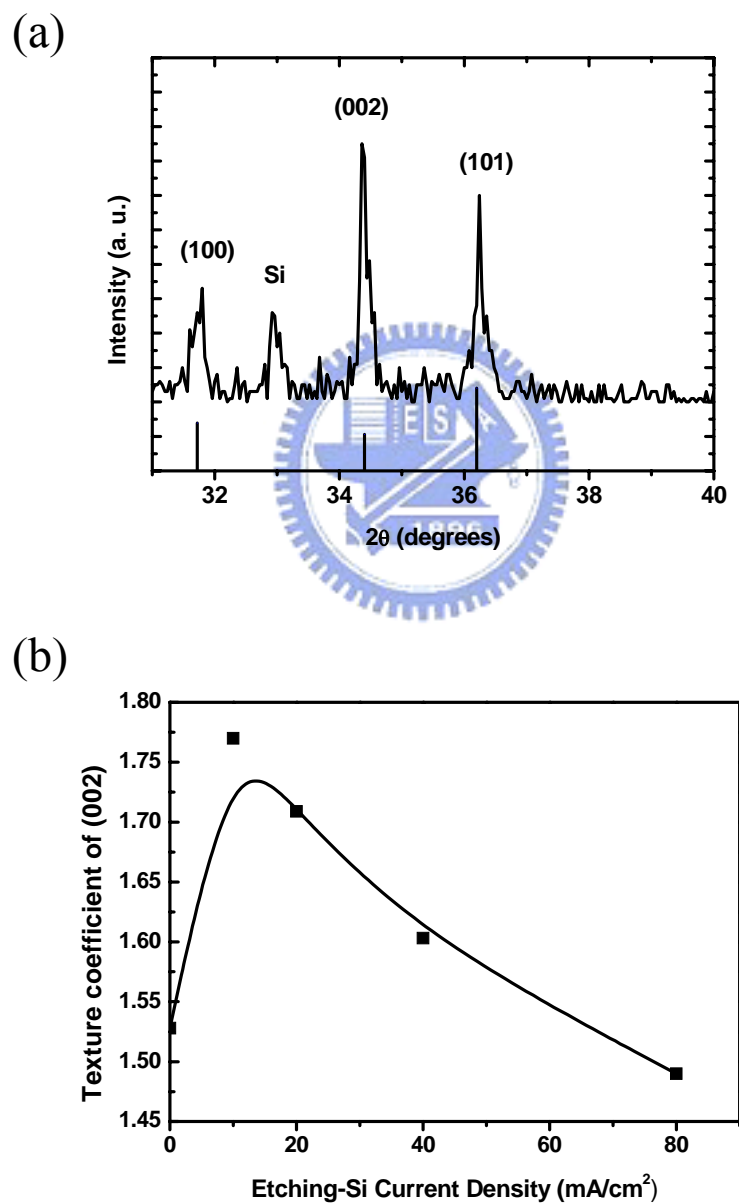
Fig. 4-7 (a) Typical XRD spectra of the ZnO nanowires. (b) Texture coefficient of the ZnO nanowires as a function of the Etching-Si current density.

Furthermore, we used the texture coefficient (TC) [10] to determine the orientation of the ZnO nanowires. Normally, the growth direction of ZnO nanowires is [002].[11] The texture coefficient can be expressed as the following expression:

$$TC_{(hkl)} = \frac{I_{(hkl)}/I_{0(hkl)}}{\frac{1}{N}\sum_{N}(I_{(hkl)}/I_{0(hkl)})} \quad , \qquad\qquad 4.1$$

where $I_{(hkl)}$ is the observed intensity of the (hkl) plane, $I_{0(hkl)}$ is the standard data (JCPDS 36-1451) of the (hkl) plane, and N is the total number of diffraction peaks. When the TC value is larger than 1, a preferred orientation exists in the sample. We calculated three stronger diffraction peaks for ZnO nanowires, which are (100), (002) and (101). Figure 4-7(b) shows the TC of (002) plane as a function of the current density of the etched silicon. Notably, the porosity increases with the etching current density for a specific HF concentration.[12] One can find that all of the TC values of (002) plane are larger than 1, indicating the preferred orientation of the ZnO nanowires. The TC value (1.48-1.77) of ZnO nanowires grown on PS is larger than that of most other ZnO nanowires grown on silicon substrates [13-15], which are calculated and listed in Table 4-1. The TC value of the ZnO nanowires grown on (110) sapphire [11], which is lattice matched with ZnO, is also listed in Table 4.1 as a reference. The calculated TCs with different porosities of the porous silicon made by different current densities reveal that the porous silicon would benefit the growth orientation of ZnO nanowires. The possible reason for this is that the small current density makes the morphology of the silicon surface appear to have a <111> direction and helps ZnO nanowires grow in the <002> direction. With increasing current density, the morphology of porous silicon results in randomly directed growth of the ZnO nanowires making the TC decrease.

Table 4-1

The calculated (002) texture coefficient value with pervious works and this work.

TC value	substrate	refence
1.05	(100) Si	Ref [9]
1.41	(100) Si	Ref [10]
0.99	(100) Si	Ref [17]
~3	(110) sapphire	Ref [3]
1.48-1.77	porous Si	This work

To investigate the influence of the current density of the Si-etching on the diameter of nanowires, the diameters of the ZnO nanowires in all of the samples were carefully estimated from the SEM images. Figure 4-8 plots the histograms of the diameter distribution for ZnO nanowires grown on various substrates etched at different current densities. A Gaussian curve fitting to each of these histograms as solid curves yields a mean diameter of 83.5nm, 89.0nm, 72.4nm and 60.0nm for Si-etching under current densities of 10mA/cm^2, 20mA/cm^2, 40mA/cm^2 and 80mA/cm^2, respectively. Among these etching conditions, ZnO nanowires have the smallest mean size and the narrowest distribution on porous Si for the etching density of 80mA/cm^2. This observation results from the monodispersity of the catalyst clusters on PS under the large etching current density. We have also grown the ZnO nanowires on Au-coated plain Si (100) substrate as a reference. The overall structures of the nanowires are similar to those grown on porous silicon. However, we found that the nanowires synthesized on plain silicon substrates have an even broader diameter distribution than those on PS substrates. Also, the nanowires appear to be less well aligned (lower TC ~1.53) on plain silicon substrates than on the PS ones. Hence, we believe that these PS substrates would play an important role in controlling the orientated growth and narrowing the diameter distribution of ZnO

nanowires.
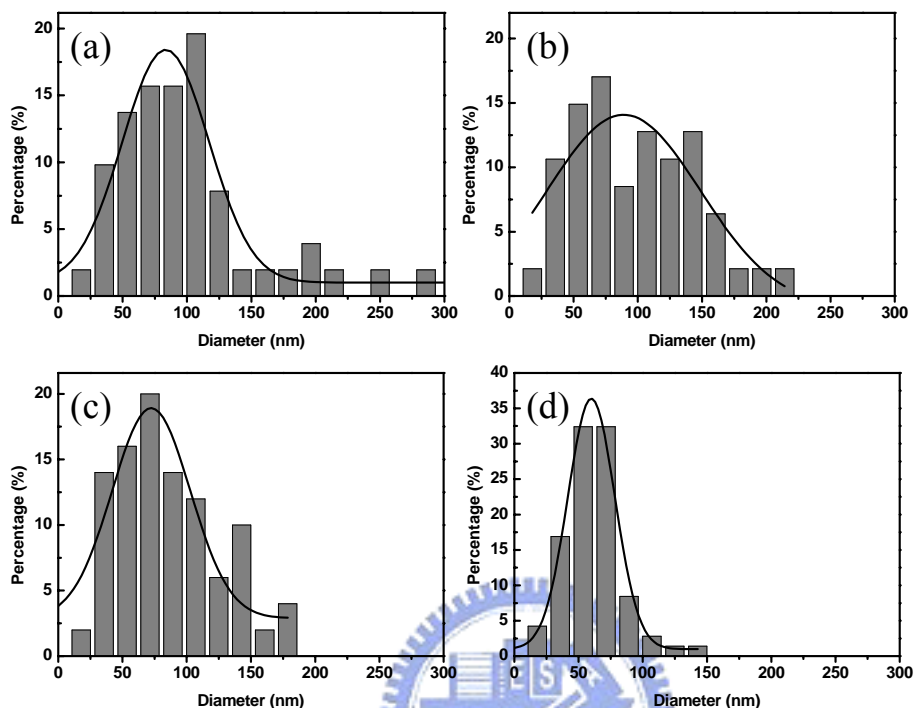
Fig. 4-8 Histogram of the diameter of ZnO nanowires grown on porous Si for different etching current densities: (a) 10 mA/cm^2 (b) 20 mA/cm^2; (c) 40 mA/cm^2, (d) 80 mA/cm^2.

A typical Raman spectrum for ZnO nanowires grown on a silicon substrate is shown in Figure. 4-9.   The observed phonon frequencies are A$_1$(TO) ~380 cm^{-1} and E$_2$(high) ~ 436 cm^{-1}.   Since the penetration depth of the Argon laser is longer than the length of the ZnO nanowires, a pronounced phonon mode of the Si substrate at 520 cm^{-1} was also observed.   The E$_1$(LO) is associated with a lattice defect, such as oxygen vacancies and zinc interstitial in the ZnO nanowires, which is similar to the previous results. [16]   Clearly, this result with very weak E$_1$(LO) indicates that the sample is composed of ZnO with high quality hexagonal nanowires.
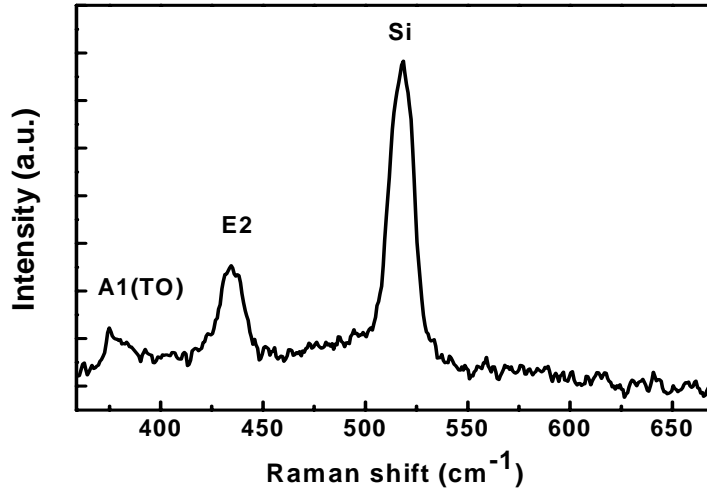
Fig. 4-9 Typical Raman spectra of the ZnO nanowires on PS substrate.

4.4 Well-aligned ZnO nanowires on ZnO thin film

From the finding of the first section of the chapter, ZnO nanocrystal can be served as a seed. Here, we report the ZnO nanowires grew on the high quality ZnO thin films and investigate the in-plane orientation of nanowires.

Figure 4-10(a) and (b) show typical plane and oblique-view SEM photographs of the ZnO nanowires fabricated on ZnO/Si(111) and ZnO/sapphire(0001) substrates, respectively. All ZnO nanowires are well vertical aligned normal to the surface. The diameter of ZnO nanorods can vary between 70 to 200 nm depending on processing parameters and the lengths can be as long as 1.5 μm.
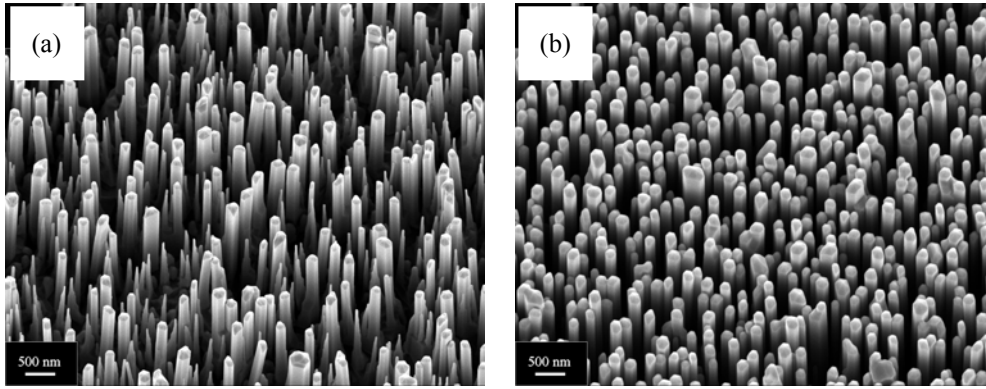
Fig. 4-10 The typical oblique-view SEM photographs of the ZnO nanowires fabricated on (a) ZnO/Si(111) and (b) ZnO/sapphire (0001) substrates.

Figure 4-11 shows the θ-2θ x-ray diffraction patterns. Only the {0001} reflection family of ZnO and surface paralleled plane of substrate appear in the wide angle XRD profile, indicating all the ZnO films have a ZnO single phase as well as a complete c-axis preferential growth. Meanwhile, the FWHM of the corresponding ZnO(0002) θ-rocking curve was 0.73° and 0.056°. The broad mosaic distribution causes some ZnO nanowires grown slightly along the inclined angle, due to the mosaic grains behave as the nucleus for growth of ZnO nanowires. It means that the buffer layer on the sapphire substrates was almost perfectly grown along the c-axial direction. Therefore, the ZnO nanorods reflect more vertically aligned on ZnO/sapphire(0001) being comparable to ZnO/Si(111).
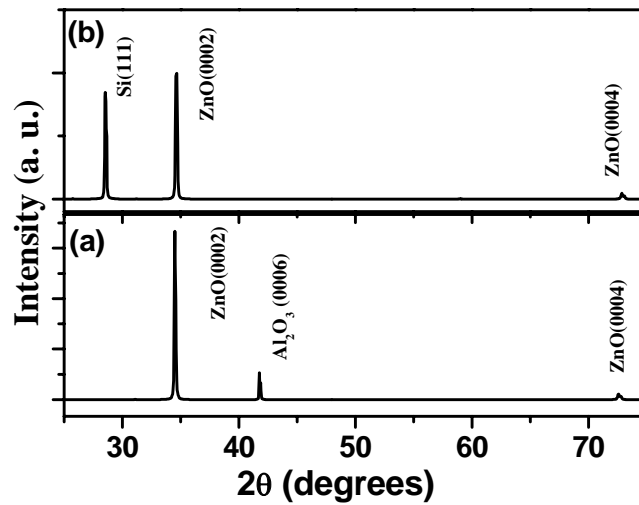
Fig. 4-11 The XRD patterns of the ZnO nanowires grown on (a) sapphire(0001) and (b) Si(111).

The vertically nanowires aligned on the both substrates. The relationship of in-plane orientation can be discovered from plane-view SEM photographs by the fast Fourier transform (FFT), as shown in the insets. The FFT of Fig. 4-12(a) displays the blurred spots indicating that the ZnO nanowires on ZnO/Si(111) are randomly oriented in the in-plane direction. On the contrary, the vertically aligned ZnO nanorods on ZnO/saphire(0001) show an in-plane alignment with six-fold symmetry confirmed from the hexagonal star-like spots, as shown in the insets in Fig. 4-12(b).
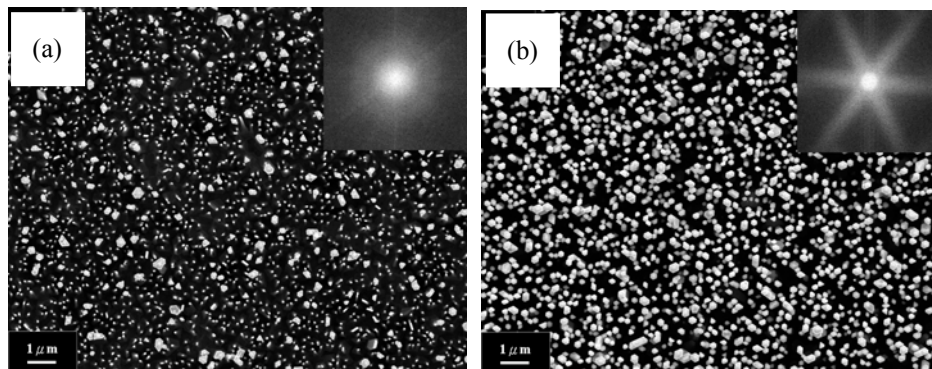
Fig. 4-12 The typical plan view SEM photographs of the ZnO nanowires grown on (a) ZnO/Si(111) and (b) ZnO/sapphire (0001) substrates. The Inset shows their corresponding FFT images.

The EBSD also provides crystallographic information of the micro-structures. Figure 4-13 shows the EBSD patterns of two different position from the ZnO nanowires on the ZnO/Si(111) substrate. The EBSD patterns constitute a number of Kikuchi lines but are not identical. To specify an orientation, it is necessary to define a reference frame consisting of at least two axes, which is known as a coordinate system. Important surfaces or directions associated with the shape of the specimen are commonly used to define the axes. The direction normal to the specimen surface is called 'normal surface', in-plane directions are the 'rolling direction' and 'transverse direction'. Figure 4-14 shows the inverse pole figures.

In the normal surface direction, a discrete peak was observed as a result of the vertically aligned of the nanowires. However, both in the rolling and transverse directions, a continuous curve appeared. It indicates that the in-plane orientation of nanowires is disordered.
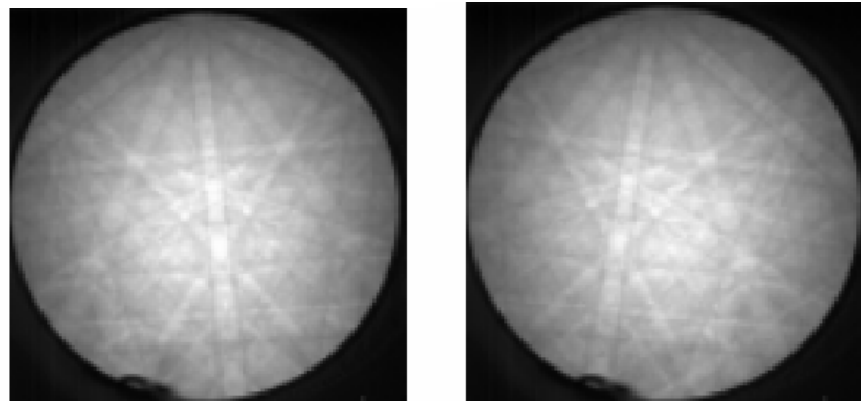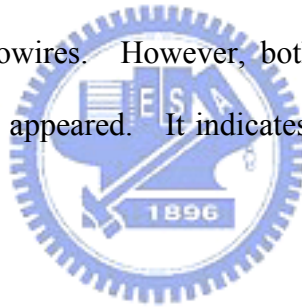
Fig. 4-13 The EBSD image taken from two different position of the ZnO nanowires on the ZnO/Si(111) substrate.
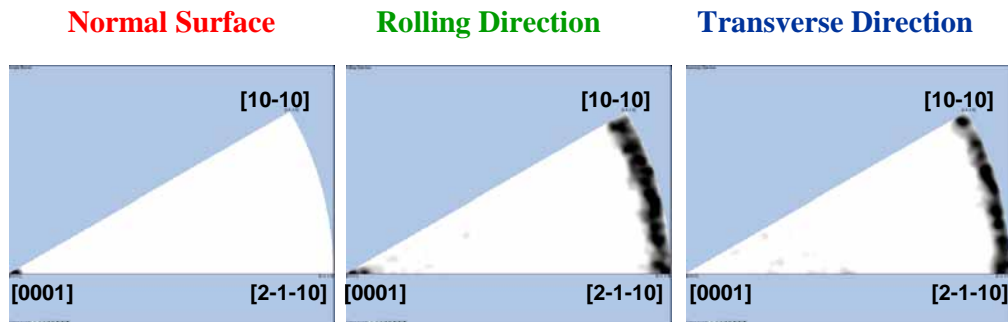
Fig. 4-14 The inverse pole figures of the ZnO nanowires on the ZnO/Si(111) substrate for the three orthogonal directions.

On the contrary, the EBSD patterns of two different positions from the ZnO nanowires on the ZnO/sapphire(0001) substrate are identical as shown in Fig. 4-15. The inverse pole figure maps is shown in Fig. 4-16.   A discrete peak was observed both at the rolling and transverse directions.   It clearly indicates that the nanowires with not only the out of plane order but also in-plane order.
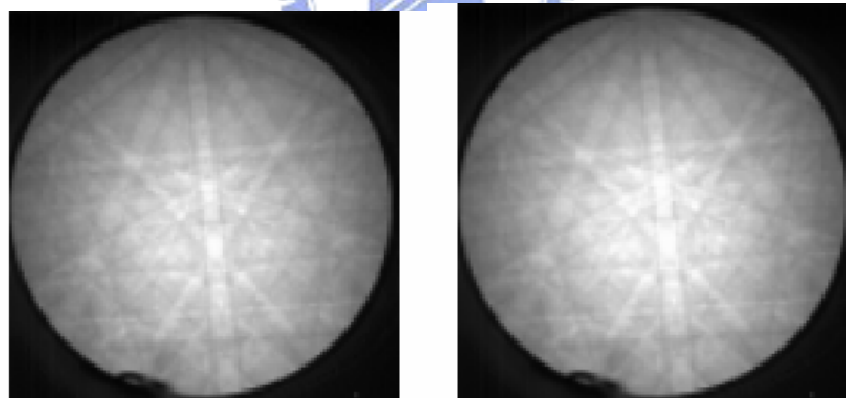
Fig. 4-15 The EBSD image taken from two different positions of the ZnO nanowires on the ZnO/sapphire (0001) substrate.

Normal Surface **Rolling Direction** **Transverse Direction**
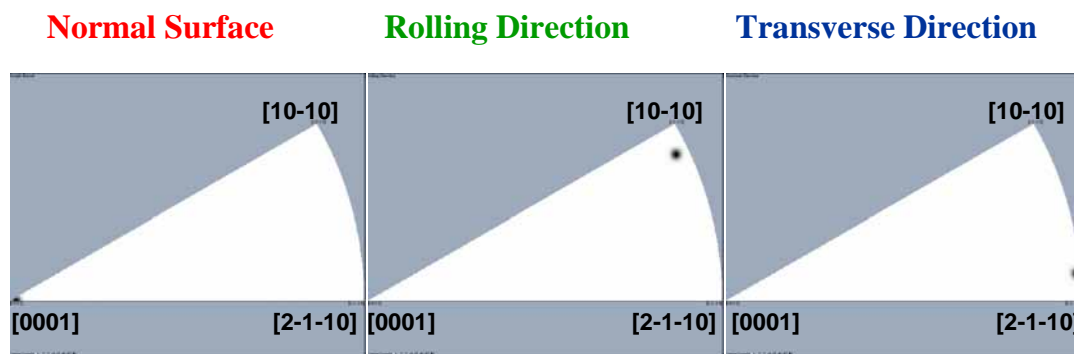
Fig. 4-16 The inverse pole figures of the ZnO nanowires on the ZnO/sapphire (0001) substrate for the three orthogonal directions.

It is believed that the difference of relationship of in-plane orientation results from the orientation of the precoated ZnO buffer layers. To explaining the in-plane growth relationship of ZnO nanorods, the XRD Φ-scan analysis was used to investigate the ZnO buffer layers on different substrates. Figure 4-17(a) demonstrates that the ZnO/Si(111) have random alignment along the in-plane direction. The reasons are explained in terms of amorphous phase for glass and the possible formation of an amorphous silica layer between ZnO and Si substrate. Although the lattice mismatch between ZnO and Si(111) is ~3.5%, but the difficulty basically stems from the fact that Si surface gets easily oxidized during the nucleation stage of a ZnO growth process.[17] In contrast, the ZnO buffer layers on saphire(0001) exhibit an in-plane alignment with six-fold azimuthal symmetry, as shown in Fig. 4-17(b). For sapphire substrate the epitaxial relationship would be $[0001]_{ZnO}$ // $[0001]_{\alpha-Al2O3}$ and $[10\bar{1}0]_{ZnO}$ // $[11\bar{2}0]_{\alpha-Al2O3}$. This result also consist with the FFT of top-view SEM image as shown the sharp star-like spots when ZnO nanowires grown on sapphire (0001) and the EBSD observation. Consequently, we conclude the excellent normal and in-plane alignment for ZnO/sapphire(0001), therefore improving the growth of ZnO nanowires.
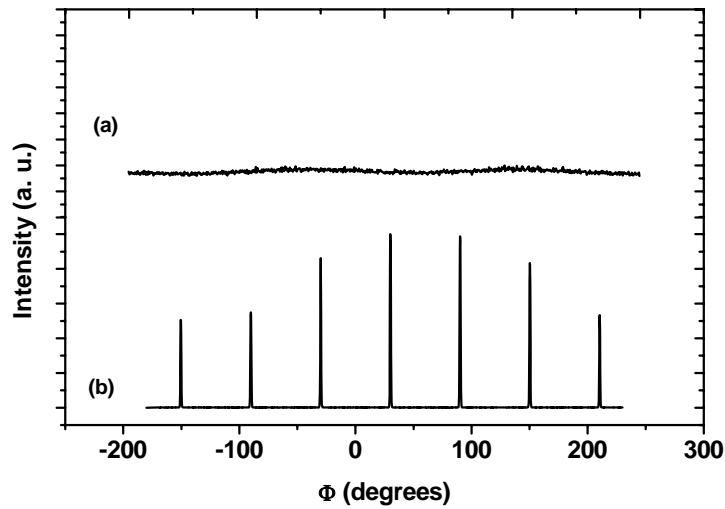
Fig. 4-17 The XRD Φ scan of ZnO thin films on (a) sapphire (0001) and (b) Si(111).

4.5 Epitaxial relation between nanowires and substrates

Figure 4-18 shows the low-magnification SEM images of the ZnO nanostructure. High yield nanostructure grew over the substrate. Figure 4-19(a) shows the high-magnification image with 15° inclination of the region of the pre-coated ZnO epilayer. Vertically aligned nanowires have diameters ranging from 80 to 350 nm. The cross section of each wire was well-faced hexagon. The epitaxial relationship is $[0001]_{ZnO\ wire}//[0001]_{ZnO\ film}$ and $[11-20]_{ZnO\ wire}//[11-20]_{ZnO\ film}$.
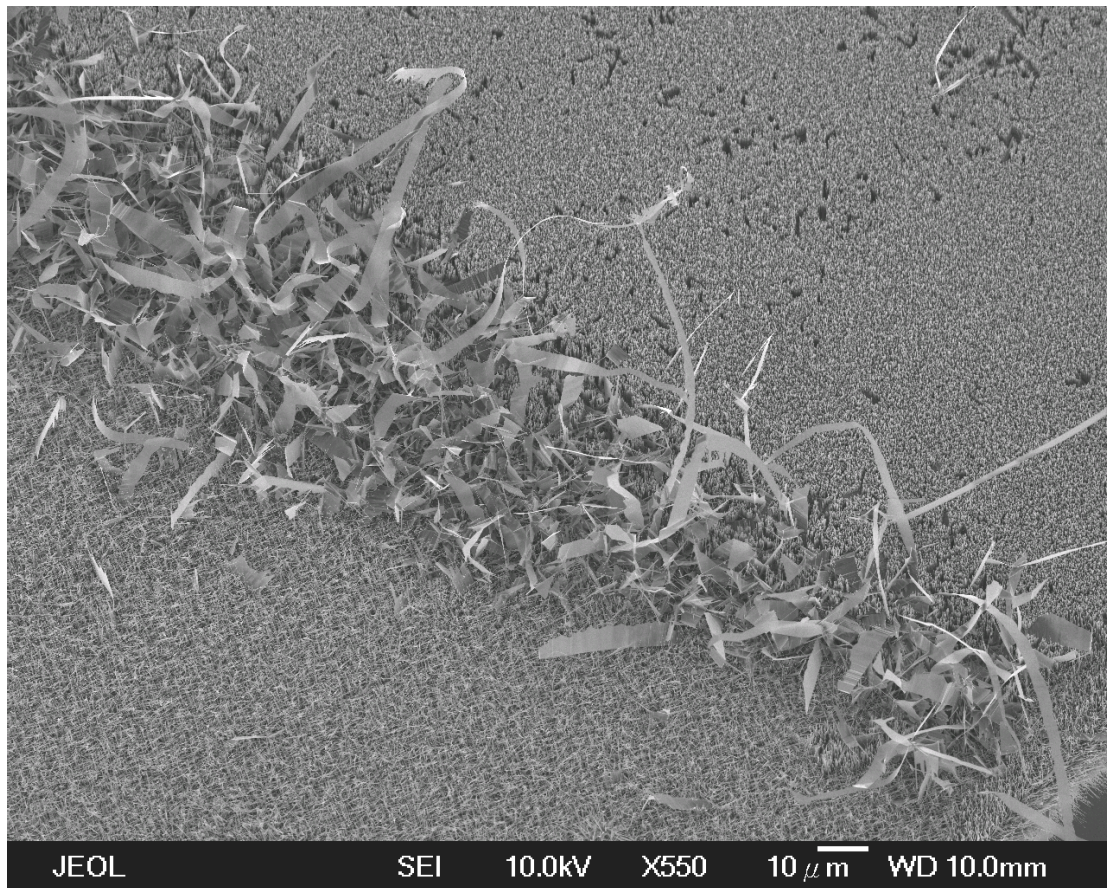
Fig. 4-18 Low-magnification SEM images of the synthesized ZnO nanostructure.

A top-view image of the nanowires grown on the region of bare *c*-plane sapphire is shown in Fig. 4-19(b). There are three clearly noticeable orientations with in-plane components parallel to the sides of an equilateral triangle. Some wires are oriented perpendicular to the surface, they appear just as small bright spots from the top view. A hillock was noted at the base of these nanowires. A noticeable feature of hexagonal hillocks is a typical phenomenon in the epitaxial growth of nanowires.[18] The hillocks form in an early stage and serve as nucleation sites for subsequent growth of vertical nanowires.
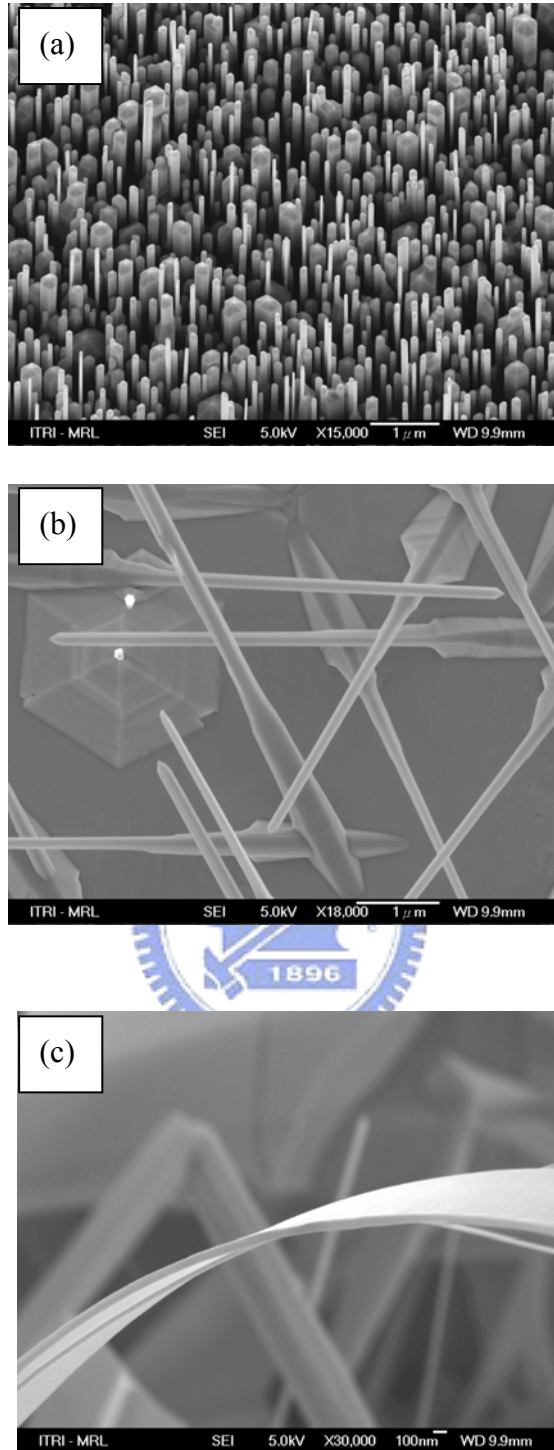
Fig. 4-19 High-magnification SEM images of the synthesized ZnO nanostructure on the ZnO epilayer (a), *c*-plane sapphire (b), junction bwteeen the epilayer and sapphire (c).

It is noted that the crystal surface of the pyramid island has a 30° rotation of the ZnO unit cell respect to that of sapphire. This phenomenon is due to reduce the

lattice mismatch between ZnO and sapphire from 32% to 18%, similar to the growth of the ZnO epilayer on *c*-plane sapphire substrate.[19]   The in-plane epitaxial relationship between ZnO island and sapphire should be ZnO(10-10) //sapphire(11-20).   Baxter *et al.* analyzed the epitaxial relation of nanowires on *c*-plane sapphire.[20]   The nanowires grow at an angle of 51.8° with ZnO[0001]// sapphire [10,14] as a result of the excellent lattice symmetry and lattice match (~2.3%).   Combining with the 3-fold rotational symmetry of the *c* -plane sapphire, these epitaxial relationships lead to nanowires growing on *c* –plane sapphire in one of three directions separated in projection by 120°.

In addition, the nanobelts/nanosheets grown at the junctions between the epifilm and the c-plane sapphire are shown in Fig. 4-19(c).   The width, thickness, and length of the belts are in the ranges of 50-100 nm and 3-6 nm, and 5-40 μm, respectively. Unlike the nanowires whose growth and alignment were strongly related to the ZnO buffered layer and sapphire.
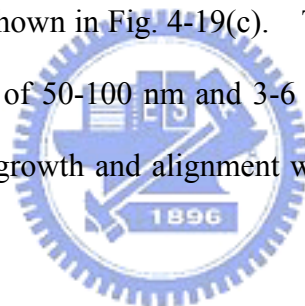
The growth mechanism of ZnO nanowires is likely governed by vapor-solid process.[21]   According to the growth of ZnO thin film, under zinc-rich ambient, thin film will prefer to column growth.[22]   Under this growth condition, the growth rate of the plane [001] is higher than the others.   In our processing furnace, no extra O_2 was added, hence the anisotropic growth of the ZnO crystal nanowires occurred. Nevertheless, the formation of the nanobelts is an issue.   We believe that it is related to the airflow condition at the step of ZnO thin film or the crystal face of the step wall of ZnO thin film.   The supersaturation of the Zn vapor occurs at the step position, leading to an enlargement of the crystal dimensions.

Figure 4-20 shows typical micro-Raman spectra of the ZnO nanostructures.

The wurtzite structure of ZnO belongs to the space group $C_{6\upsilon}^{4}$ (P6$_3$mc) with two

formula units in a primitive cell.[23-24]   The group theory predicts the existence of

the following optic modes: A$_1$ + 2B$_1$ + E$_1$ + 2E$_2$ at the Γ point of the Brillouin zone;

B_1(low) and B_1(high) modes are normally silent; A_1 , E_1, and E_2 modes are Raman

active; and A_1 and E_1 are also infrared active.   To analyze the Raman mode of ZnO

materials on sapphire substrate has to be quite careful because there are several peaks

overlapped with each other.[25]   For example, the E1(TO) mode of ZnO overlap

with the Eg mode of sapphire at 378cm^{-1}; A1(LO) mode of ZnO with another Eg

mode of sapphire appears near 578 cm^{-1}.   In spite of these two features in Raman

spectra, we still observed the E$_2$ (high) mode at 437 cm^{-1} with their width of 10 cm^{-1}

indicating good crystal quality, we also observed E1(LO) mode near 586 cm^{-1} for the

vertical aligned nanowires.   This is because the propagation direction of E1(LO)

parallel to [0-11] is parallel neither to the XY-plane nor to the Z-axis.[26]   In the

backscattering configuration, this vibration mode of the tilted nanowires and

random-orientation nanobelts is more efficiently collected than that of the vertically

nanowires so as the Raman spectrum of these ZnO nanostructures strongly depends

on the collected configuration and crystal face.
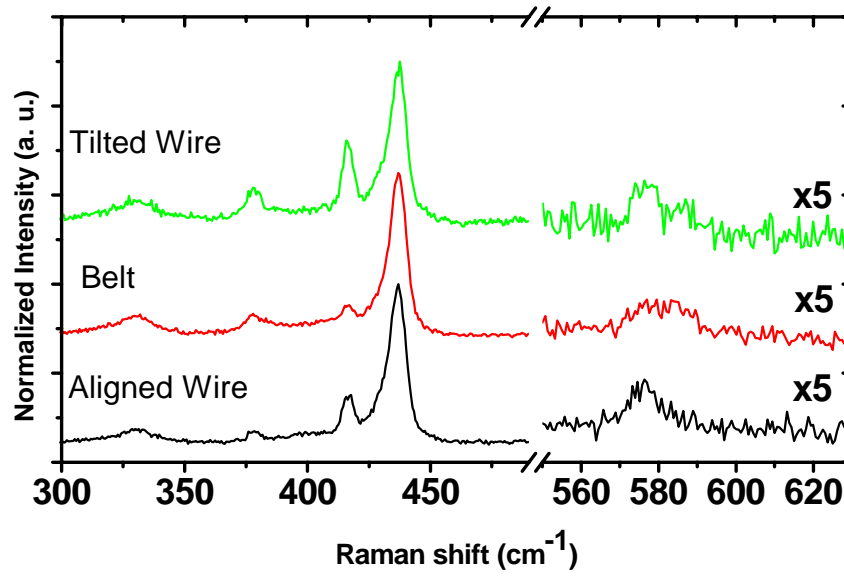
Fig. 4-20 Raman spectra obtained from (a) the vertically aligned ZnO nanowires grown on the ZnO epilayer; (b) ZnO nanobelts on the junction bwteeen the epilayer and sapphire, (c) tilt aligned ZnO nanowires on c-plane sapphire.
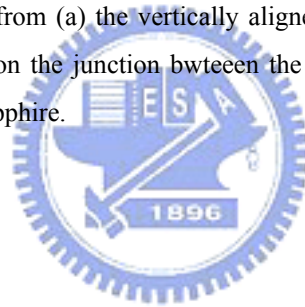
References

[1] Z.W. Pan, Z. R. Dai, Z. L. Wang, *Science* **291,** 1947 (2001).

[2] J. Q. Hu, Q. Li, N. B. Wong, C. S. Lee, and S. T. Lee, *Chem. Mater.* **14,** 1216 (2002).

[3] P. D. Yang, C. M. Lieber, *J. Mater. Res.* 12, 2981 (1997).

[4] W.-J. Li, E.-W. Shi, W.-Z. Zhong and Z.-W. Yin, *J. Cryst. Growth* **203,** 186 (1999).

[5] W. I. Park, D. H. Kim, S. W. Jung, G. C. Yi, *Appl. Phys. Lett.*, **80** 4232 (2002).

[6] J. K. Jian, X. L. Chen, W. J. Wang, L. Dai and Y. P. Xu, *Appl. Phys. A* **76**, 291 (2003).

[7] S. S. Fan, M. G.Chapline, N. R. Franklin, T. W. Tombler, A. M. Cassell, H. J. Dai, 1999 *Science* **283** 512.

[8] L.T. Canham, *Appl Phys Lett* **57,** 1046 (1990).

[9] L. Pavesi, *Riv. Nuovo Cimento* **20,** 1 (1997).

[10] J. Lu,Z. Ye, J. Huang, L. Wang and B. Zhao, *Appl. Surface Sci.* **207,** 29 (2003)

[11] M. H. Huang, S. Mao, H. Feick, H. Q. Yan, Y. Y. Wu, H. Kind, E. Weber, R. Russo , P. D. Yang, *Science* **292,** 1897 (2001).

[12] Z. Gaburro, C. J. Oton, P. Bettotti, L. Dal Negro,G. V. Prakash, M. Cazzanelli, L. Pavesi, *J. Electrochem. Soc.* **150,** C381 (2003).

[13] J. S. Lee, M. I. Kang, S. Kim, M. S. Lee, Y. K. Lee, *J. Cryst. Growth* **249**, 201 (2003).

[14] H. J. Yuan, S. S. Xie, D. F. Liu, X. Q. Yan, Z. P. Zhou, L. J. Ci, J. X. Wang, Y. Gao, L. Song, L. F. Liu, W. Y. Zhou, G. Wang, *Chem Phys. Lett.* **371**, 337 (2003).

[15] P. Yang, H. Yan, S. Mao, R. Russo, J. Johnson, R. Saykally, M. Morris, J. Pham , R. He and H. Choi, *Adv. Funct. Mater.* **12,** 323 (2002).

[16] J. J. Wu and S. C. Liu, *J. Phys. Chem. B,* **106,** 9546 (2002).

[17] A. Nahhas, H.K. Kim, J. Blachere, *Appl. Phys. Lett.*, **78**, 1511 (2001)

[18] H. J. Fan, F. Bertram, A. Dadgar, J. Christen, A. Krost, and M. Zacharias, *Nanotechnology* 15, 1401 (2004).

[19] Y. F. Chen, D. M. Bagnall , H. J. Koh, K. T. Park, K. Hiraga, Z. Q. Zhu, T. Yao, *J. Appl. Phys.* 84, 3912 (1998).

[20] J. B. Baxter and E. S. Aydil, *J. Cryst. Growth* 274, 407 (2005).

[21] H. C. Hsu, Y. K. Tseng, H. M. Cheng, J. H. Kuo, and W.F. Hsieh., *J. Cryst. Growth* 261, 520 (2004).

[22] Y. F. Chen, H. J. Ko, S. K. Hong, T. Yao, and Y. Segawa, *Appl. Phys. Lett.* 80 1358 (2002).

[23] J. M. Calleja and M. Cardona, *Phys. Rev. B* 16 3753 (1977).

[24] F. Decremps, J. Pellicer-Porres, A.M. Saitta, J. C. Chervin, A. Polian, Phys. *Rev. B* 65, 092101 (2002).

[25] N. Ashkenov, B. N. Mbenkum, C. Bundesmann, V. Riede, M. Lorenz, D. Spemann, E. M. Kaidashev, A. Kasic, M. Schubert, M. Grundmann, G. Wagner, H. Neumann, V. Darakchieva, H. Arwin, and B. Monemar, *J. App. Phys.* 93 126 (2003).

[26] C. A. Arguello, D. L. Rousseau, and S. P. S. Porto, *Phys. Rev.* 181, 1351 (1969).

Chapter 5 Optical properties of ZnO nanowires

5.1 Introduction

The various effects and phenomena observed during the interaction of light with matter in an optical experiment are unique to the particular material system under investigation.　The manner in which a material system responds to the impingement of light reveals details of the optical, electronic and nanostructural characteristics of the material.　Light in the form of photons incident on a semiconductor material interacts with the individual electrons that constitute the bound state of the host atoms. In the process, an electron may be excited to a high energy state in the conduction band from which it is rapidly thermalized to the lower unfilled states within the band. Simultaneously, a net positive charge (or the so-called hole) is left in the valance band. In addition to exciting electrons across the band gap, photon interacts with a variety of quasi-particles such as electron-hole pairs with Coulomb interaction (excitons), polaritions, polarons and plasmons.　It is well known that light interacts with the host atoms through the assistance of phonon-photon interaction process.　Compared with the other wide gap materials, ZnO has larger exciton binding energy (~60 meV), which assures more efficient excitonic emission at higher temperatures.　Stimulated emission and lasing at room temperature from exciton-exciton scattering process and electron-hole plasma (EHP) was observed in ZnO epitaxial thin films and bulk. [1,2]

In this chapter, the discussions will be directed to optical properties of the ZnO nanowires with particular emphasis on the interaction of photons with ZnO nanowires. The principal technique employed in this study is photoluminescence (PL). Temperature-dependent and excitation-power-dependent PL was measured to investigate the detailed emission mechanisms.　The basic understanding of the

underlying physics and optical properties in ZnO materials and material structures sheds light on new phenomena with tremendous potential for device applications.

5.2 PL emission under low excitation density

5.2.1 PL from ZnO nanowires grown on textured ZnO buffer layer

The typical room temperature PL spectrum (see Fig. 5-1) of the ZnO nanorods grown on textured ZnO buffer layer shows a sharp emission located at 3.26 eV and another broad emission centered at 2.55 eV. The sharp peak corresponds to the recombination of free exciton and the broad emission is attributed to excess Zn (or oxygen vacancy) or surface state emission. It is not surprising to observe free exciton emission at room temperature due to its large exciton binding energy (60 meV) as aforementioned.
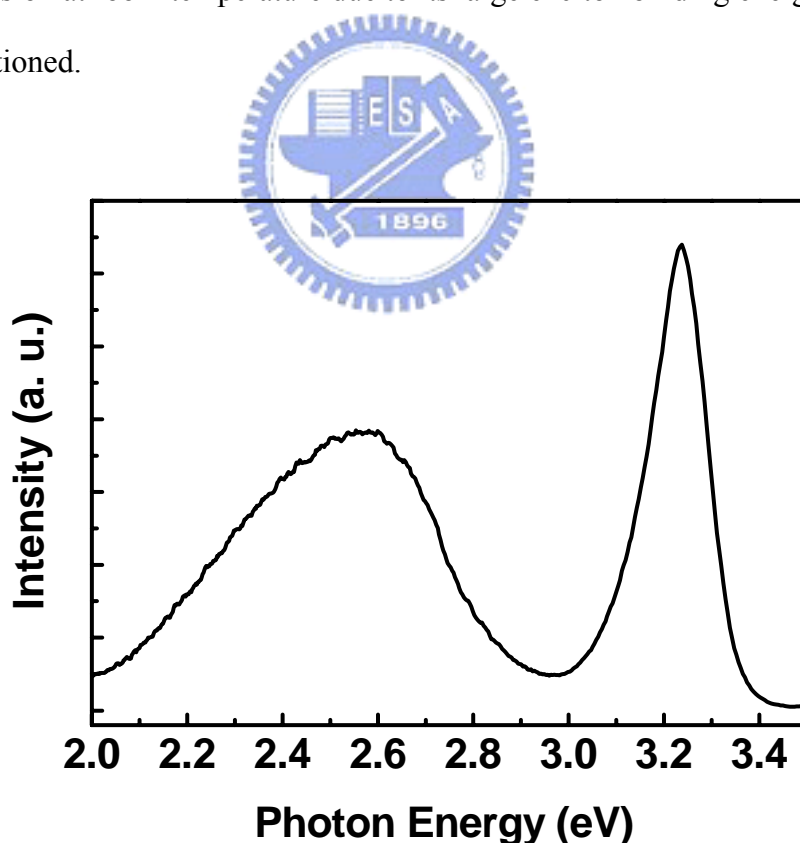
Fig. 5-1 The room temperature PL spectrum of the ZnO nanowires.

Shown in Fig. 5-2 is a near-band edge PL spectrum of ZnO nanorods measured at 6K. Several sharp peaks observed in the range of 3.0 to 3.45 eV were attributed to the exciton-related recombination. The inset in Fig. 5-2 shows the wide range PL spectrum of ZnO nanowires. The feature of the PL spectrum can be also classified into two categories: near band-edge emission and deep-level emission, which is relatively weak. The near band edge emission of the ZnO nanowires is dominated by the bound exciton peak at 3.370 eV, similar to the previous report [3], due to recombination of excitons bound to donors or acceptors, as depicted in Fig. 5. Since the as-grown ZnO thin film is generally *n*-type, the bound exciton peak is most likely related to the excitons bound to the neutral donors (D^oX), even though the origin of the donor level remains a controversial issue.[4-6] On the high energy shoulder of the D^oX peak, the free exciton *A* transition (FXA) is observed at 3.383 eV, representing no evidence of quantum confinement as presented in an earlier report in which the diameter of the wires greatly exceeded 20 nm. A weaker structure at even higher energy represents the FXA (n=2) at 3.425 eV. Generally, in II-VI semiconductors, the binding energies of neutral-donor-exciton complexes are smaller than those of excitons bound to neutral acceptors. Thus, the emission labeled A^oX most probably belongs to the acceptor-exciton complexes.[7] On the lower energy side of the exciton peaks, the phonon replicas of both FXA at 3.322 eV and D^oX at 3.298 eV are identified with the relative energy shift from the exciton peaks by a LO phonon energy, respectively. The higher order LO phonon replicas (up to the 5th order replica of FX) were also observed.
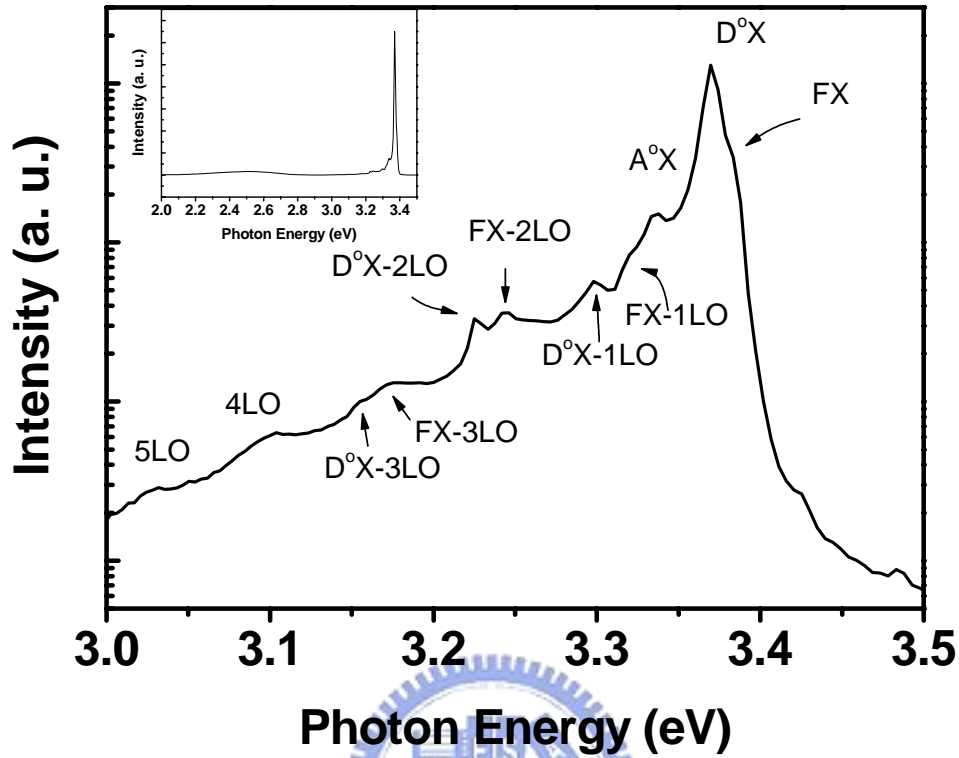
Fig. 5-2 The near-bandedge emission of the ZnO nanowires measured at 6K. The inset shows the wide-range PL spectrum.

In the Franck-Condon model, the coupling strength of the radiative transition to the LO-phonon polarization field is characterized using the Huang-Rhys S-factor.[8] The relative intensity of the n-th phonon replicas (I_n) is related to the zero-phonon peak (I_0) by the S-factor as,

$$I_n = I_0 (S^n e^{-S}/n!), \quad n = 0, 1, 2 \ldots \tag{5-1}$$

From the measured spectra, the S-factor associated with D^oX is estimated to be approximately 0.044, but the S-factor associated with FXA is around 0.325, which is much higher than that for D^oX. It is expected that the coupling of the FXA to the 1LO phonon is stronger than that of D^oX due to larger binding energy of FXA exciton, which is closer to the LO phonon energy (72 meV), as compared with D^oX

exciton. Table 5-1 shows S-factors of the ZnO nanowires and epitaxial layer. It is found that S-factor of the nanowires is more than two times larger than that of the epilayer. It indicates that the strong exciton-phonon interaction in nanowires and thus reducing structure size seems to enhance the probability of exciton-phonon scattering. The exciton-phonon interaction discussion will be discussed in the next section.

Table 5-1 The data of S factor associated with different excitons in ZnO nanorods and epilayer.

	S factor associated with D^oX	S factor associated with FX
ZnO nanorods	0.044	0.325
ZnO epilayer	0.0136	0.186

5.2   PL from ZnO nanowires grown on alumina

The inset in Fig. 5-3(a) shows a typical low temperature PL spectrum measured at 6 K and the near band edge spectrum of the ZnO nanowires, including several individual emission peaks is also depicted in Fig. 5-3(a). The feature of the PL spectrum is basically the same as that grown on the textured ZnO buffer layer, except for the larger broad defect emission in this case. Fig. 5-3(b) displays the near band-edge PL spectra of ZnO nanowires at various temperatures. As the temperature increases, the D^oX peak is quenched more quickly than the FXA emission and the emission peaks move toward lower energies. Observably, the FXA emission becomes the strongest one when the temperature exceeds 75 K. The exciton linewidth is broadened due to scattering of LO phonons and the excitons become thermally ionized on raising the measured temperature. Some of the bound excitons are thermally dissociated into free excitons and its LO-phonon replicas dominate the

PL spectrum. Third-order and even fourth-order LO phonon replicas are observed when the temperature exceeds 200 K, which implies strong coupling of phonon and exciton in ZnO nanowires. Finally, only free exciton emission and its first-order phonon replicas were observed at room temperature.
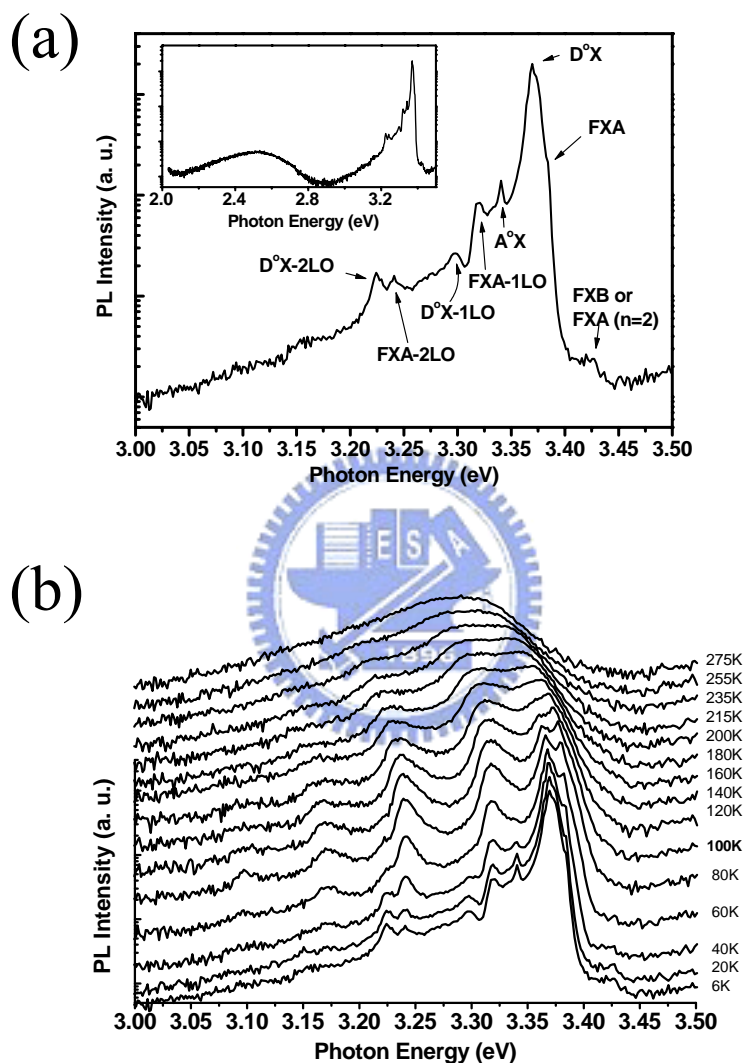
Fig. 5-3 (a) The near band edge emission of the ZnO nanowires measured at 6K. The inset shows the wide-ranged PL spectrum. (b) Temperature dependent PL spectra of the ZnO nanowires.

We also characterize exciton-phonon coupling in the use of the Huang–Rhys factor and found the S factor associated with $D^{o}X$ is ~ 0.01, but around 0.39 for FXA. Again, it reveals strong coupling of FXA to the 1LO phonon than that of $D^{o}X$, and it

is consistent with the ZnO/ZnMgO MQWs system.[12]   On comparison of our previous report on ZnO short nanowires and the epilayer, the S factor correlated with FXA of the nanowires is two times larger than that of the epilayer (0.186) and slightly larger than that of the nanorods (0.325).   These results imply that the strength of the free exciton–LO phonon coupling, which correlates with the crystallinity, is strong in the 1D nanostructure.

The characteristic energy of the LO phonon can be determined from the energy spacing between the exciton resonant lines and their LO phonon replicas.[13]   The LO phonon energy of ZnO crystal is ~72 meV at low temperature, depicted as the dotted line for reference in Fig. 5-4 together with the three physical quantities, FXA-1LO, (FXA-2LO)/2, and (FXA-3LO)/3, marked with solid squares, circles, and triangles, respectively, is shown as functions of temperature.   Notably, the energy softening associated with the FXA-1LO phonon approximately equals 9 meV (phonon energy of 63 meV), the total amount of energy softening of FXA-2LO is only 2 meV, while for FXA-3LO it is 6 meV.   The energy softening of FXA-1LO has been observed in ZnO crystals and other polar semiconductor crystals.   Absorption spectra have shown a ~10% softening of 1LO phonon energy for ZnO crystals [14] and it is theoretically explained by the exciton–polaron model.[15]   Similar phonon softening have also appeared in the low temperature PL spectra of ZnO epilayer films [16-17], which are marked by an open circle and an open square in Fig. 5-4 for comparison.
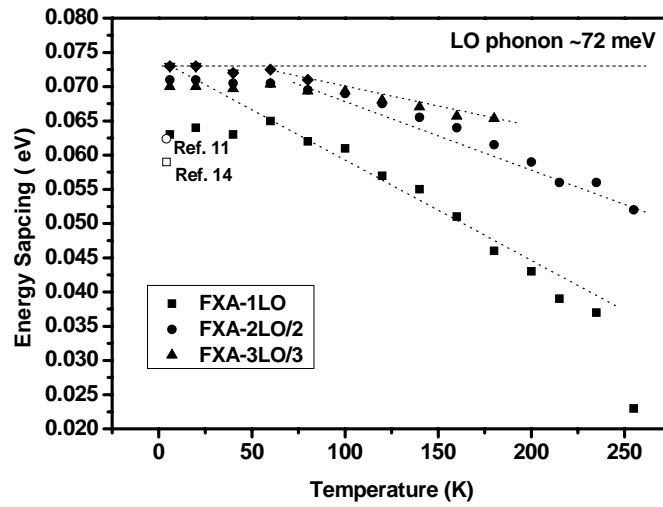
Fig. 5-4   The 1LO phonon energy spacing and 2 LO phonon spacing versus temperature. The dash line at 72 meV is plotted as reference line.   The open square and circle are the values of the ZnO film in Ref. 11 and 14, respectively.

Polaron formation was used to describe the dispersion relations of phonons and excitons, which will be split into two new phonon-like and exciton-like dispersion curves under the strong exciton–phonon coupling.[7]   Because ZnO has a free exciton binding energy of 60 meV, which is almost resonant with the LO phonon energy of 72 meV, the excitation is transferred to the excitonic polaron.   However, the bound exciton–phonon coupling of ZnO is far from resonance because of the relatively small binding energy of the bound exciton (~several meV).   This explains the fact that the S-factor of FXA-1LO is much larger than that of $D^{o}X$-1LO.

We also indicate in Fig. 5-4 that all the phonon energy of the phonon replica declines with the temperature increasing over 75 K.   The temperature-dependence of the phonon energy shift can be explained by Permogorov's theory [18], which states that

(i) the shift of the spectral maximum from its low-energy threshold increases linearly with temperature, $\Delta=(L+1/2)k_{B}T$, and hence also the energy spacing between the

zero-phonon and its phonon replicas;

(ii) the probability of one phonon scattering is approximately proportional to the excitonic kinetic energy, i.e. $(3/2)k_BT$ or L=1; and

(iii) for two phonon scattering, the annihilation probability is independent of the excitonic kinetic energy, that is L=0.

The temperature dependence of the various phonon replicas of FXA of our ZnO nanowires shows basically linear behavior beyond 75 K with the slope of the temperature dependent curve of FXA-1LO replica approximately equal to $(-3/2)k_B$, in accordance with the Permogorov's theory, but it becomes flattened below 75 K as indicated in Fig. 5-4.　However, the slope is close to $-k_B$ for FXA-2LO and close to $(-1/2)k_B$ for FXA-3LO.　The larger slope for the FXA-2LO line might be attributed to combination of the second order exciton phonon scattering and cascading phonon scattering.　It is still an open issue.　On the other hand, the strong exciton and phonon interaction leads to the excitation of the excitonic polaron with large energy softening of the FXA-1LO phonon, which causes a flattening of the curve at low temperatures in the energy spacing versus temperature plot in Fig. 5-4.　The phonon scattering processes become dominated at temperatures higher than 75–100 K, which is roughly equal to energy spacing between 6 and 9 meV.　The flattening effect also appeared in GaN films in Fig. 5-4 of Ref. [13] at around 15 K or ~1 meV, which is the energy spacing of the exciton–phonon interaction of GaN.

5.2.2 PL from ZnO nanowires grown on porous Si

Fig. 5-5(a) shows temperature-dependent near band-edge PL spectra of ZnO nanowires.　As the temperature is increased, the energy peaks shift to the low-energy side due to the decrease of the band gap.　The deconvolution of the low temperature (7K) PL spectrum ranged from 3.34 eV to 3.39 eV by a series of Lorentzian line

profiles, as depicted in Fig. 5-5(b), the dominant luminescence lines at 3.358, 3.363, and 3.372 eV are assigned as two exciton–bound–to–defect emissions and a free exciton (FX) emission, respectively. On the lower energy side of the exciton peaks, the longitudinal optical (LO) mode of the FXA at 3.31 eV and the peak at 3.24 eV are identified by the relative energy shift from the exciton peaks of higher order LO phonon replicas. The strong exciton-phonon coupling in ZnO nanowires affects the FXA-1LO phonon energy spacing because of the excitonic polaron formation. A further increase in temperature causes the bound excitons localized by the defects to become free excitons, resulting in enhanced emission from the free excitons. Observably, the FX emission becomes the strongest when the temperature exceeds 30 K. As the temperature increases, the exciton linewidth is broadened due to scattering with LO phonons and the excitons become thermally ionized. The PL intensity exponentially decreases with increasing temperature due to the thermal ionization of exciton and thermally activated nonradiative recombination mechanisms. Some of the bound excitons are thermally dissociated into free excitons, and the free excitons and their LO-phonon replicas dominate the PL spectrum. Finally, only free exciton emission and its one phonon replica can be observed at room temperature.

The dependence of the integrated PL intensity of the UV band on temperature is given in Fig. 5-5(c). The temperature dependence of the PL intensity can be expressed by the Arrhenius expression:

$$I(T) = \frac{I_0}{1 + A \exp(\frac{-\Delta E}{k_B T})},$$
(5-2)

where ΔE is the activation energy of the thermal quenching process, k_B is the Boltzmann constant, I_0 is the emission intensity at 0 K, T is the thermodynamic temperature, and A is a constant. The result shows that the activation energy of about 55.7 meV is in agreement with the exciton binding energy of 60 meV for bulk

ZnO crystal, which further supports our assessment that this emission band is from free exciton recombination.

In use of the Arrhenius-plot analysis, the activation energies of the two exciton-to-defect emissions were also obtained, corresponding to 8.8 meV and 13.6 meV. These values are in agreement with the binding energies of the exciton emission bound to neutral donors for the I_2 and I_4 emission lines, respectively.[19,20] In addition, the exciton binding energies for the I_2 and I_4 lines estimated from their spectral positions are 9 and 14 meV, respectively, which agree well with the values calculated from temperature-dependent PL. These values are found to be exactly the same as the activation energy for thermal release of excitons from the neutral donors: $(D°,X) \rightarrow D° + X$.
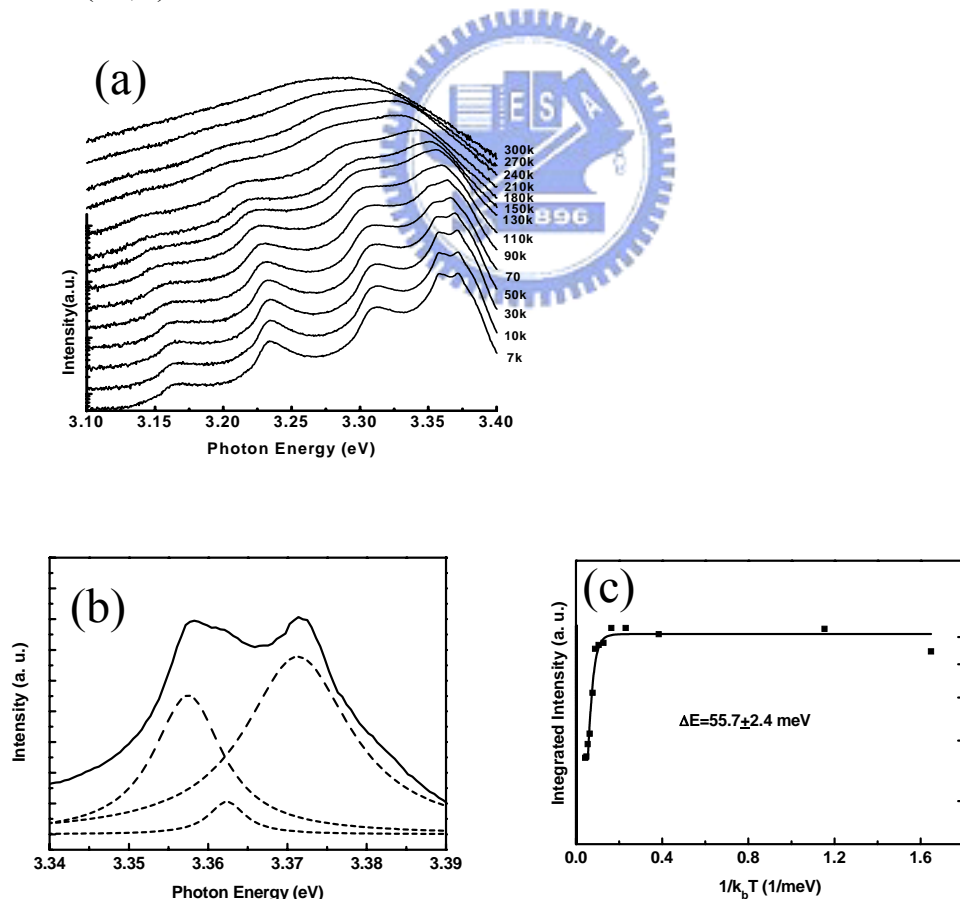
Fig. 5-5 (a) PL spectra of ZnO nanowires at temperature range 7 to 300 K. The intensities are plotted logarithmically. (b)The fitting results of PL measured at 7 K. (c) Integrated intensity of the free exciton of ZnO nanowires as function of temperature with theoretical fitting curve.

5.3.3 Comparison of PL from different morphologies of 1D nanostructures

Fig. 5-6 shows the morphologies of the well-align nanowires, tilted-growth nanowires and nanobelts, respectively. Figure 5-7(a)-(c) show their corresponding CL spectra. All of the emission bands are composed of a sharp UV band around 3.26 eV and a green band around 2.5 eV. As aforementioned, the UV peak is correlated to the exciton-related emission near the band-edge, usually be reported as the recombination of free exciton.[22] The broad green emission band is commonly observed in the PL spectra of nominally undoped ZnO thin films.[22,23] and nanostructures.[24-26] Recent studies on the recombination mechanisms responsible for the green emission in ZnO phosphors have specifically suggested that the green PL arises from the recombination of electrons in singly occupied oxygen vacancies with photogenerated holes in the valence band.[27] The vacancy defect centers exist primarily in the thin (~30nm) electron-depletion layer near the surface of ZnO.

The vertically aligned nanowires have the highest intensity ratio of UV emission to green emission, whereas, the nanobelts have the lowest ratio. It indicates that the more oxygen vacancy or surface state exist in belts. A previous study on vertically ZnO nanowires found that the intensity of the UV (green) emission has maximum (minimum) along (perpendicular to) the c axis of the ZnO nanowire and proposed the green emission is generated and emitted from the side of the nanowires.[28] Shalish *et al.* [29] show that the intensity ratio of the UV to green emission decreases while the diameter of ZnO nanowires reduces. They proposed a simple model, *surface-recombination-layer approximation*, to confirm that the surface recombination dominates the green luminescence spectra with diminishing diameter. In our experiment, the emission was collected from the normal direction to the sample surface. Under this geometry, we collected more UV emission along the c-axis from vertically aligned nanowires than that from tilted ones and nanobelts. On the

contrary, the green emission was emitted from the side of the tilted wires and nanobelts because it generates from the recombination between holes trapped at the surface defects of the sidewall and electrons trapped at the oxygen vacancy. That is the reason why it is easier to observe the green emission from the random-oriented nanowires[30] and nanobelt.[31]
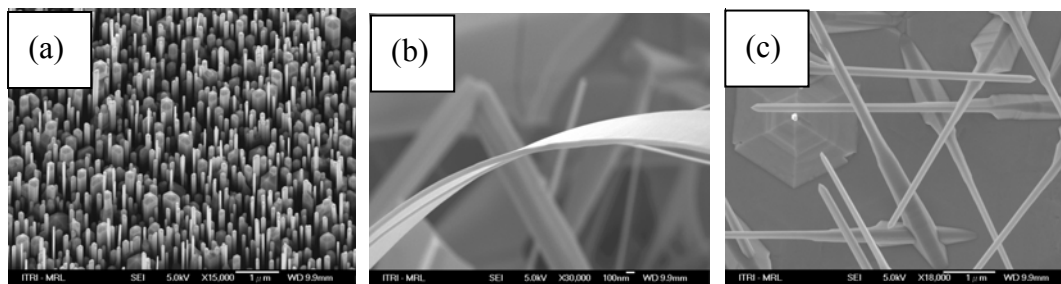
Fig. 5-6 High-magnification SEM images of the synthesized ZnO nanostructure on the ZnO epilayer (a), *c*-plane sapphire (b), junction bwteeen the epilayer and sapphire (c).
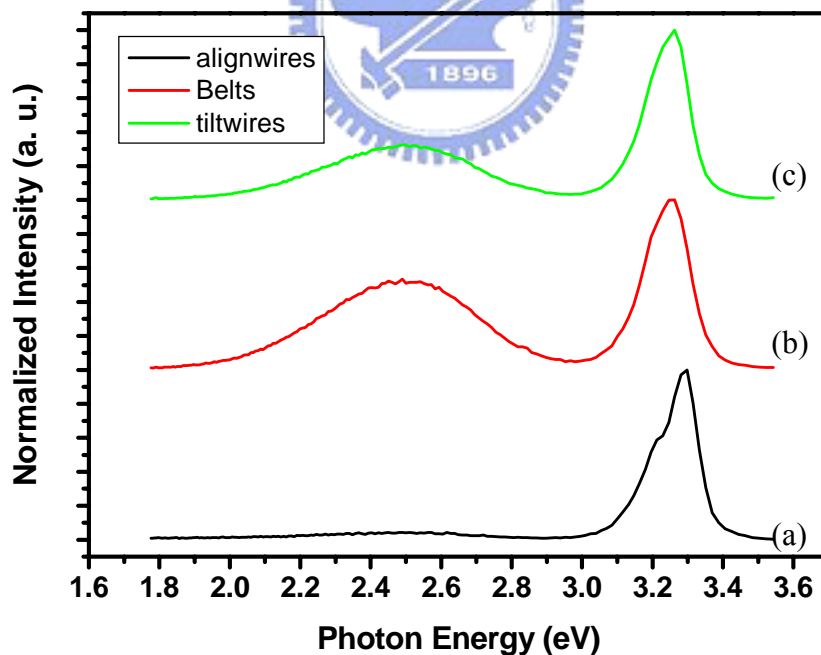
Fig. 5-7 Room-temperature PL spectra from (a) the vertically aligned ZnO nanowires grown on the ZnO epilayer; (b) ZnO nanobelts on the junction bwteeen the epilayer and sapphire.; (c) tilt aligned ZnO nanowires on *c*-plane sapphire

5.5 Stimulated emission and lasing under high excitation density

One-dimensional semiconductors have become the important fundamental building blocks because of their fundamental physical properties and their potential applications for nano-electronic and nano-photonic devices.[33,34]   ZnO nanowires are especially interesting because they exhibit large exciton binding energy (60meV), wide band gap (3.37eV), and low threshold ultraviolet lasing.[35]   Recent progress in lasing or stimulated emission has been achieved from a variety of low dimensional ZnO structures such as micro-cavity[36], nanowires, [35,37-40] nanorods,[41-43] and nanoribbons.[44]   For large diameter such as ZnO micro-cavity,[36] the lasing mechanism results from whispering gallery modes (WGMs).   The light is trapped proximity to the perimeter of nanowire by the total internal reflections (TIR).   When the diameter of the ZnO nanowire is smaller than the optical wavelength, the WGMs will experience high scattering loss as a result of diffraction.   Fabry-Perot resonator has been used to explain the lasing mode in the individual single nanostructure[35,44-46] and long whiskers[47,48] in which two well-aligned end-faces of the nanowire serve as the Fabry-Perot cavity.

However, in a disorder system of randomly oriented nanowires, coherent photon may exist during multiple scattering among these disordered nanowires.   Unlike the conventional laser, the random laser emission in disorder media of polycrystalline ZnO films and powders is a result of the coherent photon scattering that did not contain any conventional Fabry-Perot cavities.[49-51]   The key factor to random lasing is the existence of a high-gain medium and efficient light scattering in the samples to provide the necessary coherent feedback.   Due to the high-gain characteristic of the ZnO nanowires,[35] random lasing also acts in high-density vertically aligned ZnO nanorod arrays.[52]   The different resonant cavities formed by multiple scattering could have different lasing directions.   In this section, we demonstrate the stimulated emission and lasing of randomly oriented disordered ZnO

nanowires and discuss their relevant mechanisms. By Fourier transforming the lasing spectrum, we obtained a characteristic loop length of random lasing cavity.

Figure 5-8(a) shows the typical emission spectra of the ZnO nanowires measured at various pumping intensities. As a reference, the cw-PL is also shown at the bottom of this figure. At low pumping intensity, only a spontaneous emission peak at 3.26 eV with a full width at half maximum (FWHM) of 110 meV is attributed to the exciton emission. With increasing the pumping intensity, a narrow emission appears on the low-energy shoulder of the exciton band. By decomposing the emission spectrum into a broad spontaneous emission and a sharper peak, we observed that the integrated intensity of the broad spontaneous emission increases almost linearly with pumping intensity ($I_{sp}=I_P^{0.95}$), illustrated as close circles in Fig. 5-8(b); however, the integrated intensity of the narrower peak at 3.22 eV experiences a strong superlinear dependence ($I_{st}=I_P^{2.95}$) of the excitation intensity (open circles). As shown in Fig. 5-8(c), the FWHM of the sharper peak is only 20 meV. These results indicate a clear evidence of stimulated emission. The stimulated emission process was interpreted in terms of inelastic exciton-exciton scattering in which one exciton is scattered into a photonlike polariton state giving rise to luminescence, while the other exciton is scattered into an excited state with a larger quantum number or a totally dissociated state. [53]

When the pumping intensity exceeds a certain threshold at a specific position of the sample, shown in Fig. 5-9(a), we found several sharp peaks emerge from 3.20 to 3.25eV with FWHM ~2 meV. Note that the red shift of the PL peak with increasing excitation intensity is caused by the band-gap renormalization.
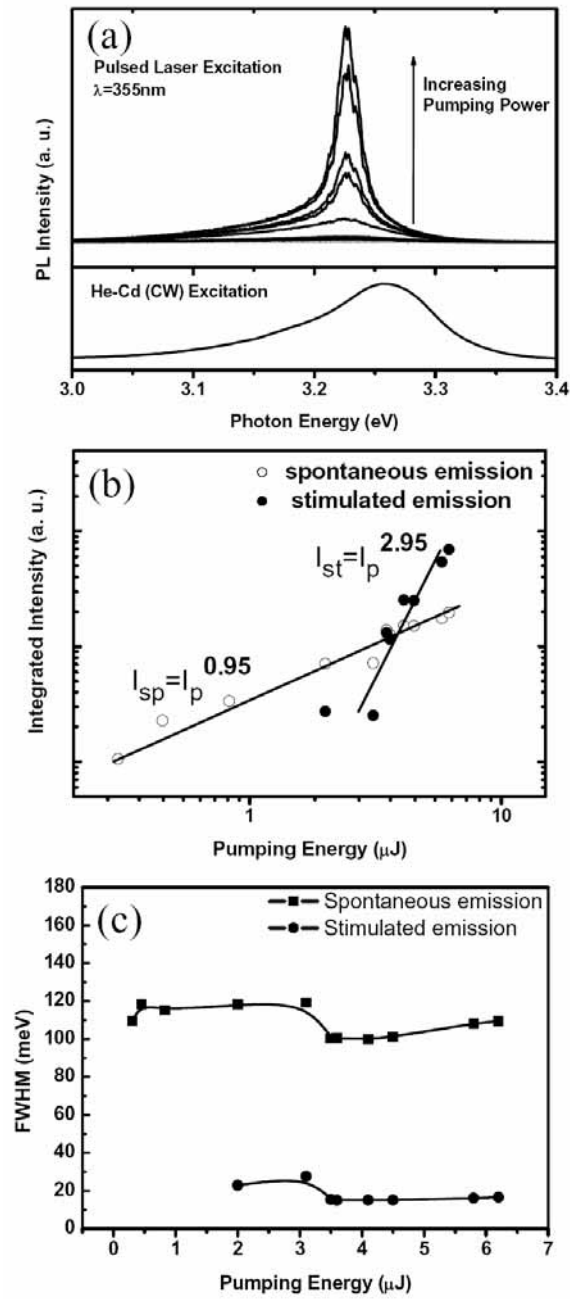
Fig. 5-8 (a) Excitation power dependence of emission spectra of ZnO nanowires. (b) Plot of integrated intensity of the stimulated emission of ZnO nanowires versus the pumping intensity. (c) The FWHM of the emission peaks versus pumping intensity.

There are two possible optical resonance modes in ZnO nanowires for laserlike action. The first resonance mode is the Fabry–Perot mode of the natural optical cavity formed by the two-end facets of the well-organized nanowires which is a well-accepted reason for explaining the lasing behavior in a single ZnO nanowire [35]

and GaN nanowire.[46]   Another possible lasing mechanism results from light amplification due to photon coherent scattering in the random media.[49][50][51] Compared with the previous reports of lasing from ZnO nanowires,[35] our samples show an unobvious feature of Fabry–Perot modes.   The longitudinal modes spacing can be determined by the equation,

$$\Delta\lambda = \lambda^2 /(2nL)$$. (5-3)

Here L is the laser cavity length, n is the refractive index (2.45), and is the resonant wavelength (~390 nm).   For a ZnO nanowire with length of about 3 μm, the mode spacing between the closest longitudinal modes is expected to be 10 nm.   It should exist only a single Fabry–Perot mode in the whole measured PL range (3.0–3.4 eV) and may become a broad lasing spectrum due to averaging out the emission spectra of the single Fabry–Perot modes having different lengths.   However, we did observe several sharp lasing modes under high pumping intensity.   Therefore, we further considered the other possible lasing action from coherent photon scattering in the random medium.
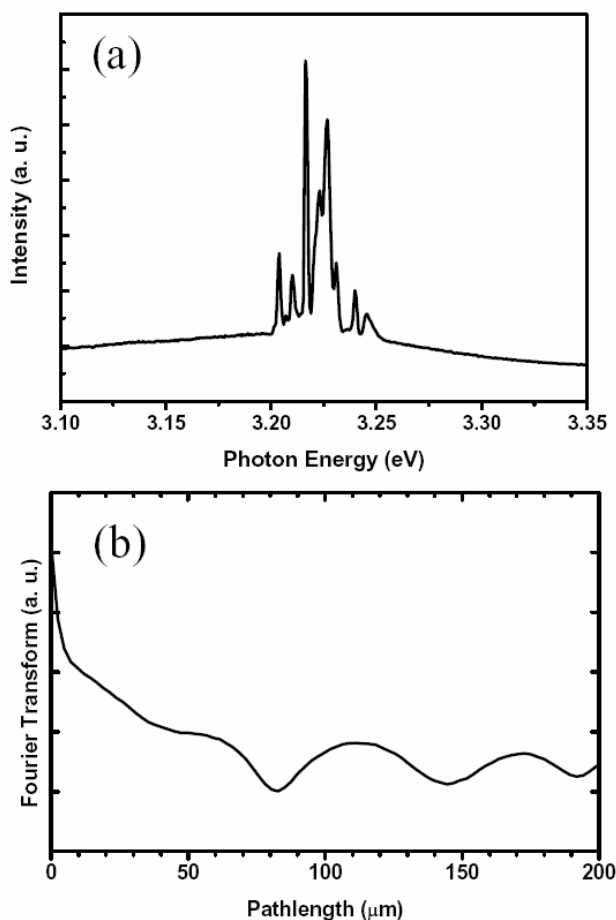
Fig. 5-9 (a) Typical lasing spectra of ZnO nanowire. The excitation intensity is about 2 MW/cm^2; (b)
    Fourier Transform of the lasing spectrum shown in Fig 3 (a).

To confirm the origin of the laserlike emission peaks, we studied the influence of

the excitation area on the number of modes in the random lasing. Figure 5-10 plots

the emission spectra measured at different excitation areas slightly above the lasing

threshold. Under the smallest excitation area $\sim 7.9 \times 10^{-5}$ cm^2, no narrow emission

peak was observed. With increasing the excitation area, several sharp laserlike

emission peaks appear. In addition, the number of sharp laserlike peaks tends to

increase with increasing excitation area. According to the previous report on

random lasing,[49] the laser oscillation would not have occurred if the closed-loop

paths were too short to provide enough amplification. This result clearly indicates

that the sharp emissions result from the random lasing action. The scattering

probability of coherent photon in random-oriented ZnO nanowires is higher than that in well-aligned ZnO nanowires. We found no distinct sharp peaks from the well-aligned ZnO nanowires grown on a quartz glass[54] with optical pumping. Hence, random laser only acted in high-density vertically aligned ZnO nanowires[52] or disorder-oriented ZnO nanowires.
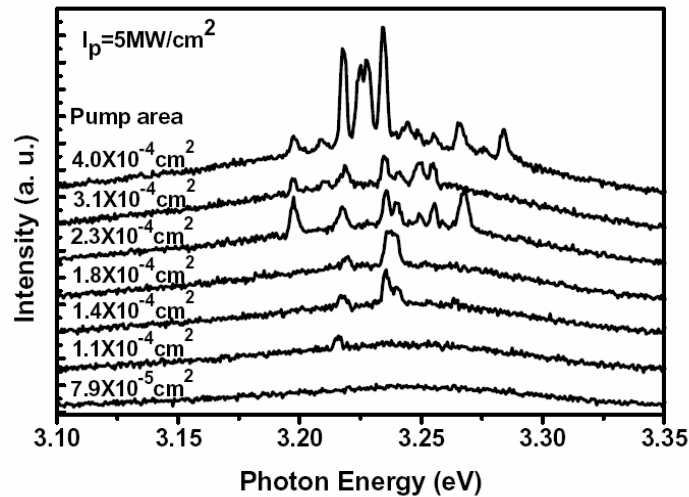
Fig. 5-10 Lasing spectra of the sample of different excitation area (from top to bottom for decreasing area).

To further determine the cavity length of the closed-loop random lasing, a simple and powerful technique which is Fourier transform (FT) of the lasing spectrum is used.[55-56] The unit of the FT result is in length provided that the unit of the lasing spectrum is in wave number (1/length). For a traditional Febry–Perot laser cavity, the separation of harmonics in FT of the lasing emission is nL/π. We assume that the closed-loop paths of the coherent photon are approximately circles, then the optical path 2L is replaced by the circumference of the loop, and the resultant FT harmonics appear at the multiples of nD/2, where D is the loop diameter.

Fig. 5-9(b) is the FT of the laser emission spectrum of Fig. 5-9(a). We found a broad peak at 20 μm and a series of peaks of the harmonics that appear at 56, 112, and 168 μm, respectively. In fact, the broad peak contains many individual peaks that

74

are belonging to several short laser cavities within the illuminated area. The fundamental resonator of random lasing has a diameter of 56 μm. The calculated loop diameter of the random laser is smaller than the spot size of the pumping laser beam on the sample.

5.6 Summary

The LO phonon-assisted luminescence of the donor-bound excitons and free excitons in ZnO nanowires were studied at various temperatures. The strong exciton–phonon coupling in ZnO nanowires affects not only the S factor but the FXA-1LO phonon energy spacing, which can be explained by the excitonic polaron formation. The S factor associated with FXA of the nanowires is larger than that of the epilayer. The flattening of the energy spacing of FXA-1LO phonon replicas is attributed to formation of the excitonic polaron and the exciton–phonon scattering dominates when the temperature exceeds the binding energy of the excitonic polaron. Furthermore, we deduced the activation energies of free and bound excitons from the temperature dependent photoluminescence spectra.

We have shown stimulated emission of randomly grown oriented-ZnO nanowires under optically pumping. Below the lasing threshold, the stimulated emission shows superlinear dependence of the pump-intensity. Above the lasing threshold, several sharp peaks with FWHM ~2 meV were observed. The random laser action requires long enough path length of closed-loop to generate photon amplification via coherent feedback scattering. If the path length of closed-loop was reduced to below a critical length, the laser action stopped. Random lasing is more easily realized in disorder grown oriented-ZnO nanowires than well aligned ZnO nanowires because of short mean-free path of coherent light scattering in the former case. Finally, the typical

cavity length of the random laser can be roughly determined by Fourier transforming

the lasing spectrum.

References

[1] D. M. Bagnall, Y. F. Chen, Z. Zhu, T. Yao, S. Koyama, M. Y. Shen, and T. Goto, Appl. Phys. Lett. **70**, 2230 (1997).

[2] Z. K. Tang, G. K. L. Wong, P. Yu, M. Kawasaki, A. Ohtomo, H. Koinuma, and Y. Segawa, Appl. Phys. Lett. **72**, 3270 (1998).

[3] W. I. Park, Y. H. Jun, S.W. Jung, and G. C. Yi, *Appl. Phys. Lett.* **82** 964 (2003).

[4] D. C. Look, J. W. Hemsky, and J. R. Sizelove, *Phys. Rev. Lett*. **82** (1999) 2552.

[5] C. G. Van de Walle, *Phys. Rev. Lett.* **85** (2000) 1012.

[6] S. F. J. Cox, E. A. Davis, S. P. Cottrell, P. J. C. King, J. S. Lord, J. M. Gil, H.V. Alberto, R. C. Vilão, J. Piroto Duarte, N. Ayres de Campos, A. Weidinger, R. L. Lichti, and S. J. C. Irvine, *Phys. Rev. Lett*. **82** (1999) 2552.

[7] C. F. Klingshirn, *Semiconductor Optics,* Springer, Verlag Berlin Heidelberg, 1994.

[8] K. Huang and A. Rhys, *Proc. R. Soc. London A* **204** (1950) 406.

[9] B. Di Bartolo and R. Powell, *Phonon and Resonance in Solids,* Wililey, New York, 1990.

[10] C. C. Chen and C. C. Yeh. *Adv. Mater.* **12,** 738 (2000).

[11] S. C. Lyu, O. H. Cha, E.-K. Suh, H. Ruh, H. J. Lee and C. J. Lee. *Chem. Phys. Lett.* **367,** 136 (2003).

[12] H. D. Sun, Y. Segawa, M. Kawasaki, A. Ohtomo, K. Tamura and H. Koinuma. *J. Appl. Phys.* **91,** 6457 (2002).

[13] S. J. Xu, W. Liu and M. F. Li. *Appl. Phys. Lett.* **77,** 3376 (2000).

[14] W. Y. Liang and A. D. Yoffe. *Phys. Rev. Lett.* **20,** 59 (1968).

[15] Y. Toyozawa and J. Hermanson. *Phys. Rev. Lett.* **21,** 1637 (1968).

[16] Y. Chen, H. J. Ko, S. K. Hong and T. Yao. *Appl. Phys. Lett.* **76,** 559 (2000).

[17] Y. Chen, S. K. Hong, H. J. Ko, M. Nakajima and T. Yao. *Appl. Phys. Lett.* **76,**

245 (2000).

[18] S. Permogorov. In: E.I. Rashba and M.D. Sturge, Editors, *Excitons*, North-Holland, Amsterdam (1982).

[19] R. Heitz, C. Fricke, A. Hoffmann, and I. Broser *Mater. Sci. Forum* **83** 1241 (1992).

[20] H. J. Ko, Y. F. Chen, T. Yao, K. Miyajima, A. Yamamoto, T. Goto, *Appl. Phys. Lett.* **77**, 537 (2000).

[21] Y. F. Chen, H. J. Ko, S. K. Hong, T. Yao, and Y. Segawa, *Appl. Phys. Lett.* **80** 1358 (2002).

[22] J. F. Muth, R. M. Kolbas, A. K. Sharma, S. Oktyabrsky, and J. Narayan, *J. Appl. Phys.* **85,** 7884 (1999).

[23] K. Vanheusden, W. L. Warren, C. H. Seager, D. R. Tallant, J. A. Voigt, and B. E. Gnade, *J. Appl. Phys.* **79,** 7983 (1996).

[24] M. H. Huang, Y. Wu, H. Feick, N. Tran, E. Weber, and P. D. Yang, *Adv. Mater.* (Weinheim, Ger.) **13,** 113 (2001).

[25] B. D. Yao, Y. F. Chan, N. Wang, *Apph. Phys. Lett.* **81**, 4 (2002).

[26] V. A. L. Roy, A.B. Djurisic, W.K. Chan, J. Gao, H.F. Lui, and C. Surya. A*ppl. Phys Lett.* **83**, 141 (2003).

[27] K. Vanheusden, W.L. Warren, C.H. Seager, D.R. Tallant, J.A. Voigt, B.E. Gnade, *J. Appl. Phys.* **79**, 7983 (1996).

[28] N. E. Hsu, W. K. Hung, Y. F. Chen, *J. Appl. Phys* **96**, 4671 (2004)

[29] I. Shalish, H. Temkin, V. Narayanamurti, *Phys. Rev. B* **69**, 245401 (2004).

[30] J. Q. Hu, Q. Li, N. B. Wong, C. S. Lee, and S. T. Lee, *Chem. Mater.* **14**, 1216 (2002).

[31] Y. B. Li, Y. Bando, T. Sato, and K. Kurashima, *Appl Phys. Lett*. **81**, 144 (2002).

[32] X. F. Duan, Y. Huang, R. Agarwal, and C. M. Lieber, *Nature* (London) **421**, 241

(2003).

[33] S. S. Wong, E. Joselevich, A. T. Woolley, C. L. Cheung, and C. M. Lieber, *Nature* (London) **394**, 52 (1998).

[34] X. F. Duan, Y. Huang, Y. Cui, J. F. Wang, and C. M. Lieber, *Nature* (London) **409**, 66 (2001).

[35] M. H. Huang, S. Mao, H. Feick, H. Q. Yan, Y. Y. Wu, H. Kind, E. Weber, R. Russo, and P. D. Yang, *Science* **292**, 1897 (2001).

[36] X. Liu, W. Fang, Y. Huang, X. H. Wu, S. T. Ho, H. Cao, and R. P. H. Chang, *Appl. Phys. Lett.* **84**, 2488 (2004).

[37] C. H. Liu, J. A. Zapien, Y. Yao, X. M. Meng, C. S. Lee, S. S. Fan, Y. Lifshitz, and S. T. Lee, *Adv. Mater.* (Weinheim, Ger.) **15**, 838 (2003).

[38] J. H. Choy, E. S. Jang, J. H. Won, J. H. Chung, D. J. Jang, and Y. W. Kim, *Appl. Phys. Lett.* **84**, 287 (2004).

[39] J. C. Johnson, H. Q. Yan, P. D. Yang, and R. J. Saykally, *J. Phys. Chem. B* **107**, 8816 (2003).

[40] Z. R. Qiu, K. S. Wong, M. M. Wu, W. J. Lin, and H. F. Xu, *Appl. Phys. Lett.* **84**, 2739 (2004).

[41] J. H. Choy, E. S. Jang, J. H. Won, J. H. Chung, D. J. Jang, and Y. W. Kim, *Adv. Mater.* (Weinheim, Ger.) **15**, 1911 (2003).

[42] Y. K. Tseng, H. C. Hsu, W. F. Hsieh, K. S. Liu, and I. C. Chen, *J. Mater. Res.* **18**, 2837 (2003).

[43] A. B. Hartanto, X. Ning, Y. Nakata, and T. Okada, *Appl. Phys. A: Mater. Sci. Process.* **78**, 299 (2004).

[44] H. Q. Yan, J. Johnson, M. Law, R. R. He, K. Knutsen, J. R. McKinney, J. Pham , R. Saykally, and P. D. Yang, *Adv. Mater.* (Weinheim, Ger.) **15**, 1907 (2003).

[45] J. A. Zapien, Y. Jiang, X. M. Meng, W. Chen, F. C. K. Au, Y. Lifshitz, and S. T.

Lee, *Appl. Phys. Lett.* **84**, 1189 (2004).

[46] J. C. Johnson, H. J. Choi, K. P. Knutsen, R. D. Schaller, P. D. Yang, and R. J. Saykally, *Nat. Mater.* **1**, 106 (2002).

[47] D. X. Zhao, Y. C. Liu, D. Z. Shen, Y. M. Lu, L. G. Zhang, and X. W. Fan, *J. Appl. Phys.* **94**, 5605 (2003).

[48] Y. G. Wang, C. Yuen, S. P. Lau, S. F. Yu, and B. K. Tay, *Chem. Phys. Lett.* **77**, 329 (2003).

[49] H. Cao, Y. G. Zhao, S. T. Ho, E. W. Seelig, Q. H. Wang, and R. P. H. Chang, *Phys. Rev. Lett.* **82**, 2278 (1999).

[50] R. K. Thareja and A. Mitra, *Appl. Phys. A: Mater. Sci. Process.* **71**, 181 (2000).

[51] X. H. H. Wu, A. Yamilov, H. Noh, H. Cao, E. W. Seelig, and R. P. H. Chang, *J. Opt. Soc. Am. B* **21**, 159 (2004).

[52] S. F. Yu, C. Yuen, S. P. Lau, W. I. Park, and G.-C. Yi, *Appl. Phys. Lett.* **84**, 3241 (2004).

[53] C. F. Klingshirn, *Semiconductor Optics* (Springer, Berlin, 1995).

[54] S. Yang, H.C. Hsu, W.R. Liu, and W.F. Hsieh, submitted.

[55] R. C. Polson, A. Chipouline, and Z. V. Vardeny, *Adv. Mater.* (Weinheim, Ger.) **13**, 760 (2001).

[56] R. C. Polson, G. Levina, and Z. V. Vardeny, *Appl. Phys. Lett.* **76**, 3858 (2000).

Chapter 6 Structure and optical properties of ZnMgO nanowires

6.1 Introduction

The most challenge of realizing the photonic devices based on ZnO nanowires are *p*-type doping technique, heterostructures, and bandgap engineering. A desire to produce ultraviolet (UV) emitting/detecting nanodevices are required for a number of applications, such as sensing of chemical and biological contaminants, biological agent detection, sterilization, and tunable solid-state lighting. Various groups around the world are attempting to achieve shorter-wavelength operation, while at the same time improving the output power and extraction efficiency of their devices.

Alloying ZnO phase with MgO and ZnS has been investigated for widening the bandgap of the ZnO-based nanowires. A blue-shift of the UV emission compared to that of the pure ZnO nanowires have observed while sulfur was doped into ZnO nanowires. [1,2] The room-temperature (RT) photoluminescence [3] and absorption spectra [4] of the well-aligned ZnMgO were tuned by adjusting Mg concentration. However, no reported studies on stimulated emission (SE) in ZnMgO alloy nanowires. In this chapter, we demonstrate a simple method to achieve the bandgap engineering in core-shell ZnO-MgO nanowires by using Mg diffusion. With increasing annealing temperature, the diffused concentration of Mg was increased as a result of the PL UV-shift. Furthermore, we report the observation of stimulated emission (SE) from optically pumped ZnMgO nanowires for the first time.

81

6.2 Experimental details

Synthesis of ZnO nanostructure was fabricated in a simple vapor transport process. Zinc powder (99.9999%) and Mg powder (99.6%) with Mg:Zn weight ratios of 1:19 were placed in a ceramic boat as the starting materials. An *a*-plane sapphire wafer was used as a substrate. The boat was positioned in the center of the quartz furnace tube and the substrate was placed 10 mm downstream from the mixed powder. Prior to heating the furnace, the quartz tube was purged with high-purity argon gas for 3 min twice. The system was heated increased to 570 °C with an Argon flow rate of 500 sccm and kept at this temperature for 60 min. After the wire growth, the products were subsequently heat-treated under ambient atmosphere pressure for 120 min from 800$^{\rm o}$C to 1000$^{\rm o}$C. After the reaction was completed, the system was cooled to the ambient temperature and a gray-white colored product was found deposited on the substrate.
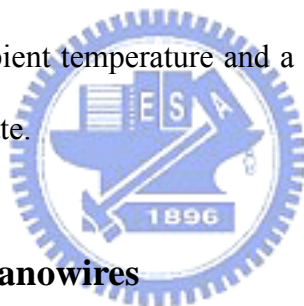
6.3 Growth of MgZnO nanowires

Figure 6-1(a) shows the SEM images of the products for as-grown. All the morphologies of the products are nanowire- shape with diameters of about 200-500 nm and lengths of over 5 μm. Figure 6-1(b) shows the EDX pattern of as-grown nanowires, indicating that mainly composed of Mg and O, with a small amount of Zn. The typical XRD pattern of the nanowires is shown in Fig. 6-2. All relatively sharp diffraction peaks can be perfectly indexed to a high crystallinity of the hexagonal structure of ZnO and faced-center cubic structure of MgO. The TEM image of as-grown nanowires illustrated in Fig. 6-3 (a) shows the individual nanowire displays difference in brightness between the core and sheath regions. The core structure has a diameter of about 90 nm and the sheath region has diameter of 600 nm. EDX pattern as shown in Fig. 6-3(b) indicates that the nanowire is composed of Mg and O

82

with a small amount of Zn.　The HRTEM image taken from the edge of nanowire, in Fig. 6-3(c), shows a perfect lattice plane with the inter-planar spacing of 2.1 nm, in good agreement with the (002) spacing of MgO.　The selection-area electron diffraction (SAED) pattern of this region as shown in Fig. 6-3(d) shows the outer layer of the nanowires is single-crystalline MgO with a cubic rock salt structure. From the above observations, we propose that the formation of the nanowires should be ZnO/MgO core-shell heterostructure as drawn in Fig. 6-3(e).
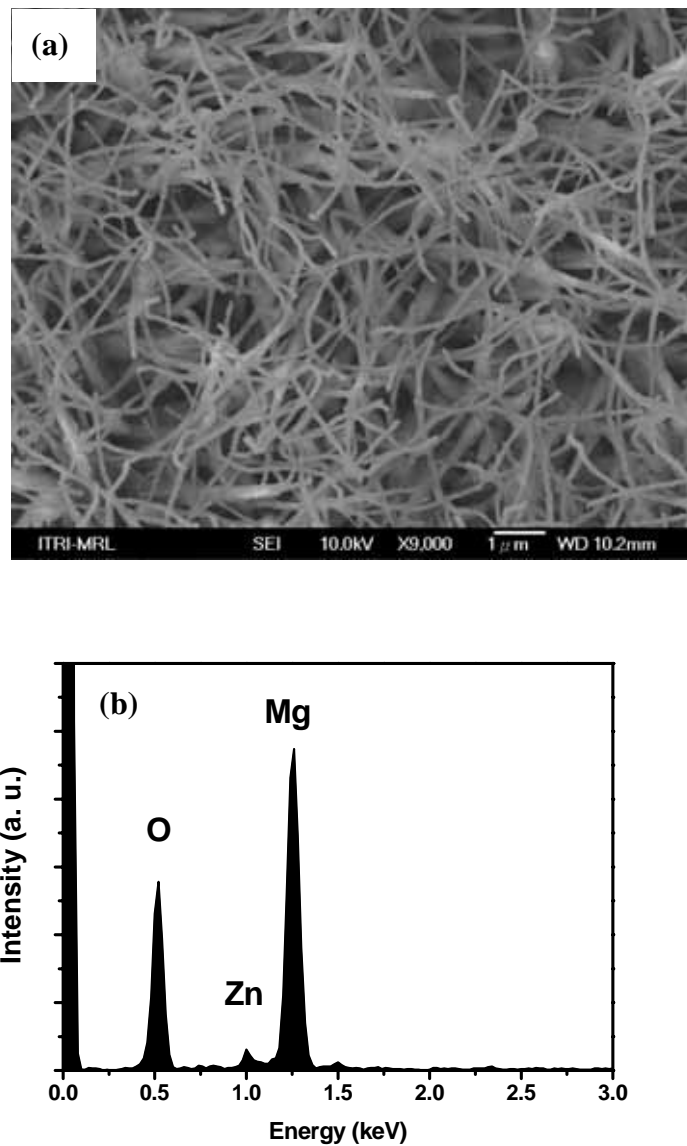
Fig. 6-1 (a) Typical SEM image of as-grown nanowires and (b) EDX pattern
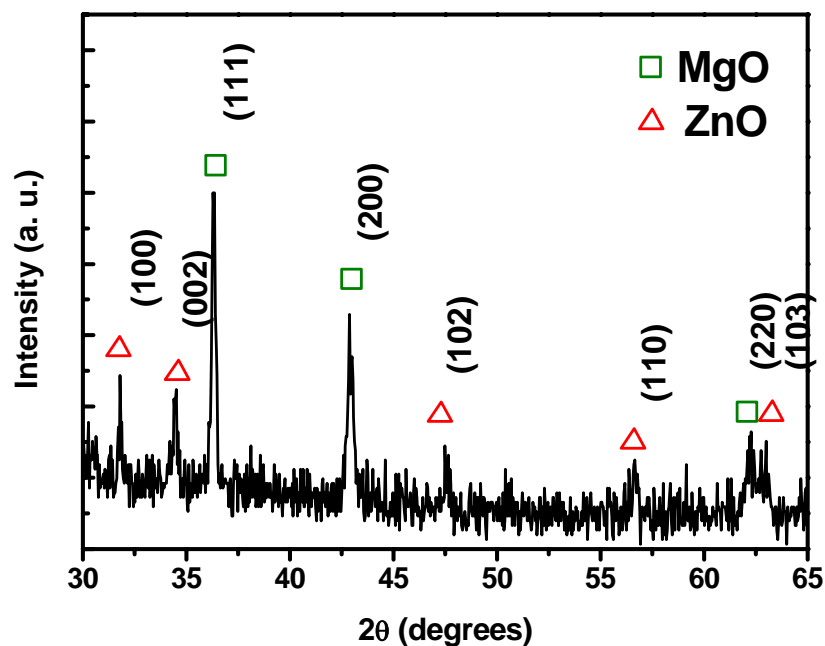
Fig.6.2 Typical XRD pattern of the as-grown nanowires.

The growth of the ZnO/MgO core-shell nanowires discussed above was accomplished by simple thermal evaporation of Zn and Mg powders. The growth is proposed to proceed as follows. Because the melting point of Zn (~419°C) is lower than that of Mg (650°C), the Zn powder would evaporate to produce Zn vapor before Mg powder does with further increasing the processing temperature. In the present case, as no evidence for catalyst particles was observed on any tips of the synthesized nanowires, therefore the vapor–solid (VS) mechanism would be a reasonable explanation for the growth of the ZnO nanowires. The follow-up vaporation of Mg would condensed, and rapidly oxidized to MgO on the ZnO nanowires. This may lead to the formation of ZnO/MgO core-shell nanowires. Although the formation mechanism is important for the fabrication of high quality ZnO-based heterostructures, the detailed growth mechanisms of the nanostructures are not fully understood.
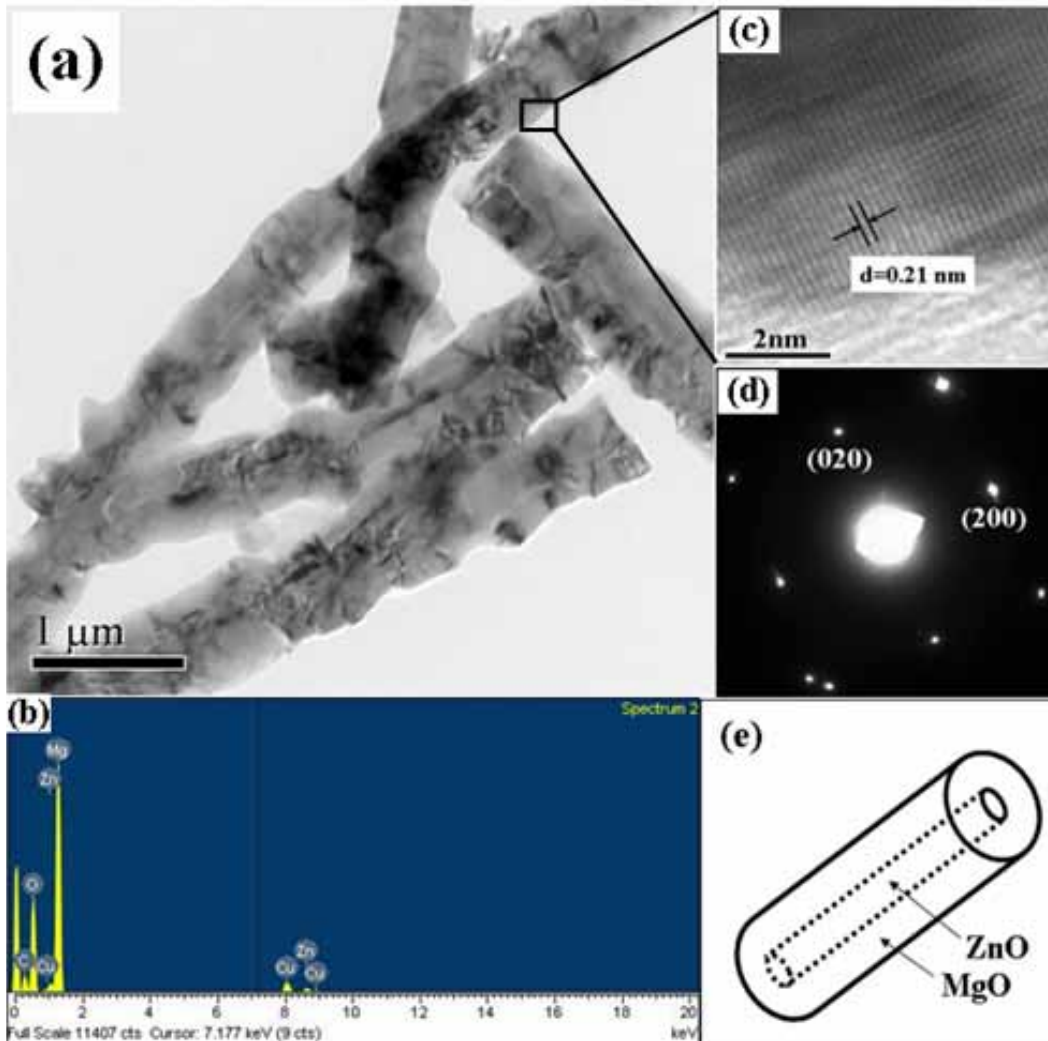
Figure 6.3 (a) TEM image of as-grown nanowires; (b) EDX analysis showing the nanowire is composed of Zn, Mg and O; (c) HRTEM image of the edge of the nanowire; (d) SAED of single-crystalline MgO with a cubic rock salt structure; and (d) Schematic model of the core-shell nanowires.

6.4 Bandgap Engineering

Figure 6-4 shows the room temperature PL spectra of the ZnO/MgO core-shell nanowires annealed at different temperatures in the range from $800^{\circ}C$ to $1000^{\circ}C$. In the PL spectra of the undoped ZnO nanowires and as-grown ZnO/MgO core-shell nanowires, an near band edge (NBE) emission peak at 3.27 eV with a Full Width at Half Maximum (FWHM) of 81 meV is attributed to the free exciton emission have been reported elsewhere.[5,6] As the annealing temperature is increased, the

position of the NBE emission peak tends towards higher photon energy with from 3.27 to 3.5 eV, as shown in Fig. 6-5. Meanwhile, the FWHM of the emission broadens gradually from 81 meV to 112 meV (Fig. 6-5). Another peak appears at 3.23 eV on the low-energy of the exciton band. While the annealing temperature increases up to 1100 ^{o}C, the position of the emission peak reaches to 3.50 eV and the low-energy peak disappears.
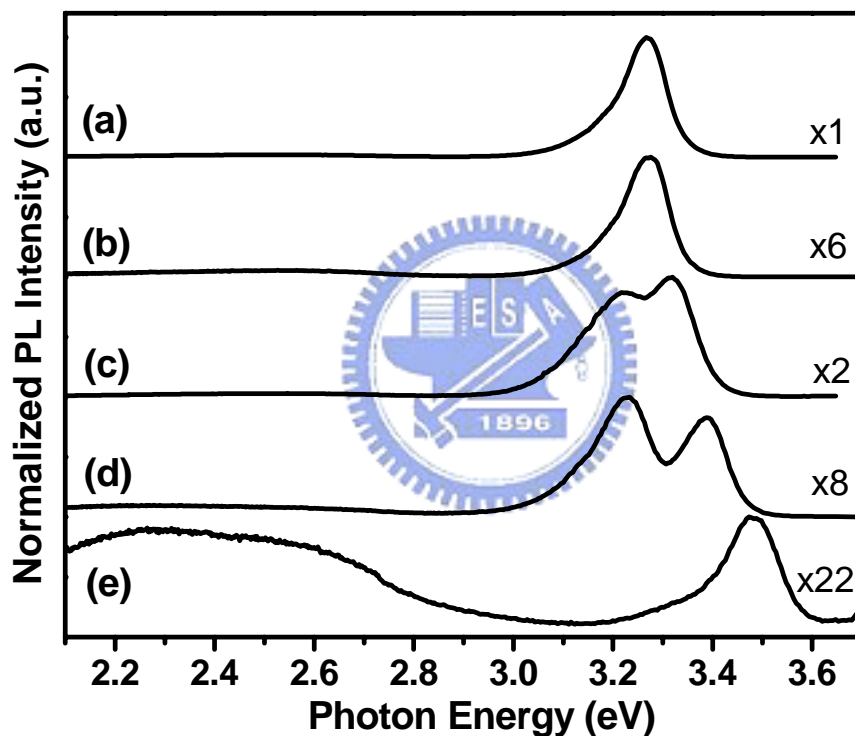
Fig. 6-4 Room temperature PL spectra of (a) pure ZnO nanowires and (b) the as grown ZnO/MgO core/shell nanowires annealed at different temperatures in the range from (c)800°C, (d)900 ^{o}C and (e)1000°C.
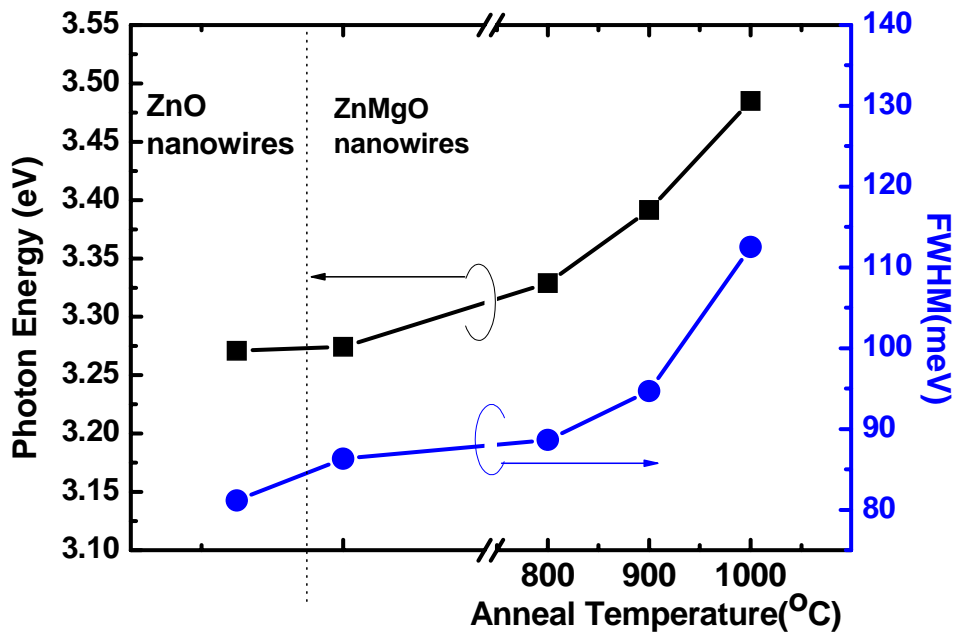
Fig. 6-5 The energy position of excitonic emission of Zno/MgO core-shell nanowires and corresponding FWHM as a function of annealing temperature.

The dramatically blueshifted emission is attributed to the formation of ternary ZnMgO nanowires via interdiffusion. Figure 6-6 shows the EDX spectra of the ZnO/MgO core/shell nanowires annealed different temperature. Zn content increases with increasing temperature. This indicates that annealing treatment leads to Mg diffusion into ZnO nanowires and Zn diffusion towards MgO. The diffused concentration content of Mg element increases while increasing annealed temperature. The origin of the emission peak at 3.22eV is should be attributed to the NBE emission from the residual inner core of ZnO nanostructures.
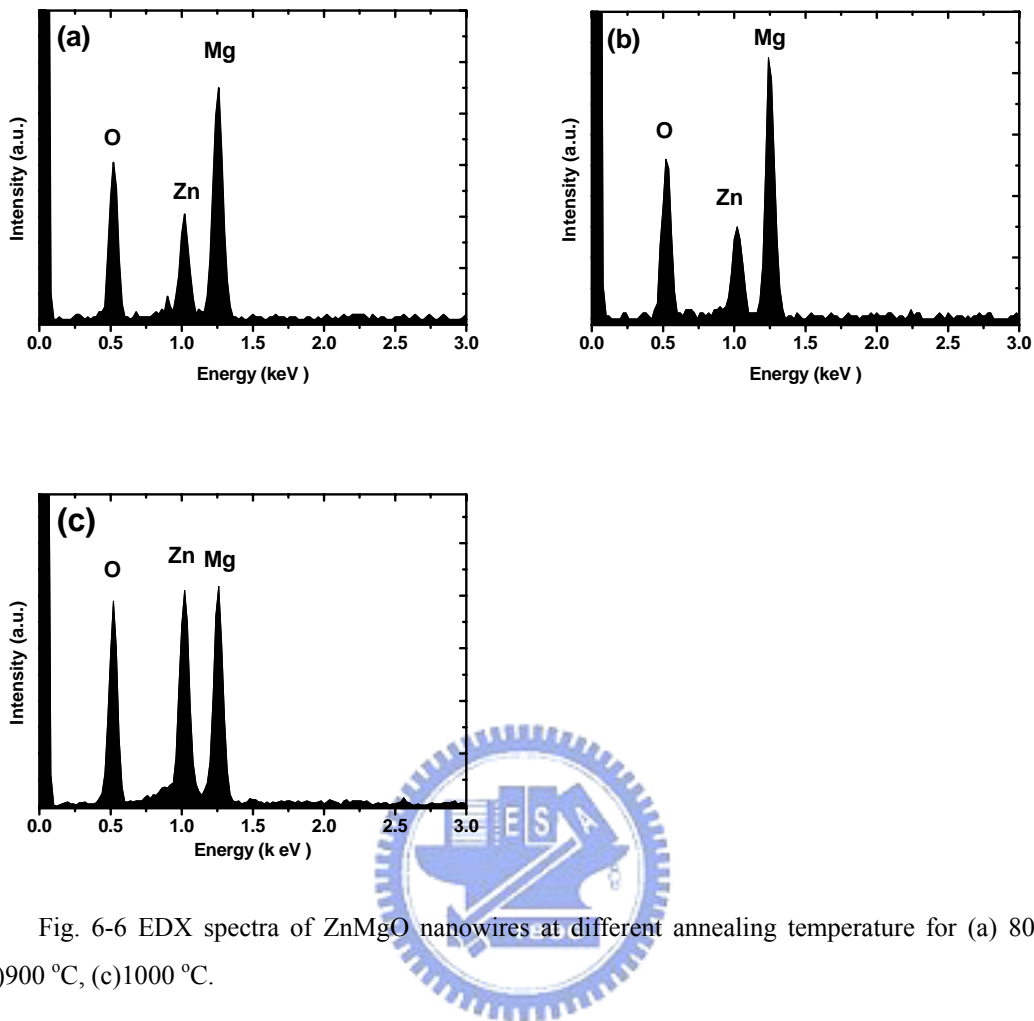
Fig. 6-6 EDX spectra of ZnMgO nanowires at different annealing temperature for (a) 800°C, (b)900 °C, (c)1000 °C.

A decrease of the PL intensity with increasing Mg concentrations results from the increase of nonradiative recombination processes. Besides the NBE emission, the other two emissions, including a blue emission at ~2.62 eV and a green emission at 2.23 eV, were also observed. The green light emission results from the single ionized oxygen vacancy in ZnO. The relative intensity of the green emission band to the NBE band also changes with the change of Mg content in the Mg-doped ZnO nanostructures. From the PL spectra, it can be seen that pure ZnO has a much stronger NBE band than the green emission band, while both Mg-doped ZnO nanonails and nanowires have a weaker NBE band than the green emission band. The relative intensity of the green emission band to the NBE band follows the order

88

Mg-doped ZnO nanowires > ZnO nanowires. The difference in the PL spectra among these products can be explained as follows. Since Mg^{+2} has a smaller ion radii than Zn^{+2}, the incorporation of Mg into ZnO crystal lattice may introduce little lattice distortion in the ZnO nanostructures. After all, Mg doping into ZnO nanostructures influences the energy structure of ZnO and thus a new band structure may be formed, which should result in changes of the PL intensity of green light emission. With the increase of Mg content in the Mg-doped ZnO nanostructures, the intensity of surface oxygen vacancies may also increase due to the insufficiency of oxygen in the reaction system, which also results in the increase of green emission. The NBE emission peak weakens and the green light emission is enhanced. The band gap broadens for the reason mentioned before, which leads to the blueshifted of the PL spectra and changes the intensity of near band edge emission. This will give rise to some new defects, such as oxygen vacancies, which should result in the changes of the PL intensity of green light emission.
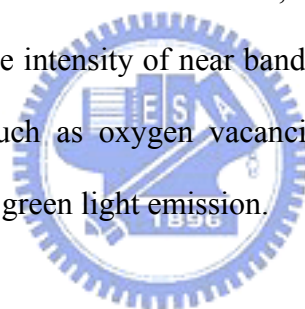
6.5 Stimulated emission

As shown in Fig 6-7 is the optical pumped spectrum as a function of excitation intensity. The emission intensity of SP and SE as a function of I_{exc} at RT is plotted in Fig. 6-7(b),(d) and (f). The SE is attributed to stimulated recombination of exciton-exciton scattering and exhibits a dependence of I_{exc} ($I_{SE} \propto I_{ext}^{\rho}$, where $\rho \sim$ 2.08). The spontaneous emission is seen to increase approximately linearly with increasing I_{exc}, while the SE is seen to increase in a strongly superlinear fashion with increasing I_{exc}. The stimulated emission is a two-particle process, which is attributed to stimulated recombination of exciton-exciton scattering.[7,8]

After annealing treatment with different temperature as well as as-grown

nanowires are shown in Figure 6.   The blue-shifting of the SE peak is also observed

and similar to the result of cw-PL.   Otherwise, when the doping of Mg is increased,

the power of I_{st} decreases from 2.08 to 1.45.   The material quality was degraded after

the process of Mg diffusion due to additional scattering centers by impurities and

defects. Hence many non-radiative centers formed or other loss mechanisms formed

after diffusion of Mg.   The cross section (or probability) of exciton-exciton

scattering is reduced.   It means that the efficiency of the stimulated emission

decreases.   The result of SE is consistent with cw-PL result.
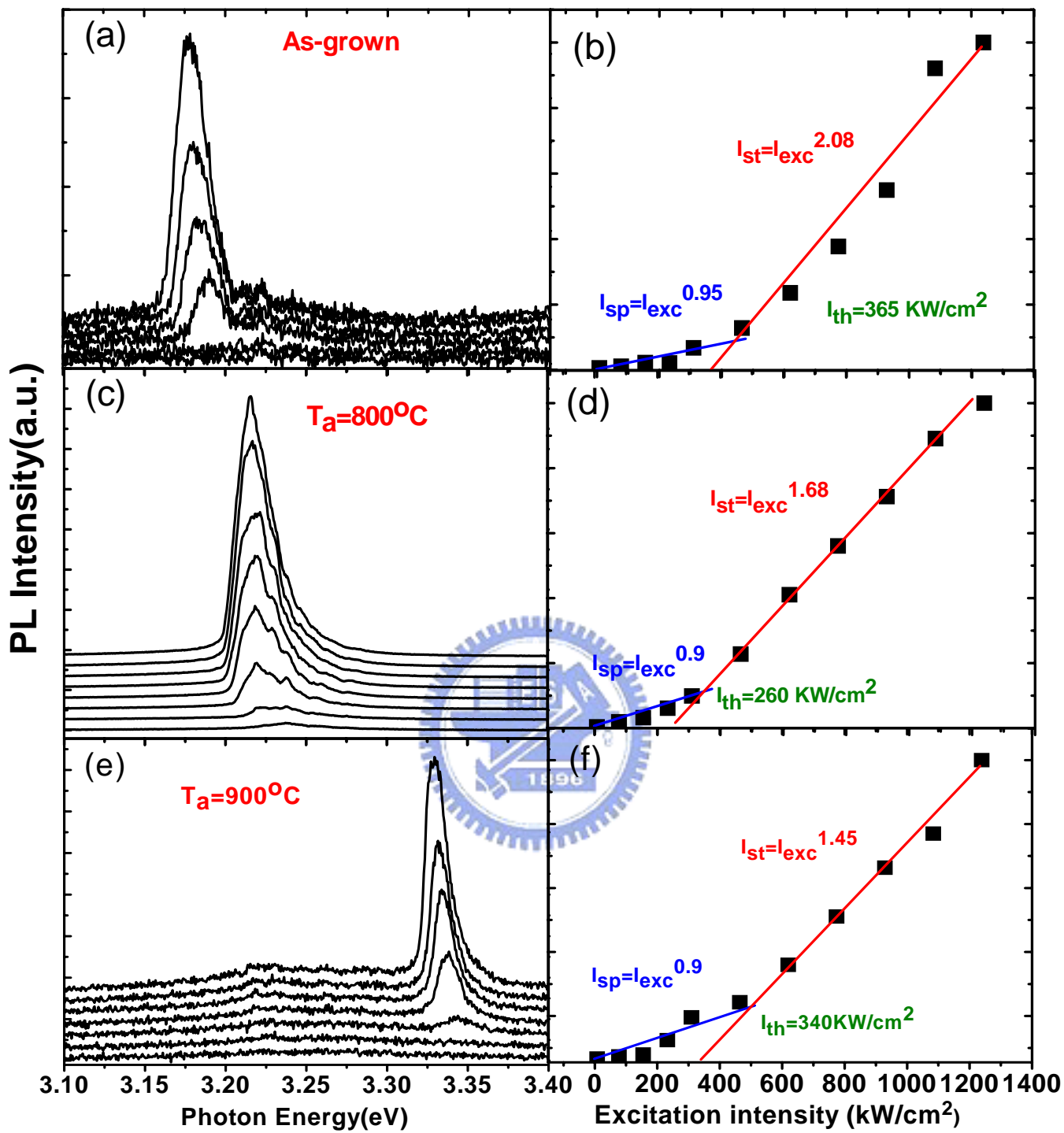
Fig. 6-7 The RT emission spectra as a function of excitation intensity for (a) as-grown (c) annealing-800°C (e) annealing-900°C ZnO/MgO core/shell nanowires. Figure 6.6 (b),(d) and (f) show the integrated PL intensity dependence on excitation intensity.

6.3 Summary

We report a simple fabricated method for the hetrostructure of ZnMgO nanowires. The formation of the core-shell structure is discussed. A blueshift in the near band emission at room temperature after annealing treatment is attributed to the diffusion of Mg into the ZnO nanowires and then ZnMgO alloy formation. Band gap engineering and stimulated emissions of ZnMgO nanowires with different Mg doping are also domesticated. The unique properties of stimulated emission in MgZnO nanowires could potentially be utilized for nano-device application.

References

[1] B. Y. Geng,G. Z. Wang, Z. Jiang, T. Xie, S. H. Sun, G. W. Meng, and L. D. Zhang, Appl. Phys. Lett. 82, 4791 (2003).

[2] G. Shen, J. H. Cho, J. K. Yoo, G. C. Yi, and C. J. Lee *Phys. Chem. B,* 109, 5491 (2005).

[3] C. H. Ku, H. H. Chiang, and J. J. Wu, *Chem. Phys. Lett.* 404, 132 (2005).

[4] C. Y. Lee, T. Y. Tseng, S.Y. Li, and P. Lin *Nanotechnology* 16, 1105 (2005).

[5] H. C. Hsu, Y. K. Tseng, H. M. Chang, J. H. Kuo, W.F. Hsieh, *J. Crystal Growth*, **261**, 520 (2004).

[6] B. P. Zhang, N. T. Binh, Y. Segawa, Y. Kashiwaba, K. Haga, *Appl. Phys. Lett,*. **84** 586 (2004).

[7] D. M. Bagnall, Y. F. Chen, Z. Zhu, T. Yao, S. Koyama, M. Y. Shen, and T. Goto, *Appl. Phys. Lett.* **70**, 2230 (1997).

[8] Y. F. Chen, N. T. Tuan, Y. Segawa, H. J. Ko, S. K. Hong, and T. Yao, *Appl. Phys. Lett.* **78**, 1469 (2001).

Chapter 7 Conclusions and Outlooks

7.1 Conclusion

We have demonstrated the possibility of selective growth of ZnO nanowires on a low temperature grown ZnO buffer layer.   The vapor-solid mechanism is responsible for this selective growth of the ZnO nanowires.   We have studied the epitaxial relationship between the nanowires and the substrates.   Besides we found enhancement of the orientation of ZnO nanowires on can be achieved by using the porous silicon substrate, we also demonstrated ZnO nanowires are vertically aligned with well in-plane alignment as a result of homoepitaxy in the region of the ZnO epifilm on c-plane sapphire.   In the region of bare c-plane sapphire, however, besides few nanowires vertically aligned with $[0001]ZnO//[0001]\alpha\text{-Al}_2\text{O}_3$, the nanowires were properly aligned with 3-fold rotation symmetry.   Furthermore, ZnO nanobelts were found at the junction regions between the epifilm and the bare sapphire (0001) surface.

Although no apparent quantum confinement was observed in these samples from the PL spectra, both of strong edge-emission and phonon-assisted exciton emission in nanowires from low temperature PL spectrum shows good crystalline quality of the grown samples.   Moreover, the LO phonon-assisted luminescence of the donor-bound excitons and free excitons in ZnO nanowires were studied at various temperatures. The strong exciton-phonon coupling in ZnO nanowires affects not only the S factor but the FXA-1LO phonon energy spacing, which can be explained by the excitonic polaron formation.   The S factor associated with FXA of the nanowires is larger than that of the epilayer.   The flattening of the energy spacing of FXA-1LO phonon replicas is attributed to formation of the excitonic polaron and the

exciton-phonon scattering dominates when the temperature exceeds the binding energy of the excitonic polaron. By fitting the temperature-dependent PL spectra with the Arrenius expression the activation energies of FXA and D^oX were obtained. The green emission is due to recombination between holes trapped at the surface defects or electrons trapped at the oxygen vacancy, the stronger green emission implies that the more surface defects existing on the side wall of the nanowires and nanobelts. We demonstrated that not only the emission prosperities but also the vibration prosperities are related between collected configuration and crystal face of nanostructures.

We have shown stimulated emission of randomly grown oriented ZnO nanowires under optical pumping. Above the lasing threshold, several sharp peaks with FWHM ~2 meV were observed which shows the superlinear dependence on the pump intensity. The random laser action requires a long enough path length of closed loop to generate photon amplification via coherent multiple scattering. If the path length of the closed loop was reduced to below a critical length, the laser action stopped. Random lasing is more easily realized in disorder-grown oriented ZnO nanowires than well-aligned ZnO nanowires because of the short mean free path of coherent light scattering in the former case. Finally, the typical cavity length of the random laser can be roughly determined by Fourier transforming the lasing spectrum.

Finally, we report on the simple fabricated method for the hetrostructure of ZnMgO nanowires. The formation of the core-shell structure is discussed. A blueshift in the near band emission at room temperature after annealing treatment is attributed to the diffusion of Mg into the ZnO nanowires and ZnMgO alloy formation. Band gap engineering and stimulated emissions of ZnMgO nanowires with different Mg doping are also demonstrated. The unique properties of stimulated emission in MgZnO nanowires could potentially be utilized for nano-device applications.

7.2 Outlooks

We have studied the substrate effect on the growth orientation of ZnO nanowires, the fundamental emission (the origin of the recombination), and the fabrication of ternary MgZnO nanowires and their optical properties. There are some pending challenges for not only fundamental research but also device applications. For fundamental research, the first challenge is to explore the properties of the single nanowire, especially carrier-carrier interactions, time-resolved photoluminescence and nonlinear optical effects. The second challenge is to fabricate fine controlled hetrostructures and stable *p*-type ZnO nanowires. The further study we must develop is to grow the periodic arrays of vertical aligned ZnO nanowires. These periodic arrays can be as 2D photonic crystals.

One of the important device applications is to achieve the electro-luminescence device, such as light emitting diode and laser. Lieber's group has developed an electrically driven CdS nanowire laser.[1] Such lasers promise to increase flexibility and to reduce costs. They also may enable new uses, including integrated single- and multicolor emitters for lab-on-a-chip systems; nanosensors for biochemical defense, medicine and general chemical and biological detection; near-field optical nanolithography; and integrated optoelectronics for inter/intra-chip optical communication.

Another application is used as energy-conservation devices based on *p-n* junctions. Energy conservation is an important issue in the future. Dye-sensitized solar cells (DSSCs) are the efficient, stable, inexpensive excitonic photovoltaic cells since they were first developed by M. Grätzel and co-worker in 1991 with an efficiency of 7.1%.[2] The most popular *n*-type semiconductor is TiO_2 nanocrystals. Very recently, two research groups individually demonstrated the ZnO nanowires

based DSSCs.[3][4]　　However, the conservation efficiency of ZnO based DSSc is 1/10 times lower than that of TiO$_2$ based DSSCs.　　To improve the conservation efficiency is an important work in the future.　　ZnO-based nanowires will be one of the most functional photonic materials in future research and device applications.

References

[1] X. Duan, Y. Huang, R. Agarwal, and C. M. Lieber, Nature **421**, 241 (2003).

[2] B. O'Regan and M. Grätzel, Nature 353, 737 (1991).

[3] J. B. Baxter, E. S. Aydil, Appl. Phys. Lett. **86**, 053114 (2005).

[4] M. Law, L. E. Greene, J. C. Johnson, R. Saykally, P. D. Yang, Nature Mater. **4**, 455 (2005).

徐旭政簡歷 (Vita)

基本資料

姓名：徐 旭 政 (Hsu-Cheng Hsu)

性別：男

出生年月日： 1976 年 04 月 15 日

籍貫: 高雄市

永久通訊處：(812) 高雄市小港區沿海一路 160 巷 3 號

email:hchsu.eo89g@nctu.edu.tw; hsucheng.hsu@gmail.com

學歷：

1994.9 – 1998.6 國立清華大學物理系 學士

1998.9 – 2000.6 國立交通大學光電所 碩士

2000.9 – 2005.6 國立交通大學光電所 博士

博士論文題目:

氣相傳輸法成長氧化鋅奈米線之光學特性研究

Optical properties of ZnO-based nanowires grown by vapor

transport method

Publication list

I. Refereed Journal Publications:

1. Kuo-Feng Lin, Hsin-Ming Cheng, **Hsu-Cheng Hsu**, Li-Jiaun Lin, and Wen-Feng Hsieh, "Band Gap Variation of Size-Controlled ZnO quantum dots synthesized by sol-gel method", *Chemical Physics Letters,* 409, 208-211 (2005).

2. Hsin-Ming Cheng, **Hsu-Cheng Hsu**, Yung-Kuan Tseng, Li-Jiaun Lin, and Wen-Feng Hsieh, "Raman scattering and efficient UV photoluminescence from well-aligned ZnO nanowires epitaxially grown on GaN buffer layer", *Journal of Physical Chemistry B 109,* 8749-8754 (2005).

3. **Hsu-Cheng Hsu**, Chun-Yi Wu, and Wen-Feng Hsieh, "Stimulated emission and lasing of random growth-oriented ZnO nanowires", *Journal of Applied Physics,* **97**, 064315 (2005). Also selected for the March 28, 2005 issue of Virtual Journal of Nanoscale Science & Technology.

4. Hsin-Ming Cheng, **Hsu-Cheng Hsu**, Shiow-Lian Chen, Wen-Ti Wu, Chih-Chun Kao, Li-Jiaun Lin, and Wen-Feng Hsieh, "Efficient Ultraviolet Photoluminescence from Monodispersed Secondary ZnO Colloidal Spheres Synthesized by Sol-Gel Method", *Journal of Crystal Growth, 277,* 192-199 (2005).

5. **Hsu-Cheng Hsu**, Ching-Sheng Cheng, Chia-Chieh Chang, Song Yang, Chen-Shiung Chang, and Wen-Feng Hsieh, "Orientation-enhanced growth and optical properties of ZnO nanowires grown on porous silicon substrates", *Nanotechnology* 16, 297-301 (2005).

6. **Hsu-Cheng Hsu** and Wen-Feng Hsieh, "Excitonic polaron and phonon assisted photoluminescence of ZnO nanowires", *Solid State Communications* 131, 371-375 (2004).

7. **Hsu-Cheng Hsu**, Yung-Kuan Tseng, Hsin-Min Cheng, Jia-How Kuo, and Wen-Feng Hsieh, "Selective growth of ZnO nanorods on pre-coated ZnO buffer layer" , *Journal of Crystal Growth* 261, 520-525 (2004).

8. Yung-Kuan Tseng, **Hsu-Cheng Hsu**, Wen-Feng Hsieh, Kuo-Shung Liu, and I-Cherng Chen, "Two-step oxygen injection process for growing ZnO nanorods" *Journal of Materials Research.* 18, 2837-2844 (2003).

9. Shi-Hao Lee, Yu-Kuei Hsu, **Hsu-Cheng Hsu**, Chen-Shiung Chang, and Wen-Feng Hsieh, " Fabrication and optical property of GaSe thin film grown by pulsed laser deposition" *Japanese Journal of Applied Physics* (1) 42, 5217-5221 (2003).

10. **Hsu-Cheng Hsu**, Hsin-Hong Chen, Shou-Yi Kuo, Chen-Shiung Chang, and Wen-Feng Hsieh, "Effect of annealing on the structural and optical properties of

AgGaS$_2$ Thin Films Prepared by Pulsed Laser Deposition", *Thin Solid Films* 419, 237–241 (2002).

II. Conference:

A. International conference

1. Wen-Feng Hsieh, Hsin-Ming Cheng, Kuo-Feng Lin, and **Hsu-Cheng Hsu**, "Size dependence of band gap variation and electron-phonon coupling in ZnO quantum dots", the Pacific Rim Conference on Lasers and Electro-Optics 2005 (CLEO-PR 2005), Tokyo, JAPAN, oral paper CTuN4-2 (2005/7).

2. **Hsu-Cheng Hsu**, Hsin-Min Cheng, Chun-Yi Wu, Yi-Chin Lee, and Wen-Feng Hsieh, "Luminescence of selective area growth of epitaxial ZnO nanowires and nanobelts", 3rd International Conference on Materials for Advanced Technologies (ICMAT 2005), Singapore, oral paper N-8-OR25 (2005/7).

3. Hsin-Min Cheng, **Hsu-Cheng Hsu**, Song Yang, Yi-Chin Lee, and Wen-Feng Hsieh, "Substrate effect on in-plane orientation of vertically well-aligned ZnO nanorods", 3rd International Conference on Materials for Advanced Technologies (ICMAT 2005), Singapore, oral paper N-9-OR26 (2005/7).

4. Chun-Yi Wu, **Hsu-Cheng Hsu**, Hsin-Min Cheng, Song Yang, and Wen-Feng Hsieh, "Structure and optical characteristics of ZnO saw-like nanostructure", 3rd International Conference on Materials for Advanced Technologies (ICMAT 2005), Singapore, post paper N-4-PO42 (2005/7).

5. Wen-Feng Hsieh, **Hsu-Cheng Hsu**, Hsin-Ming Cheng, and Kuo-Feng Lin, "Enhancement of resonant Raman scattering from ZnO Quantum Dots" in Technical Digest of Conference on Lasers and Electro-Optics (CLEO'2005), Baltimore, MD, USA, paper JWB30 (2005/5).

6. **Hsu-Cheng Hsu** and Wen-Feng Hsieh, " Exciton-phonon coupling of selective grown ZnO nanorods on pre-coated ZnO buffer layer", Materials Research Society (MRS'2003) Spring Meeting, San Francisco, CA, USA (2003/4).

7. **Hsu-Cheng Hsu**, Hsin-Hong Chen, Shou-Yi Kuo, and Wen-Feng Hsieh, "Optical and Structural Properties of AgGaS$_2$ Thin Films Prepared by Pulsed Laser Deposition", 2nd International Photonics Conference (IPC 2000), National Chiao Tung University, Hsinchu, TAIWAN, paper Th-T3-P005, Proc. IPC 2000, pp. 679-681(2000/12).

B. Domestic conference

8. Hsu-Cheng Hsu, Chun-Yi Wu, Hsin-Min Cheng, Song Yang, and Wen-Feng Hsieh, "Random lasing in 1D disorder-oriented ZnO nanosaws" in Conference of Year 2005 Annual Meeting of Chinese Physical Society, Kaohsiung, TAIWAN,

oral paper BA-5, (2005).

9. Hsin-Min Cheng, <u>Hsu-Cheng Hsu</u>, and Wen-Feng Hsieh, "Optical properties of arrays of well-aligned ZnO nanowires epitaxially grown on GaN(0001) buffer layer", in Conference of Year 2005 Annual Meeting of Chinese Physical Society, Kaohsiung, TAIWAN, post paper PK-20, (2005). (best post paper award)

10. S. Yang, **H. C. Hsu**, W. R. Liu, T. C. Huang and W. F. Hsieh, "The photoluminescence and structure analysis of ZnO nanowires on silica glass substrates", in Conference of Year 2005 Annual Meeting of Chinese Physical Society, Kaohsiung, TAIWAN, oral paper DB-3, (2005).

11. Kuo-Feng Lin, **Hsu-Cheng Hsu**, Hsin-Ming Cheng, and Wen-Feng Hsieh "Influence of crystal size on the photoluminescence of ZnO quantum dots grown by sol-gel technique" in Proceedings of Optics and Photonics Taiwan'04, Chunli, TAIWAN, oral paper (2004).

12. Chun-Yi Wu, **Hsu-Cheng Hsu**, Hsin-Min Cheng, Song Yang, and Wen-Feng Hsieh, "Self-formed laser cavity in ZnO nanosaws" in Proceedings of Optics and Photonics Taiwan'04, Chunli, TAIWAN, oral paper (2004).

13. Ming-Rung Tsai, Kuo-Feng Lin, **Hsu-Cheng Hsu**, and Wen-Feng Hsieh, "以溶膠凝膠法製備 MgxZn1-xO 粉末之發光特性研究" in Proceedings of Optics and Photonics Taiwan'04, Chunli, TAIWAN, post paper (2004).

14. **Hsu-Cheng Hsu**, Song Yang, Ching-Sheng Cheng and Weng-Feng Hsieh, "Fabrication of ZnO nanowires and their UV emission properties" in Conference of Year 2004 Annual Meeting of Chinese Physical Society, Hsin-Chu, TAIWAN, oral paper PP-73, (2004).

15. Song Yang, **Hsu-Cheng Hsu**, and Weng-Feng Hsieh, "Growth of vertical-oriented ZnO nanowires on quartz glass by a NiO-assisted vapor depositon" in Conference of Year 2004 Annual Meeting of Chinese Physical Society, Hsin-Chu, TAIWAN, post paper PP-37, (2004).

16. Ching-Sheng Cheng, Song Yang, **Hsu-Cheng Hsu**, Jia-Jay Chang, Chen-Shiung Chang, and Wen-Feng Hsieh, "Orientation enhancement of ZnO nanowires using a porous silicon substrate and their excitonic photoluminescence", in Proceedings of Optics and Photonics Taiwan'03, Taipei, TAIWAN, post paper FB4-6 (2003).

17. <u>Hsu-Cheng Hsu</u>, Wen-Feng Hsieh, "Room-temperature stimulated emission from single crystalline ZnO nanowires" in Proceedings of Optics and Photonics Taiwan'03, Taipei, TAIWAN, oral paper FA3-1 (2003).

18. Ching-Sheng Cheng, <u>Hsu-Cheng Hsu</u>, Jia-Jay Chang, Chen-Shiung Chang, Wen-Feng Hsieh,"Enhanced near band edge emission from ZnO nanorod grown on porous silicon by vapor transport process" in Conference of Year 2003 Annual

Meeting of Chinese Physical Society, Hwa-Lean, TAIWAN, post paper PE-18, (2003).

19. <u>Hsu-Cheng Hsu</u>, Wei-Rien Liu, and Wen-Feng Hsieh, "Growth of ZnO Nanowires and Their Exciton-Phonon Interaction", in Proceedings of Optics and Photonics Taiwan'02, Taipei, TAIWAN, oral paper FA4-4 (2002).

20. 李明達, 盧啟原, <u>徐旭政</u>, 張振雄, 謝文峰, " 利用脈衝雷射沉積層狀半導體 硒化鎵薄膜於化學處理矽基板之製程與特性研究", in Proceedings of Optics and Photonics Taiwan'02, Taipei, TAIWAN, post paper PA-15 (2002).

21. Jia-Hao Kuo, Hung-Yu Lin, <u>Hsu-Cheng Hsu</u>, and Wen-Feng Hsieh, " The Stusy of Preparation and Optical Properties on ZnO Thin Films by Pulsed Laser Deposition" in Proceedings of Optics and Photonics Taiwan'02, Taipei, TAIWAN, post paper PA-16 (2002).

22. Jia-How Kuo, <u>Hsu-Cheng Hsu</u>, Wen-Feng Hsieh, "Characterization of ZnO Thin Films by Pulsed Laser Deposition", in Conference of Year 2002 Annual Meeting of Chinese Physical Society, Taichung, TAIWAN, post paper D-075, 2002.

23. Min-Dar Lee, <u>Hsu-Cheng Hsu</u>, Yu-Kuei Hsu, Chen-Shiung Chang and Wen-Feng Hsieh, "Van der Waals epitaxy of GaSe thin film on hydrogen-terminated Si(111) surfaces by pulsed laser deposition", in Conference of Year 2002 Annual Meeting of Chinese Physical Society, Taichung, TAIWAN, post paper E-048 (2002).

24. <u>Hsu-Cheng Hsu</u>, Shi-How Lee, Min-Dar Lee, Yu-Kuei Hsu, Chen-Shiung Chang and Wen-Feng Hsieh, "Van der Waals epitaxial growth of GaSe layered films on variable substrate by Pulsed Laser Deposition" in Conference of Year 2002 Annual Meeting of Chinese Physical Society, Taichung, TAIWAN, oral paper E-064 (2002).